

# Technical University of Berlin

Institute of Fluid Dynamics and Technical Acoustics  
Laboratory for Flow Instabilities and Dynamics  
Prof. Dr.-Ing. K. Oberleithner

---

Master Thesis

## Application of linear stability analysis on a flow field of a swirl-stabilized burner

Lukas Moczarski

Berlin, den 01.09.2020

Email: lukas.moczarski@gmail.com  
Matriculation Number: 410 913  
Study Program: Engineering Science M.Sc.  
Supervisors: Prof. Dr.-Ing. Kilian Oberleithner (Technical University of Berlin)  
Dr. -Ing. Thomas Ludwig Kaiser (Technical University of Berlin)  
Dr. -Ing. André Fischer (Rolls-Royce Deutschland)



---

## Erklärung der Selbstständigkeit / Declaration of Authorship

---

Hiermit erkläre ich, dass ich die vorliegende Arbeit selbstständig und eigenhändig sowie ohne unerlaubte fremde Hilfe und ausschließlich unter Verwendung der aufgeführten Quellen und Hilfsmittel angefertigt habe.

This thesis is composed of my original work, and contains no material previously published or written by another person except where due reference has been made in the text. I have clearly stated the contribution by others to jointly-authored works that I have included in my thesis.



Lukas Moczarski

Berlin, 16.06.2020



---

## Zusammenfassung

---

Diese Arbeit beschäftigt sich mit der Anwendung der Linearen Stabilitätsanalyse(LSA) auf numerisch ermittelte, hochturbulente Strömungsfelder einer industriellen Drallbrenner-geometrie mit Kerosin-Einspritzung. Die Grundlage der Analyse bilden Datensätze des kompressiblen Finite-Volumen-Strömungslöser PRECISE-UNS (Predictive system for Real Engine Combustors with Improved Sub-models and Efficiency - UNStructured) welcher innerhalb des Unternehmens Rolls-Royce Deutschland entwickelt wurde, mit dem Ziel, die hochkomplexe Strömungs- und Verbrennungsdynamik der Brennkammer zu modellieren. Diese Datensätze werden mit Hilfe einer in dieser Arbeit erarbeiteten Methode dem LSA-Tools FELiCS zugeführt, welches aktuell an der TU Berlin am Fachgebiet für Dynamik Instabiler Strömungen entwickelt wird. Diese Arbeit dient als Evaluation der Möglichkeiten der linearen Stabilitätsanalyse als Validierungs- und Vorhersagetool im industriellen Kontext. Im ersten Teil werden auf Basis der Modalanalyse rein hydrodynamische Strukturen und Mechanismen untersucht. Daran anschließend wird mit der Resolventenanalyse die Antwort der Strömung auf Anregung ermittelt und darauf basierend Aussagen zur thermoaktustischen Rezeptivität getroffen.

Aus PRECISE gewonnene Large-Eddy-Simulation(LES)-Schnappschüsse werden zunächst mit Hilfe empirischer Methoden zur modalen Zerlegung, namentlich die Proper-Orthogonal Decomposition(POD) und die Dynamical-Mode-Decomposition(DMD), auf kohärente Strukturen untersucht. Sowohl in reagierenden als auch nicht-reagierenden Simulationen werden dabei Moden gefunden, die auf helikale Instabilitäten hinweisen, die sich vom Inlet ausgehend im Strömungsfeld ausbreiten.

Die zeitlich gemittelten LES-Daten werden mittels einer globalen linearen Stabilitätsanalyse untersucht. Diese basiert auf den linearisierten Erhaltungsgleichungen für Masse und Impuls. Im Falle der reagierenden Strömung mit anwesender Flamme wird dem inhomogenen Temperatur- und damit Dichtefeld mit einer dritten Gleichung Rechnung getragen, welche aus der Energiegleichung hergeleitet wird. Einsetzen eines harmonischen Modalansatzes führt zu einem Eigenwertproblem, dessen Eigenwertspektrum Aufschluss über intrinsische Instabilitäten im Strömungsfeld gibt. Um die beim Linearisieren der Gleichungen auftretenden zusätzlichen Terme zu schließen, werden verschiedene Viskositätsmodelle evaluiert.

Die Modalanalyse findet separierte Eigenwerte und -vektoren, welche in räumlicher Gestalt

und zeitlicher Frequenz in guter Übereinstimmung mit den dominanten Moden der POD und DMD stehen. Um die zugrundeliegenden Mechanismen besser verstehen zu können, werden die 2D-Moden wieder auf die 3D-Geometrie extrapoliert. Phänomenologisch lassen diese sich als Doppelhelix beschreiben, welche sich entgegen der tangentialen Hauptströmungsrichtung vom Inlet aus im Strömungsfeld ausbreitet.

Um die Möglichkeiten der linearen Stabilitätsanalyse als Vorhersagetool bewerten zu können, werden Modalanalysen auf RANS-Strömungsfeldern angewendet, welche in Geometrie und Randbedingungen den LES-Simulationen gleichen, jedoch auf allen Größenskalen auf den zeitlich gemittelten Gleichungen basieren und den Einfluss von Turbulenz gänzlich modellieren. Hier weichen die Frequenzen und räumlichen Strukturen von den LES-Ergebnissen ab, die grundsätzliche Dynamik einer dominanten helikalen Instabilität wird jedoch identifiziert. Die Ergebnisse für reagierende und nicht-reagierende Strömung werden vorgestellt und mit denen der LES verglichen.

Im zweiten Teil der Arbeit wird untersucht, ob die Antwort der Strömung auf akustische Anregung mittels der Resolventenanalyse korrekt wiedergegeben werden kann. Dazu werden DMD-Moden harmonisch angeregter LES-Simulationen mit den Ergebnissen der Resolventenanalyse verglichen.

---

## Contents

---

1	Introduction	1
2	Theoretical foundations	5
2.1	Computational fluid dynamics . . . . .	6
2.1.1	Reynolds-averaged Navier-Stokes . . . . .	6
2.1.2	Large-eddy simulation . . . . .	8
2.1.3	Combustion modeling . . . . .	8
2.2	Linear stability analysis . . . . .	9
2.2.1	Modal analysis . . . . .	14
2.2.2	Resolvent analysis . . . . .	16
2.3	Data-based analysis . . . . .	17
2.3.1	Fast Fourier transform . . . . .	17
2.3.2	Proper orthogonal decomposition . . . . .	18
2.3.3	Spectral proper orthogonal decomposition . . . . .	19
3	Flow configuration and data-based analysis	21
3.1	The flow fields . . . . .	21
3.2	POD and DFT results . . . . .	23
4	Application of Linear Stability Analysis	29
4.1	FELiCS tool . . . . .	29
4.2	Turbulent viscosity evaluation . . . . .	31
4.2.1	$\nu_t$ - constant . . . . .	32
4.2.2	$\nu_t$ - TKE based . . . . .	33
4.3	Results . . . . .	36
4.3.1	LES cold flow . . . . .	36
4.3.2	LES reacting flow . . . . .	41
4.3.3	RANS cold flow . . . . .	46
4.3.4	RANS reacting flow . . . . .	48

5 SPOD and Resolvent Analysis	53
5.1 Flow field . . . . .	54
5.1.1 Results: SPOD and LSA . . . . .	56
5.1.2 Results: SPOD and RA . . . . .	60
Bibliography	65

---

## List of Figures

---

2.1	Three dimensional array with $N_b$ snapshot matrices stacked in the third dimension. . . . .	19
3.1	x-r-slices through cylindrical flow domain for cold LES (a), reacting LES (b), cold RANS (c) and reacting RANS (d). Flow direction is left to right, with the pilot jet and the outer inlet passages on the leftmost side of each figure. Streamlines represent velocity in x-r-plane. In the reacting simulation, the black lines represent isocontour of the region of highest mean heat release corresponding to the flame position. . . . .	22
3.2	First 50 eigenvalues as obtained in the POD for the cold and reacting LES. The eigenvalues are sorted by relative energy in descending order. Relative energy is expressed as a fraction of cumulated energy of all eigenvalues. . .	23
3.3	First four POD modes of the x-r-plane for cold and reacting simulation (upper and lower half plane respectively). Depicted is the axial velocity component. The contour colours are normalized by the maximal value of axial velocity of the respective mode. The percentage of fluctuating energy contained in each mode is written in the bottom right corner. . . . .	24
3.4	Isocontour of instantaneous vorticity (red) calculated by means of the Q-criterion on the cold 3D-field, overlayed with the POD planar axial velocity field (a) and streamlines of the mean velocity field (b). . . . .	25
3.5	PSD of axial velocity of instantaneous x-r-plane snapshots. The velocity of all spacial points is taken into account. The PSD is plotted over the non-dimensional Strouhal number. This dimensionless Number is defined as $St = \frac{f \cdot D}{U_{ref}}$ , relating the oscillation frequency to a reference length and velocity. The reference values are chosen as the outermost inlet diameter and an arbitrary velocity in the range of the inlet stream velocities. . . .	26
3.6	Axial velocity of DFT modes associated to the four main peaks in the PSD depicted in Figure 3.5. Only the real part is shown and the colours are normalized with the maximum value of the respective mode. . . . .	27
4.1	Numerical domain and boundary conditions for the BiGlobal LSA. . . . .	31

4.2	LSA eigenvalue spectra of the LES cold mean field for different values of $\nu_t$ . The only physical eigenmode is found for $\nu_t = 10^3 \cdot \nu_{\text{mol}}$ and is encircled in red. . . . .	32
4.3	<b>(a)</b> : Mean field with black lines indicating the x-velocity at the respective axial position marked by the vertical dashed black lines. Red lines mark the distance between the local x-velocity extrema at the particular axial position. <b>(b)</b> : Radial distance $l$ between local extrema as a measure for the turbulent length scale. . . . .	33
4.4	Left side: Spacial distribution of turbulent kinetic energy $k$ , turbulent length scale $l_m$ and sponge viscosity $\nu_{\text{sp}}$ . Right Side: The complete viscosity field as an addition of $\nu_{\text{sp}}$ and the turbulent viscosity calculated by $\nu_t = cl_m\sqrt{k}$	34
4.5	Left side: LSA eigenvalue spectra for an azimuthal wavenumber of $m = -2$ obtained with a constant viscosity and with a viscosity calculated with the TKE-model. Right Side: Coherent velocity field corresponding to the respective separated eigenvalues in comparison with the spacial shape of the dominant POD mode. Contour colours are normalized with the maximal value of each field. . . . .	35
4.6	Cold flow LSA Eigenvalue spectra of different azimuthal wavenumbers $m = \{-1, -2, -3, -4, -5\}$ plotted together. The red lines mark the oscillation frequency of the five modes identified by means of DFT. The separated eigenvalue corresponding to the global mode of each wave number is enlarged and depicted in the legend. The lower half shows the mode shape corresponding to each separated eigenvalue at the respective azimuthal wave number in comparison with the DFT modes at the frequencies marked by the red line. . . . .	37
4.7	Axial, radial and azimuthal velocity component of the adjoint mode corresponding to the direct mode for $m = -2$ . . . . .	38
4.8	<b>a</b> : Structural sensitivity of each global modes from Figure 4.6. <b>b</b> : Mean velocity field with streamlines in x-r-plane and a clearly shaped recirculation bubble. The dark red mark indicates the location of highest structural sensitivity and therefore the wavemaker of the global modes. . . . .	39
4.9	Azimuthal vorticity of dominant mode (blue isocontour) overlayed with the instantanious vorticity from the 3D-field calculated with the Q-criterion. .	40
4.10	LSA eigenvalue spectra and spacial shapes of separated eigenvalues at different azimuthal wavenumbers $m = \{-1, -2, -3, -4, -5\}$ as obtained for the reacting LES using the equations for a non-homogenous density. The layout is similar to Figure 4.6. . . . .	41
4.11	<b>a</b> : Structural sensitivity of the five global modes of the reacting LES as obtained with low mach LSA. <b>b</b> : Axial component of the mean velocity field with streamlines in x-r-plane and a clearly visible recirculation bubble. The red mark indicates the wavemaker position and the black lines are isocontours of the mean heat release indicating the flame position. . . . .	43

4.12 LSA eigenvalue spectra and spacial shapes of separated eigenvalues at different azimuthal wavenumbers $m = \{-1, -2, -3, -4, -5\}$ as obtained for the reacting LES calculated with the equations for a uniform density. The layout is similar to Figure 4.6. . . . .	44
4.13 <b>a:</b> Structural sensitivity of the five global modes of the reacting LES as obtained with cold flow LSA. <b>b:</b> Axial component of the mean velocity field with streamlines in x-r-plane and a clearly visible recirculation bubble. The red mark indicates the wavemaker position and the black lines are isocontours of the mean heat release indicating the flame position. . . . .	45
4.14 Eigenvalue spectra and spacial shapes of separated eigenvalue at different azimuthal wavenumbers $m = \{-1, -2, -3, -4, -5\}$ as obtained for the cold flow RANS. The layout is similar to Figure 4.6. The five separated eigenvalues from the cold flow LES are depicted in red. . . . .	46
4.15 <b>a:</b> Structural sensitivity of the five global modes of the cold flow RANS. <b>b:</b> Axial component of mean velocity field with streamlines in x-r-plane and a clearly shaped recirculation bubble. The red mark indicates the wavemaker position. . . . .	47
4.16 Low mach eigenvalue spectra and spacial shapes of separated eigenvalue at different azimuthal wavenumbers $m = \{-1, -2, -3, -4\}$ as obtained for the reacting RANS calculated with the equations for non-uniform density. The layout is similar to Figure 4.6. The four separated eigenvalues from the low mach LSA on the reacting LES are depicted in red. . . . .	49
4.17 'Cold hot' eigenvalue spectra and spacial shapes of separated eigenvalue at different azimuthal wavenumbers $m = \{-1, -2, -3, -4\}$ as obtained for the reacting RANS calculated with the assumption of a uniform density. The layout is similar to Figure 4.6. The five separated eigenvalues from the 'cold hot' LSA on the reacting LES are depicted in red. . . . .	49
4.18 <b>a:</b> Structural sensitivity of the five global modes of the reacting RANS as obtained with the low mach and the 'cold hot' LSA. <b>b:</b> Axial component of mean velocity field with streamlines in x-r-plane and a clearly shaped recirculation bubble. The red mark indicates the wavemaker position. . . . .	50
5.1 x-r-slice through cylindrical flow domain for cold LES. Flow direction is left to right, with the pilot jet and the outer inlet passages on the leftmost side of the figure. . . . .	54
5.2 Isocontour of instantanious vorticity calculated by means of the Q-criterion on the cold 3D-field. The view is in axial direction from a downstream position. The isocontour is colored by wall distance to distinguish between the inner $ m  = 1$ and the outer $ m  = 3$ vortex. The cyan and red circles indicate the position of the inner and middle passage respectively. . . . .	55

---

5.3	SPOD and LSA spectra (first and second column) for the cold flow LES for azimuthal wave numbers of $-4 \geq m \leq 4$ . For $ m  = \{1,2,3\}$ , the results for negative and positive azimuthal wave numbers are plotted in the same row. The dominant peak in every SPOD spectrum is circled either in red or blue. The frequency of those peaks is shown as equally colored lines in the LSA spectrum to allow a direct comparison. If a corresponding LSA mode is found, it is circled in the same color as the SPOD peak. Both modes are compared in the third column, red on the left and blue on the right. If no corresponding LSA mode is found, the SPOD mode is plotted alone. . . . .	57
5.4	Structural sensitivity of the dominant LSA modes. The region of highest sensitivity is marked in the mean field in the lower half. The region of highest sensitivity are marked as a red marker for $m = \{-2, -3, -4\}$ and as a black marker for $m = 1$ . . . . .	59
5.5	SPOD spectra and RA gains for the cold flow LES for azimuthal wave numbers of $-4 \geq m \leq 4$ . The SPOD and RA spectra for each azimuthal wave number are plotted in the same figure to directly compare the envelopes. The dominant SPOD peak is circled in either red or blue and the corresponding RA gain at that frequency is marked with a cross in the same color. If a global mode was found within the LSA, a vertical line indicates the frequency of that mode in the same color as the corresponding SPOD peak. The associated SPOD and RA modes are pictured in direct comparison in the third column of the figure, with red marked modes/responses on the left and blue marked modes/responses on the right. . . . .	61
5.6	Eigenvalue spectrum of LSA conducted with the TKE-viscosity model. The upper half shows the results for a deactivated sponge layer, the lower half for an activated sponge layer. The separated eigenvalue is not affected by the sponge viscosity. . . . .	63

---

## List of Tables

---



---

## List of Abbreviations

---

**CFD** Computational Fluid Dynamics

**DNS** Direct Numerical Simulation

**FELiCS** Finite Element Linear Combustion Solver

**LES** Large-Eddy Simulation

**LSA** Linear Stability Analysis

**NSE** Navier-Stokes Equation(s)

**PRECISE-UNS** Predictive system for Real Engine Combustors with Improved Sub-models and Efficiency - UNStructured

**RANS** Reynolds-Averaged-Navier-Stokes



---

## List of Symbols

---

### Latin

$G$  spatial filter function  
 $k$  turbulent kinetic energy

$R_s$  specific gas constant

$t$  time  
 $T$  temperature  $u$  velocity

### Greek

$\mu$  dynamic viscosity  
 $\mu$  RA-gain  
 $\nu$  kinematic viscosity  
 $\rho$  density  
 $\tau$  viscous stress tensor

### Dimensionless Quantities

$Re$  Reynolds number

### Subscripts

$t$  turbulent



# CHAPTER 1

---

## Introduction

---

One of the most crucial parts in the development process of aero-engines certainly is the design of the combustion chamber. With weight and size being the limiting factor in aviation, they are required to operate in extremely high power density regimes in order to be able to propulse an aircraft. This high power density in aero-engines is achieved by using liquid fuels, high pressures and a highly turbulent flow which accelerates the combustion process. To further induce turbulence and enhance the chemical reaction, modern combustor inlets induce a swirled motion to the flow field. This leads to the radial opening of the inlet streams, giving rise to a recirculation zone which stabilizes the flame and further enhances species mixing and combustion performance. To additionally achieve an efficient and clean combustion process, modern aero-engine combustors are designed to operate in a lean environment, reducing  $NO_x$  emissions. Unfortunately, these very aspects yield a technical system highly susceptible for unsteady mechanism commonly referred to as combustion or thermoacoustic instabilities.

Most combustion systems such as aero engines but also rockets and gas-turbines are designed to operate in a steady environment. This steadiness is of statistical nature, meaning that the flow field is stationary with turbulent fluctuations arising over a large range of frequencies. With those broad band velocity and pressure fluctuations, the heat release of the flame fluctuates in a broadband manner as well, emitting a noise spectrum of incoherent and diffuse nature, posing no immediate threat to a safe engine operation. However, these stochastic heat release fluctuations might lock into acoustic modes of the combustion chamber, inducing a positive feedback mechanism of combustion and acoustic waves. Based on this, small perturbations can grow exponentially up to high amplitude self-sustained oscillations, which result in unacceptable noise emissions, efficiency loss or even structural failure of components. While the fundamental physical mechanism behind this has been known for over a century [1], combustion instabilities have always been and remain one of the most challenging problems in fluid mechanics. They incorporate turbulence, acoustic waves and multi-phase reacting flows within complex boundaries, yielding a vast number of interacting mechanisms [2]. Hence, oftentimes they

are only discovered in a late stage of development, requiring an extensive redesign. A famous example for this is the design process of the F1 rocket engine of the Saturn V. A thermoacoustic instability in the combustion chamber necessitated a staggering 1332 full scale test to finally get the destructive oscillation under control [3]. The early prediction of thermoacoustic instabilities therefore is of great importance in the design process, making it a subject of intensive research within the combustion community.

One phenomenon known to have an influence on the onset of combustion instabilities is the formation of large-scale coherent structures within the flow field. These structures often arise in shear layers and can be observed as vortical structures in various flow configurations. They are most easily recognizable at low Reynolds numbers such as the famous *von Kármán vortex street* arising in the wake of a cylindrical obstacle in the flow field [4]. But also in the context of highly turbulent flows which appear entirely incoherent and stochastic, various mechanisms have been observed to bring structure into the chaos. These structures contain the majority of turbulent kinetic energy, which from there on gets transferred to smaller and smaller eddies, ultimately dissipating to heat on a molecular level. In contrast to the small scale turbulent motion, coherent structures have a deterministic behaviour which can be described as wave-like motion, as theoretically described by Reynolds and Hussain [5] and successfully visualised for a turbulent mixing layer by Brown and Roshko [6] and for a turbulent mixing jet by Crow and Champagne [7].

In swirled combustor flow fields of gas turbines or aero-engines, large-scale coherent structures are mainly induced by a phenomenon called vortex breakdown. This mechanism is triggered by a sufficiently large swirl of the fluid and is characterized by the appearance of flow reversal in certain regions. The emerging region of high shear between the recirculation zone and the surrounding jet is known to induce helical coherent structures, which travel downstream and dominate the entire flow field dynamic [8] [9] [10]. These hydrodynamic structures can interact with the acoustic field in a combustor [11] [12] [13] and when locked into an acoustic mode give rise to thermoacoustic instabilities.

Generally, to predict the behaviour of a flow field, the common approach in industry and academics is to discretize the Navier-Stokes Equations (NSE) and solve them numerically. However, the orders of magnitude of length scales in highly turbulent flows are of such large difference, reaching from the Kolmogorov scale ?? to the geometric boundaries of the domain, that a Direct Numerical Simulation (DNS) of the entire instantanious flow field remains impractical in the near future ?. A common trade off in industry is the numerical solving of the so called Reynolds-Averaged Navier-Stokes Equations (RANS). RANS calculations are the least computationally expensive CFD method and as such still are the most common in CFD-Codes for the majority of industrial applications. They decompose the flow in a mean and a fluctuating quantity and solve for the mean properties. In consequence, they do not resolve unsteady behaviour of the flow. In the case of complex configurations with inhomogenous turbulence and large coherent structures, this method is generally not able to resolve the flow accurately. However, even though a flow field in a swirled aero-engine combustor is remarkably complex, a RANS simulation still

captures general trends regarding emission and aerodynamic performance and is therefore extensively used during preliminary design processes [14].

Since RANS is not able to capture any unsteady features of a flow, in recent years the method of a Large-Eddy Simulation (LES) has become a common used tool in industry. In terms of computational requirements and accuracy, Large Eddy Simulation (LES) is located between RANS and DNS, resolving large scale unsteady motions while locally modeling the influence of the small sub-grid-scale fluctuations. LES therefore gives insight into unsteady behaviour of a flow and is widely used in industrial research and development to investigate the onset of thermoacoustic and hydrodynamic instabilities. The high numerical cost of an unsteady reacting LES however prevents it to be used routinely within an industrial design process.

All of those simulations have one thing in common..experiment, no insight into the cause of mechanism

To investigate coherent structures arising from hydrodynamic instabilities and to gain new insights into their feedback mechanisms, a linear stability analysis might be the more efficient tool. To apply it, the Navier-Stokes Equations are linearized around the mean flow and a harmonic modal ansatz is inserted. The linearized equations then pose an eigenvalue problem whose solutions give information about the frequency, shape and growth of hydrodynamic instabilities. Since the LSA is based on the linearized equations, the computational costs are just a fraction compared to the previously introduced method of integrating the full set of nonlinear equations in time. With a potential interaction between acoustic modes and hydrodynamic instabilities, as observed by Terhaar et al. [11], the prior knowledge of the latter just from a mean field is of great interest in industrial applications. The great potential within the LSA is its ability to detect instabilities and the regions of high receptibility in which they are induced, with only base or mean flow data as input. The significant value this technique could potentially have in an industrial context is obvious. While currently it is necessary to solve a computational expensive Large Eddy Simulation to obtain accurate knowledge of unsteadiness within a complex flow configuration, the low order approach of LSA can identify instabilities intrinsic of the mean field with just a fraction of the computational effort. In addition to that, the LSA opens the door for unsteady analysis of flow fields obtained by means of Reynolds-Averaged Navier Stokes simulation, which is still the standard CFD approach in industry, and could therefore be a valuable tool in industrial design processes.

In addition to that, application of a Resolvent Analysis (RA) can approximate the hydrodynamic response to acoustic forcing and potentially estimate the Flame Transfer Function of a combustor with the mean field and flame as input [15].

The main motivation of this thesis is to perform a linear stability analysis on an industrial swirled flow field to evaluate the capabilities of the method and to introduce it as a potentially valuable tool with respect to injector and combustion chamber design processes. Linear stability analysis has been conducted on a variety of different flow configurations from free shear layer [16], to bluff body wake flows [17] to swirling flows in gas turbine

fuel injectors [18]. Depending on the complexity of the flow, the LSA can yield a great success in predicting the frequency and growth rate of intrinsic hydrodynamic instabilities. However, so far it is mostly used as a diagnostic tool to further investigate already known instabilities which has been extracted by means of data-based modal analysis such as Proper Orthogonal Decomposition. Of great interest to the industrial community is a potential use of LSA as a predictive tool.

Modern aero-engine combustion chambers are fully annular in design, with a separation into individual sectors. Each of these sectors contain an upstream liquid fuel injector. To achieve a clean and highly efficient combustion, modern aero-engine combustors are designed to operate in a lean environment with a highly turbulent flame to allow for high energy densities.

This thesis focuses on a swirl stabilized flow field in a cylindrical domain with a characteristical three passage inlet. Each of the flow passages includes a set of vanes which induce a swirled motion to the fluid, creating a recirculation zone which has a stabilizing effect on the combustion. To further increase turbulence and enhance combustion performance, the two outermost passages are counter rotating to the innermost passage, resulting in an additional shear layer in between. This particular injector design has already been partly investigated by Treleaven [14] who performed a Proper Orthogonal Decomposition on the flow field of a compressible simulation. Various dominant coherent structures corresponding to helical modes were found. A local linear stability analysis was also conducted within [14], finding evidence of unstable helical modes driven by the region of high shear between the outer and inner passages of the injector. Since a local LSA is limited to parallel or weakly non-parallel flows, an assumption not valid in the inlet area of strongly swirling flows, there was little confidence in the local LSA results and it was not further pursued. However, it can be expected that a global linear stability analysis is able to find the spatial structure, frequency and growth rate of unstable modes.

Such regions of recirculating flow are known to have wavemaker characteristics, meaning regions of absolute hydrodynamic instability that trigger a global mode which induces a self-excited oscillation to the whole flow domain.

Adjoint analysis takes advantage of the adjoint equations in order to estimate the influence of a certain parameter in the equation on its solutions. It is considered a highly efficient method of optimization and sensitivity studies [67]. It has been and is increasingly applied in multiple fields of science [138]. Among those are meteorology [128, 243], nuclear reactor physics [181], seismic tomography [249], adaptive mesh refinement [129], shape optimization [82] and thermoacoustics [106, 140]. A pedagogical introduction to the topic is provided by Errico [67]. In recent years, the method has also been applied in the context of hydrodynamic stability analysis (e.g. Luchini et al. [137, 139], Giannetti and Luchini [83] Chandler et al. [30] and Tammisola and Juniper [241, 240]). A review of the method in this framework is provided by Luchini and Bottaro [138].

# CHAPTER 2

---

## Theoretical foundations

---

The governing equations describing the state of a non-reacting newtonian fluid are called the Navier-Stokes Equations (NSE), which in their compressible form are

the *conservation of mass*

$$\frac{\partial \rho}{\partial t} + \nabla \cdot \rho \mathbf{u} = 0, \quad (2.1)$$

the *conservation of momentum*

$$\rho \left( \frac{\partial \mathbf{u}}{\partial t} + \mathbf{u} \cdot \nabla \mathbf{u} \right) = -\nabla p + \nabla \cdot \underbrace{\mu \left[ \nabla \mathbf{u} + (\nabla \mathbf{u})^T - \frac{2}{3} \nabla \cdot \mathbf{u} \right]}_{\tau}, \quad (2.2)$$

and the *conservation of internal energy*

$$\rho \left( \frac{\partial (c_v T)}{\partial t} + \mathbf{u} \cdot \nabla (c_v T) \right) = -p \nabla \cdot \mathbf{u} + \nabla \cdot (\kappa \nabla T), \quad (2.3)$$

Where  $\tau$  is the viscous stress tensor. Over a broad range of applications, the perfect gas law, reading  $p = \rho R_s T$ , is used to couple density  $\rho(x,t)$ , pressure  $p(x,t)$  and temperature  $T(x,t)$ . Here, the specific gas constant  $R_s = \frac{R_m}{M}$  relates the universal gas constant to the molar mass of the fluid. With this thermodynamic equation of state, the system of partial differential equations is closed. It must be mentioned here that the energy equation can be written in many different forms depending on the application. The form seen above is used in low-Mach number flows where it is commonly written as a temperature equation, neglecting kinetic energy and heat production from viscous heating [19]. Furthermore, in reactive flows the source terms arising due to chemical reactions need to be included in the energy equation and further equations for the species transport is introduced. For a comprehensive work on the general methods of numerical combustion, the reader is referred to the work of Poinsot [19] and for a condensed summary of the combustion models used

within PRECISE-UNS a look at the work of Anand et al. [20] is recommended. Since the LSA-Solver FELiCS is based on the above equations and a detailed description of the numerical combustion scheme used in PRECISE goes beyond the framework of this thesis, Equations (2.1), (2.2) and (2.3) are placed above all following derivations and the combustion models are only briefly described in 2.1.3.

Due to the nonlinearity, in most cases and especially in industrial applications, these equations cannot be solved analytically [21]. In fact, in the three dimensional space the existence of a smooth and globally defined solution of the Navier-Stokes equations is yet to be found and is part of the millennium problems stated by the Clay Mathematics Institute. [22][23]

In engineering, this challenge is overcome by discretizing space and time and integrate the equations numerically, iterating to an approximative result. With an ever increasing processing power following Moore's Law [24], solving the Navier-Stokes equations has become extremely common in academics and industry as the most popular branch of computational fluid dynamics (CFD). While the various approaches of doing so produce results in agreement with experimental data, often the computational cost are extremely high and labourious post processing is usually necessary to extract the main features and dynamics of the flow. In Chapter 2.1, the various aspects of numerically solving the NSE are examined.

## 2.1 Computational fluid dynamics

The numerical time integration of the Navier-Stokes equations to simulate fluid flow is a commonly used tool in academics and industry with countless different CFD-Codes in use. However, as mentioned at the beginning, with high Reynolds Numbers and consequently arising turbulent fluctuations, the length and time scales become increasingly small making it exceedingly expensive to completely resolve the flow field on the computational grid. In fact, the direct numerical simulation (DNS) approach is so costly that it is projected to remain limited to small domains and low Reynolds numbers at least in the near future and is therefore of secondary interest in the industrial context. In the face of a limited computational power and cost awareness in industry, the equations are either solved for the statistical mean values with a complete modeling of turbulent influence on the flow (RANS) or they are solved with a spacial filtering, resolving large turbulent structures and modeling the sub grid scale eddies (LES). In both cases, the equations need to be closed with a turbulence model.

### 2.1.1 Reynolds-averaged Navier-Stokes

To obtain the Reynolds-Averaged equations [25], the instantanious values of the fluid are decomposed into a mean and a fluctuating part reading

$$\mathbf{q} = \bar{\mathbf{q}} + \mathbf{q}', \quad (2.4)$$

where  $\bar{\mathbf{q}}$  and  $\mathbf{q}'$  indicate time-averaged and fluctuating quantities relative to the mean field respectively. Inserting Equation (2.4) into the conservation equation for mass (Equation (2.1)) and time-averaging yields

$$\nabla \cdot (\bar{\rho} \bar{\mathbf{u}}) + \nabla \cdot (\overline{\rho' \mathbf{u}'}) = 0, \quad (2.5)$$

with a new term  $\nabla \cdot (\overline{\rho' \mathbf{u}'})$  indicating a nonlinear correlation of fluctuating density and velocity. To avoid modeling of this unknown term, CFD codes usually prefer a mass-weighed average (Favre average) over a Reynolds average [19] which is defined by

$$\hat{q} = \frac{\bar{\rho} \bar{q}}{\bar{\rho}}, \quad (2.6)$$

with the instantaneous field decomposed into favre averaged and fluctuating quantity reading

$$q = \hat{q} + q''. \quad (2.7)$$

Applying the Favre average on Equation (2.1) and taking the temporal mean, the equation of mass reads

$$\nabla \cdot (\bar{\rho} \hat{\mathbf{u}}) = 0. \quad (2.8)$$

The same formalism inserted into the conservation equation of momentum (Equation (2.2)) yields

$$\bar{\rho} \left( \frac{\partial \hat{\mathbf{u}}}{\partial t} + \hat{\mathbf{u}} \cdot \nabla \hat{\mathbf{u}} \right) = -\nabla \bar{p} + \nabla \cdot [\hat{\boldsymbol{\tau}} - \widehat{\rho \mathbf{u}'' \mathbf{u}''}], \quad (2.9)$$

[19] with a new arising term,  $\widehat{\rho \mathbf{u}'' \mathbf{u}''}$ , which resembles the modulation of the mean flow due to turbulent fluctuations. These so called Reynolds stresses have a diffusion like property similar to the viscous stress tensor  $\boldsymbol{\tau}$ . In other words, while the viscous stress describes momentum transfer on a molecular level, the Reynolds stresses stem from momentum transfer due to turbulent motion. This statistical tensor is ultimately unknown and deriving its values from new continuity equations leads to more and more unknown quantities. Consequently, without further information the set of Reynolds or Favre averaged equations governing the flow cannot be solved [26]. This closure problem is usually addressed with the *Boussinesq turbulent viscosity* assumption, relating the Reynolds stresses to the viscous tensor,  $\boldsymbol{\tau}$ , introducing a turbulent eddy viscosity,  $\mu_t$ , reading

$$\widehat{\rho \mathbf{u}'' \mathbf{u}''} = -\mu_t \left[ \nabla \hat{\mathbf{u}} + (\nabla \hat{\mathbf{u}})^T - \frac{2}{3} \nabla \cdot \hat{\mathbf{u}} \right] + \frac{2}{3} \bar{\rho} k. \quad (2.10)$$

Here, the last term denotes the turbulent kinetic energy

$$k = \frac{1}{2} \widehat{\rho \mathbf{u}'' \mathbf{u}''}. \quad (2.11)$$

Inserting Equation (2.10) into the momentum equation results in an effective viscosity,  $\mu_{\text{eff}} = \mu + \mu_t$ , which can be significantly larger than just the laminar viscosity. Using this approach, the only quantity remaining to be modeled is the turbulent viscosity. The simplest models use algebraic expressions to calculate  $\mu_t$  from mean values, while the more sophisticated one- or two-equation models define and solve additional transport equations. Most commonly the two-equation  $k - \varepsilon$  model is applied, where additional transport equations for the turbulent kinetic energy,  $k$ , and the turbulent dissipation,  $\varepsilon$ , are solved, from which the turbulent viscosity is calculated reading

$$\nu_t = C_\mu \frac{k^2}{\varepsilon}. \quad (2.12)$$

### 2.1.2 Large-eddy simulation

The methodology of LES is based on the same equations as RANS however includes a spatial filtering operation applied to the instantaneous quantities which is for non-uniform density flows according to [19] defined as

$$\bar{\rho}\bar{q}(x) = \int \rho q(x') G(x - x') dx'. \quad (2.13)$$

$G(x - x')$  denotes a spatial filter function e.g. a rectangular or a gaussian function. While it's possible to vary the scale of resolved quantities, according to Pope [26], a well-resolved LES should resolve approximately 80 % of the turbulent kinetic energy [14].

Deploying the LES filter operation on the instantaneous equation of state yields a set of equations with formal resemblance to the Favre or Reynolds filtered equations derived in Chapter 2.1.1. Consequently, a term denoting the sub-grid-scale influence of turbulent motion on the resolved flow remains to be modeled. This sub-grid-scale viscosity is assumed to be isotropic and to be dependent on the local strain rate and mesh size. Hence, LES assumes that the unresolved scales of turbulent motion act only locally. Comparing LES to RANS, the most obvious difference is the possibility to investigate unsteady motion evolving in time and the significantly smaller amount of turbulent motion to be modeled leading to a higher accuracy. Moreover, with an unsteady simulation, the post-processing of time series with data-based modal analysis is possible.

### 2.1.3 Combustion modeling

One method to take combustion into account in numerical simulations is introducing additional transport equations for the species fraction and adding source terms for the enthalpy released from the chemical reaction to the energy equation. Since it is impractical to simulate all of the numerous species involved in the combustion, a reduced reaction mechanism need to be implemented. Within the computation of the reacting flow fields in this thesis, the Flamelet Generated Manifold (FGM) method is used to reduce the number of species and model the flame. Within this approach it is assumed that the timescale of the chemical reaction is so small that fluctuations of the flow field do not

impact the flame structure. Since the flame itself is extremely thin, a one-dimensional model can be applied to calculate the diffusion and convection effects directly. To then account for the turbulence chemistry interaction, a method called Presumed Probability Density Function is deployed, representing the relationship between the species and their variance as a probability density function [14].

## 2.2 Linear stability analysis

The governing equations of hydrodynamic instabilities are derived from the Navier-Stokes equations describing conservation of mass (Equation (2.1)), momentum (Equation (2.2)) and energy (Equation (2.3)) in their compressible form. As mentioned earlier, with a flame being present, additional equations of species transport needs to be solved and the heat release due to the chemical reaction has to be included in the energy equation. However, in a linear and low-mach environment it is assumed to be sufficient to neglect the above and proceed to take the combustion into account by deploying an equation describing the non-uniform density, as demonstrated by Kaiser [27]. By taking Equations (2.1) - (2.3) and the perfect gas law,  $p = \rho R_s T$ , as a foundation and introducing further thermodynamic relations

$$c_p - c_v = R_s, \quad (2.14)$$

and

$$\frac{c_p}{c_v} = \gamma, \quad (2.15)$$

the internal energy equation can be rewritten as

$$\frac{\rho}{\gamma - 1} \left( \frac{\partial}{\partial t} \left( \frac{p}{\rho} \right) + \mathbf{u} \cdot \nabla \left( \frac{p}{\rho} \right) \right) = -p \nabla \cdot \mathbf{u} + \frac{\kappa}{R_s} \Delta \left( \frac{p}{\rho} \right). \quad (2.16)$$

This transformation is valid under the assumption of constant isochoric and isobaric specific heat capacities and specific gas constant. Furthermore, since the assumption of a low mach number flow allows for a decoupling of pressure and density, the pressure is solely described by the constant thermodynamic pressure of the deflagration. Hence, it can be pulled in front of the differential operators. Applying the chain rule of derivation and multiplying by  $\frac{\gamma-1}{p}$  yields

$$-\underbrace{\frac{1}{\rho} \left( \frac{\partial \rho}{\partial t} + \mathbf{u} \cdot \nabla \rho \right)}_{-\rho \nabla \cdot \mathbf{u}} = -(\gamma - 1) \nabla \cdot \mathbf{u} + \frac{\kappa}{c_v} \left( \frac{2}{\rho^3} \nabla \rho \cdot \nabla \rho - \frac{1}{\rho^2} \Delta \rho \right). \quad (2.17)$$

When applying the product rule of derivation on the mass conservation (2.1) one sees that the bracketed LHS term can be rewritten as pointed out. Rearranging the equation and multiplying by  $\rho^3$  finally yields Equation (2.18) coupling density to the velocity which replaces Equation (2.3) henceforth.

$$\gamma \rho^3 \nabla \cdot \mathbf{u} = \frac{k}{c_v} (2 \nabla \rho \cdot \nabla \rho - \rho \Delta \rho) \quad (2.18)$$

Together with Equations (2.1) and (2.2), Equation (2.18) describe the dynamics of a fluid with non-homogenous density due to a flame being present. In the cold flow configurations discussed within this thesis, the field is isothermal resulting in a homogenous density which makes the last equation dispensable and simplifies mass and momentum conservation resulting in the following two equations

$$\begin{aligned} \nabla \cdot \mathbf{u} &= 0 \\ \rho \left( \frac{\partial \mathbf{u}}{\partial t} + \mathbf{u} \cdot \nabla \mathbf{u} \right) &= -\nabla p + \mu \Delta \mathbf{u} \end{aligned} \quad (2.19)$$

### Linearization

To deploy a Linear Stability Analysis, the previously derived governing equations need to be linearized around the mean flow. An appropriate method to do so is the triple decomposition, first suggested by Hussain and Reynolds [28] to describe the evolution of organized waves in turbulent shear flows. This ansatz decomposes the instantanious field into a mean, a periodic and a stochastic motion, reading

$$\mathbf{q} = \bar{\mathbf{q}} + \tilde{\mathbf{q}} + \mathbf{q}'. \quad (2.20)$$

The overline resembles a time average whereas the tilde stands for a phase average defined as an ensemble average of any point in space at a particular phase [5]. The insertion of this decomposition in the respective set of equations and the subsequent averaging procedures generate additional terms similar to those occurring in the RANS approach in 2.1.1. To outline the method and to distinguish between the arising terms and their handling, Equation (2.20) is exemplary inserted into the mass conservation equation (Equation (2.1)) yielding

$$\frac{\partial \bar{\rho}}{\partial t} + \frac{\partial \tilde{\rho}}{\partial t} + \frac{\partial \rho'}{\partial t} + \nabla \cdot ((\bar{\rho} + \tilde{\rho} + \rho')(\bar{\mathbf{u}} + \tilde{\mathbf{u}} + \mathbf{u}')) = 0. \quad (2.21)$$

Multiplying out the second term and deploying a phase  $\langle \cdot \rangle$  or time  $\bar{\cdot}$  average respectively yields

$$\text{phase averaged: } \frac{\partial \tilde{\rho}}{\partial t} + \nabla \cdot \bar{\rho} \bar{\mathbf{u}} + \nabla \cdot (\bar{\rho} \tilde{\mathbf{u}}) + \nabla \cdot (\tilde{\rho} \bar{\mathbf{u}}) + \nabla \cdot \langle \tilde{\rho} \tilde{\mathbf{u}} \rangle + \nabla \cdot \langle \rho' \mathbf{u}' \rangle. \quad (2.22)$$

$$\text{time averaged: } \nabla(\bar{\rho} \bar{\mathbf{u}}) + \nabla \cdot \bar{\rho} \tilde{\mathbf{u}} + \nabla \cdot \bar{\rho}' \mathbf{u}'. \quad (2.23)$$

By subtracting Equation (2.23) from Equation (2.22), the mass conservation equation describing coherent motion on a mean field is obtained reading

$$\frac{\partial \tilde{\rho}}{\partial t} + \nabla \cdot (\bar{\rho} \tilde{\mathbf{u}}) + \nabla \cdot (\tilde{\rho} \bar{\mathbf{u}}) + \nabla \cdot \left( \langle \tilde{\rho} \tilde{\mathbf{u}} \rangle - \bar{\rho} \bar{\mathbf{u}} \right) + \nabla \cdot \left( \langle \rho' \mathbf{u}' \rangle - \bar{\rho}' \bar{\mathbf{u}}' \right) = 0. \quad (2.24)$$

In this equation, the last two terms on the LHS denote a nonlinear correlation of velocity and density fluctuations similar to the last term in Equation (2.5) within the RANS framework. While this issue is commonly tackled by introducing a Favre average in RANS, non-vanishing terms in the phase average avert this method to be of success here. Following [27], the effect of those terms is assumed to be negligible, leading to

$$\frac{\partial \tilde{\rho}}{\partial t} + \nabla \cdot (\bar{\rho} \tilde{\mathbf{u}}) + \nabla \cdot (\tilde{\rho} \bar{\mathbf{u}}) = 0. \quad (2.25)$$

Consequently, deploying the same method on the momentum conservation equation leads to numerous additional terms of similar nonlinear nature. However, due to the convective term on the LHS, apart from nonlinear terms including the fluctuating density, also terms of nonlinear velocity fluctuation arise. Following the work of Kaiser [27], these terms are assumed to be significantly larger than those including the fluctuating density and are therefore not to be omitted, leading to a momentum equation reading

$$\bar{\rho} \left( \frac{\partial \tilde{\mathbf{u}}}{\partial t} + \bar{\mathbf{u}} \cdot \nabla \tilde{\mathbf{u}} + \tilde{\mathbf{u}} \cdot \nabla \bar{\mathbf{u}} \right) + \tilde{\rho} \left( \bar{\mathbf{u}} \cdot \nabla \bar{\mathbf{u}} \right) + \bar{\rho} \left[ \nabla \cdot \left( \langle \tilde{\mathbf{u}} \tilde{\mathbf{u}} \rangle - \bar{\tilde{\mathbf{u}}} \bar{\tilde{\mathbf{u}}} \right) + \underbrace{\nabla \cdot \left( \langle \mathbf{u}' \mathbf{u}' \rangle - \bar{\mathbf{u}}' \bar{\mathbf{u}}' \right)}_{\boldsymbol{\tau}'} \right] = \nabla \tilde{p} + \nabla \cdot \boldsymbol{\tau}. \quad (2.26)$$

The nonlinear terms are noted in square brackets and represent the influence of coherent and turbulent fluctuations on the linear evolution of coherent structures on the mean field. Making use of the assumption that a time averaged mean field is already modulated by the coherent Reynold stresses, ( $\langle \tilde{\mathbf{u}} \tilde{\mathbf{u}} \rangle - \bar{\tilde{\mathbf{u}}} \bar{\tilde{\mathbf{u}}}$ ), this term is neglected and only the last term denoted as  $\boldsymbol{\tau}'$  remains to be evaluated [29]. By comparing the equations of hydrodynamic instability to the RANS equations from Chapter 2.1.1, one recognizes  $\boldsymbol{\tau}'$  as formally similar to the Reynolds stresses, which have viscous characteristics stemming from the momentum transfer due to turbulent motion. In the linear framework, the term represents the oscillations of small scale turbulent motion during the passage of the coherent structure. Similar to RANS, this term is unknown, making the equations of hydrodynamic instability an unclosed set of equations. Since the mean field is already known before conducting an LSA, it might seem practical to neglect those terms and continue to only take into account the damping due to the molecular viscosity. However, as stated in [27] and observed within the framework of this thesis, this leads to spurious modes arising in the LSA eigenvalue spectrum, making a differentiation between physical and non-physical modes impractical. Following the same Boussinesq turbulent viscosity ansatz as in RANS (Equation (2.10)),

both terms can be expressed as a viscous like term, relating  $\boldsymbol{\tau}'$  to the mean strain rate and turbulent kinetic energy,  $k$ , specified by

$$\begin{aligned}\langle \mathbf{u}'\mathbf{u}' \rangle &= -\nu_t^c \left[ \nabla \mathbf{u} + (\nabla \mathbf{u})^T - \frac{2}{3} \nabla \cdot \mathbf{u} \right] + \frac{2}{3} \langle k \rangle \mathbf{I}. \\ \overline{\mathbf{u}'\mathbf{u}'} &= -\nu_t^t \left[ \nabla \mathbf{u} + (\nabla \mathbf{u})^T - \frac{2}{3} \nabla \cdot \mathbf{u} \right] + \frac{2}{3} \bar{k} \mathbf{I}.\end{aligned}\quad (2.27)$$

Based on this, Rukes et al. [30] showed that these expressions can be reduced to

$$\boldsymbol{\tau}' = \langle \mathbf{u}'\mathbf{u}' \rangle - \overline{\mathbf{u}'\mathbf{u}'} = \nu_t \left[ \nabla \tilde{\mathbf{u}} + (\nabla \tilde{\mathbf{u}})^T - \frac{2}{3} \nabla \cdot \tilde{\mathbf{u}} \right]. \quad (2.28)$$

This term can then be introduced to the governing equations, where it is added to the viscous stress tensor,  $\boldsymbol{\tau}$ , so that

$$\tilde{\boldsymbol{\tau}} = \boldsymbol{\tau} + \boldsymbol{\tau}' = \nu_{\text{eff}} \left[ \nabla \tilde{\mathbf{u}} + (\nabla \tilde{\mathbf{u}})^T - \frac{2}{3} \nabla \cdot \tilde{\mathbf{u}} \right], \quad (2.29)$$

where  $\nu_{\text{eff}}$  denotes the effective viscosity as the sum of molecular and turbulent viscosity. Additional to those two, in LES data there is also a sub-grid scale (SGS) viscosity to account for, which results from the unresolved and therefore modeled turbulent fluctuations. The value is typically small but can easily be extracted from LES datasets such that  $\nu_{\text{eff}} = \nu + \nu_t + \nu_{\text{SGS}}$ . Consequently, before conducting an LSA, a way must be found to describe the turbulent viscosity. One fairly simple but commonly used solution is the addition of an arbitrary value for  $\nu_t$  which significantly decreases the Reynolds number of the system, hence damping unwanted oscillations but also possibly filtering out physical ones. A more sophisticated approach is an eddy viscosity calculation based on the turbulent kinetic energy  $k = \frac{1}{2}(\overline{u_i u_i})$  which can be extracted from the given datasets. This and further approaches are evaluated in the next section.

To conclude the derivation of governing equations for hydrodynamic instabilities, the full set of equations for non-uniform density flows is given as

$$\begin{aligned}\frac{\partial \tilde{\rho}}{\partial t} + \nabla \cdot (\bar{\rho} \tilde{\mathbf{u}}) + \nabla \cdot (\tilde{\rho} \bar{\mathbf{u}}) &= 0 \\ \bar{\rho} \left( \frac{\partial \tilde{\mathbf{u}}}{\partial t} + \bar{\mathbf{u}} \cdot \nabla \tilde{\mathbf{u}} + \tilde{\mathbf{u}} \cdot \nabla \bar{\mathbf{u}} \right) + \tilde{\rho} \left( \bar{\mathbf{u}} \cdot \nabla \bar{\mathbf{u}} \right) &= \nabla \tilde{p} + \nabla \cdot \mu_{\text{eff}} \left[ \nabla \tilde{\mathbf{u}} + (\nabla \tilde{\mathbf{u}})^T - \frac{2}{3} \nabla \cdot \tilde{\mathbf{u}} \right] \\ \gamma \bar{\rho}^3 \nabla \cdot \tilde{\mathbf{u}} + 3 \bar{\rho}^2 \tilde{\rho} \nabla \cdot \bar{\mathbf{u}} &= \frac{\kappa}{c_v} (\bar{\rho} \Delta \tilde{\rho} + \tilde{\rho} \Delta \bar{\rho} - 4 \nabla \tilde{\rho} \nabla \bar{\rho})\end{aligned}\quad (2.30)$$

Note that with a constant density flow all density fluctuations vanish, thus the last equation is omitted while the mass governing equation reduces to  $\nabla \cdot \tilde{\mathbf{u}}$  and the divergence terms in the momentum equation equal zero.

### Turbulent viscosity model

As shown in the preceding section, the linearization of governing equations by means of triple decomposition results in additional nonlinear terms of stochastic and coherent interaction (Equation (2.26)). These terms are ultimately unknown and pose a closure problem to the set of equations, which has to be addressed in a proper way. While in laminar flows with low Reynolds numbers such terms are often neglected, in the highly turbulent configuration dealt with in this thesis they require modeling. An often used ansatz is to express these terms as viscous like, relating them to the mean strain rate tensor and a turbulent viscosity as shown in Equation (2.28). The equations are then solved with an effective viscosity  $\nu_{\text{eff}} = \nu + \nu_t + \nu_{\text{SGS}}$ , where  $\nu$  denotes the molecular kinematic viscosity and  $\nu_{\text{SGS}}$  the sub-grid scale viscosity which is calculated within the LES. Hence, the only property left unknown is the turbulent eddy viscosity.

In the framework of LSA on turbulent mean flows, various eddy-viscosity closure models have been applied in recent years, but a favorable method is yet to be established. Those models can be fairly simply, e.g. by choosing an arbitrary constant value for  $\nu_t$  two or three orders of magnitude higher than the molecular kinematic viscosity. Other approaches are based on the Prandtl mixing length model, relating the eddy viscosity to a length scale and the mean rate of strain tensor. A more sophisticated approach with its roots in RANS calculation relates the eddy viscosity to the turbulent kinetic energy and the turbulent dissipation rate, similar to Equation (2.12). Rukes et al. [30] investigated different eddy viscosity models within a local linear stability analysis and found that in their case the most accurate results are obtained with an approximate least-square approach based on the full Reynolds stress tensor and the mean strain rate. However, transferring this to the application on RANS flow fields is not feasible since the Reynolds stress tensor is not extractable from the results. Besides choosing an arbitrary value for  $\nu_t$ , the method being most applicable with the given data is the RANS based calculation of eddy viscosity reading

$$\nu_t = C_\mu \frac{k^2}{\varepsilon}, \quad (2.31)$$

with  $C_\mu = 0.09$ , where following [26], in high Reynolds number flows  $\varepsilon$  can be written as

$$\varepsilon = \frac{C_\mu^{0.75} k^{1.5}}{l_m}, \quad (2.32)$$

yielding the term for the eddy viscosity reading

$$\nu_t = c l_m \sqrt{k}. \quad (2.33)$$

The modeling constant is consequently defined as  $c = C_\mu^{0.25} = 0.55$  and the turbulent mixing length  $l_m$  can be defined as proportional to the size of the large scale coherent structures responsible for the majority of turbulent production reading  $l_m = c_{\text{prop}} l$ . The

proportionality constant relating the scale of the coherent structures to the mixing length is chosen to be  $c_{\text{prop}} = 0.075$  based on [31] and [32], where for axisymmetric coaxial jets it was chosen to be  $c_{\text{prop}} = 0.0705$  and  $c_{\text{prop}} = 0.082$  respectively.

This ansatz, where the turbulent viscosity is based on the turbulent kinetic energy and a length scale was independently suggested by Kolmogorov and Prandtl and a similar approach was pursued by Casel [33] in the case of a turbulent jet flow. On this simpler configuration it yielded accurate results within the framework of an LSA and Resolvent Analysis. Using this approach means including the trace of the Reynolds stress tensor,  $\overline{u'_i u'_i}$ , in the calculation but neglecting the other entries. An investigation of the full Reynolds stress tensor obtained from the cold LES snapshots however reveals that the fluctuating energy contained in the main diagonals includes 91.1% of the total energy. This indicates that the shear stresses are of secondary importance and an omission should not result in a significant error. Since the given 3D-datasets do not include the shear stresses, this is a good finding.

Calculating the turbulent viscosity by means of TKE and length scale yields a value far greater than the molecular and sub-grid-scale viscosity. The eddy viscosity is therefore the main contributor to the effective viscosity which is in agreement to preceding studies on a highly turbulent swirled injector [27].

### 2.2.1 Modal analysis

To solve for hydrodynamic instabilities, a harmonic approach for the disturbance quantities is substituted into the set of Equations (2.30), relating the three dimensional perturbations  $\tilde{\mathbf{q}}(x,y,z) = (\tilde{\mathbf{u}}(x,y,z), \tilde{p}(x,y,z), \tilde{\rho}(x,y,z))^T$  to a specific growth rate and spacial mode shape reading

$$\tilde{\mathbf{q}}(x,y,z) = \hat{\mathbf{q}}(x,y,z)e^{-i\omega t}, \quad (2.34)$$

with  $\omega_r$  denoting the frequency and  $\omega_i$  the growth rate where  $\omega_i > 0$  indicates a global instability growing in time. Inserting this term into the set of governing equations yields a three dimensional, cartesian system to be solved. When analyzing a mean field of a cylindrical swirled combustor it is however feasible to use cylindrical coordinates allowing to reduce the dimension by one, since the assumption of a homogenous azimuthal direction is valid. By further assuming that the perturbations are harmonic in azimuthal direction, Equation (2.34) can be rewritten as

$$\tilde{\mathbf{q}}(x,r,\Theta) = \hat{\mathbf{q}}(x,r)e^{i(m\Theta - \omega t)}, \quad (2.35)$$

where  $m$  is the azimuthal wave number which corresponds to an axi-symmetric instability when  $m = 0$  or an  $m$ -armed skew-symmetric (helical) structure when  $|m| > 0$ . Hence, within the framework of LSA, the flow can be separately analyzed for different azimuthal wave numbers. Deploying this reduced modal ansatz on the set of equations and building linear operators yields a generalized eigenvalue problem, reading

$$\mathbf{A}\hat{\mathbf{q}}(x,r) = \omega\mathbf{B}\hat{\mathbf{q}}(x,r), \quad (2.36)$$

where  $\mathbf{A}$  and  $\mathbf{B}$  are defined by

$$\mathbf{B} = \begin{bmatrix} 0 & 0 & i \\ i\bar{\rho} & 0 & 0 \\ 0 & 0 & 0 \end{bmatrix} \quad (2.37)$$

$$\mathbf{A} = \begin{bmatrix} \bar{\rho}\nabla \cdot (\ ) + (\ ) \cdot \nabla \bar{\rho} & 0 & (\ )\nabla \cdot \bar{\mathbf{u}} + \bar{\mathbf{u}} \cdot \nabla (\ ) \\ -\nabla \cdot \mu_{\text{eff}}[\nabla + \nabla^T](\ ) - \frac{2}{3}\nabla \cdot (\ ) & \nabla(\ ) & (\ )( \bar{\mathbf{u}} \cdot \nabla \bar{\mathbf{u}} ) \\ \gamma\bar{\rho}^3\nabla \cdot (\ ) & 0 & (\ )^3\bar{\rho}^2\nabla \cdot \bar{\mathbf{u}} - \frac{\kappa}{c_v}(\bar{\rho}\Delta(\ ) + (\ )\Delta\bar{\rho} - 4\nabla(\ )\nabla\bar{\rho}) \end{bmatrix} \quad (2.38)$$

This eigenvalue problem is numerically discretized and solved with the Finite Element Method (FEM), yielding a spectrum of eigenvectors and eigenvalues. Each of those refer to a spacial mode shape ( $\hat{\mathbf{q}}(x,r)$ ), a growth rate ( $\text{Re}\{\omega\}$ ) and a frequency ( $\text{Im}\{\omega\}$ ) and can give insights into intrinsic instabilities of the given mean field. An eigenvalue with a positive growth rate indicates a global mode whose amplitude will increase with time, whereas an eigenvalue with a negative growth rate indicates a damped mechanism. Within the linear analysis of mean fields, a global mode associated to a large-scale coherent structure is expected to yield a growth rate around  $\omega_i = 0$ . This seems intuitive since the underlying flow is in a stationary state, meaning that the unsteady coherent structure present in the flow is oscillating in a limit cycle without any further increase in amplitude. Since the influence of the large-scale turbulent motion is incorporated in the temporal mean field, a mean flow LSA should find a marginally stable ( $\omega_i = 0$ ) or weakly damped global mode [4].

### Adjoint Modes

For every direct eigenvalue problem stated in the form of Equation (2.41), there exists an adjoint eigenvalue problem reading

$$\mathbf{A}\hat{\mathbf{q}}^\dagger(x,r) = \omega^\dagger \mathbf{B}\hat{\mathbf{q}}^\dagger(x,r). \quad (2.39)$$

Solving this eigenvalue problem results in a set of adjoint eigenvalues and eigenvectors each corresponding to a solution of Eqn. (2.41). These adjoint modes can give information about the location of the strongest feedback of the corresponding direct mode. Since the location of strongest feedback is often spatially separated from the location of strongest perturbation amplitude, Giannetti and Luchini [34] proposed a term,  $\sigma$ , to couple the absolute values of direct and adjoint mode reading

$$\sigma = \frac{||\hat{\mathbf{q}}^\dagger|| ||\hat{\mathbf{q}}||}{\int \hat{\mathbf{q}}^\dagger \cdot \hat{\mathbf{q}} dS}. \quad (2.40)$$

This structural sensitivity is a measure for internal feedback strength and hence regions with a high  $\sigma$  can be seen as the origin of global instabilities. In practical terms, a parameter optimization based on the adjoint equations is therefore an effective way to identify the regions where design changes have the largest impact on inherent instabilities.

### 2.2.2 Resolvent analysis

Resolvent analysis (RA) is a method to investigate the flow fields hydrodynamic response to harmonic forcing. While the modal LSA gives insights into intrinsic mechanisms, the RA can be seen as an extension that is able to describe the growth of external perturbations imposed on the flow field. These non-modal linear mechanisms can grow to significant amplitudes, even when no eigenvalue was found to be unstable or marginally stable. Mathematically speaking, a linear forcing term,  $\tilde{f}$ , is added to the momentum equation of hydrodynamic instabilities (Equation (2.30)), resulting in an extended eigenvalue problem reading

$$\mathbf{A}\hat{\mathbf{q}}(x,r) = \omega \mathbf{B}\hat{\mathbf{q}}(x,r) + \mathbf{P}\hat{f}(\omega), \quad (2.41)$$

where  $\mathbf{P} = [1,0,0]^T$ . By rearranging the linear operators  $\mathbf{A}$ ,  $\mathbf{B}$  and  $\mathbf{P}$ , this term provides a link between the linear forcing term  $\hat{f}(\omega)$  and the response  $\hat{\mathbf{q}}(x,r)$ :

$$\hat{\mathbf{q}}(x,r) = (\mathbf{A} - \omega \mathbf{B})^{-1} \mathbf{P} \hat{f}(\omega) = \mathfrak{R}\hat{f}(\omega). \quad (2.42)$$

Here,  $\mathfrak{R}$  denotes the resolvent operator around the mean flow.

A following Singular Value Decomposition (SVD) of  $\mathfrak{R}$  then yields right singular vectors and left singular vectors which are proven to resemble optimal forcings,  $\tilde{\phi}$ , and optimal responses,  $\tilde{\psi}$ , respectively [35]. To investigate the receptibility to external forcing, the energy gain between forcing and response is in the framework of this study defined as

$$\mu_j^2(\omega) = \frac{||\tilde{\phi}||^2}{||\tilde{\psi}||^2} = \frac{\int_{\Omega} \tilde{\phi} \mathbf{R} d\Omega}{\int_{\Omega} \tilde{\psi} \mathbf{R} d\Omega}, \quad (2.43)$$

with  $\mathbf{R} = [1,0,0]^T$  to solely incorporated velocity fluctuations in the gain calculation. When

this gain is large, small perturbations at a particular frequency are expected to grow to large amplitudes. If for a given frequency the first gain value is significantly larger than the following - the so called low-rank condition - the spacial structure of the instability at this frequency is assumed to be represented by the dominant optimal response and forcing pair [35]. When conducted over a whole range of frequencies, the RA yields a gain spectrum that shows at which forcing frequencies the amplification is maximal.

## 2.3 Data-based analysis

The three methods of empirical mode decomposition applied within the framework of this thesis are fast Fourier transform (FFT), proper orthogonal decomposition (POD) and spectral proper orthogonal decomposition (SPOD). Based on a large set of time dependent instantaneous snapshots, a zero-mean fluctuating flow field is decomposed into a finite amount of spacially and temporally independent modes. Each of those snapshots denoted by  $\mathbf{q}^n(x,t) = [\mathbf{u}_x, \mathbf{u}_y, \mathbf{u}_z]^T$  comprises the flow quantities at discrete points in space at a given time. The methods then yield a modal decomposition of the process, which gives insights into the main features present in the flow field. Similar to the modal LSA, when applied on a rotational symmetric flow field the dominant modes can be characterised by their azimuthal wave number, where  $m = 0$  represent axisymmetric structures and  $|m| > 0$  represent helical structures with  $m$  arms. The sign of  $m$  denotes the rotation direction of a particular instability.

Since a full derivation of the mathematical groundwork goes beyond the scope of this thesis, the methods are briefly described in practical terms and the reader is referred to relevant literature in the respective section.

### 2.3.1 Fast Fourier transform

A Fourier transform of a two dimensional flow field transforms the time-series of  $N$  snapshots from physical space into a spectral representation of  $N$  Fourier coefficients in spectral space [26]. To conduct an FFT, the time-series of individual observations  $\mathbf{q}(x,t)$  is lined up in a snapshot matrix reading

$$\mathbf{Q} = \begin{bmatrix} | & | & | \\ \mathbf{q}^{(1)} & \mathbf{q}^{(2)} & \dots & \mathbf{q}^N \\ | & | & & | \end{bmatrix} \quad (2.44)$$

The construction of this snapshot matrix then allows for a row-wise FFT, meaning that the FFT is performed for each spacial point over its time dimension reading

$$\hat{\mathbf{q}}^k = \sum_{n=1}^N \mathbf{q}^n e^{-i \frac{2\pi}{N} kn}, \quad k = -N/2 + 1, \dots, N/2. \quad (2.45)$$

Each of the  $k$  Fourier modes represent a spacial mode shape corresponding to a harmonic oscillation at the discrete frequency  $f_k = \frac{k}{N} F_s$  with  $F_s$  denoting the sampling frequency.

Note that  $\hat{\mathbf{q}}^k$  is now a complex quantity. The energy content of the flow field by frequency can then be extracted by calculating the integral Power Spectral Density over the whole domain. Frequencies with a distinct peak in the PSD can be associated to a dominant oscillating mechanism. Advantages of the FFT are its relatively low computational effort and the fact that the physical interpretation of the modes is unambiguous since every mode has a fixed oscillation frequency. This strict separation by frequency however can also be undesirable when it comes to coherent structures in turbulent flows, as their frequency spectrum is oftentimes not monochromatic and the structure gets distributed over various discrete frequency steps in the FFT, making it difficult to analyse dominant structures and their energy content in turbulent flows.

### 2.3.2 Proper orthogonal decomposition

Proper orthogonal decomposition was first introduced in the context of turbulence in 1967 [36], and since then has become one of the most common empirical methods to extract coherent structures from turbulent flows. The method seeks to approximate the dynamics of the flow by finding an orthogonal basis, such that a subset of  $N_s$  modes contains more energy than any other orthogonal basis. This subset of modes is defined by

$$\mathbf{q}(x,t) \approx \sum_{i=0}^{N_s} \Psi_i(t) \phi_i(x) \quad (2.46)$$

and approximates the dynamic of the flow in an optimal way. As depicted, a mode is comprised of a temporal coefficient independent in space and a spacial shape independent in time. The starting point for a POD is again the snapshot matrix  $\mathbf{Q}$ :

$$\mathbf{Q} = \begin{bmatrix} | & | & | \\ \mathbf{q}^{(1)} & \mathbf{q}^{(2)} & \dots & \mathbf{q}^N \\ | & | & & | \end{bmatrix} \quad (2.47)$$

From here on, the so called 'method of snapshots' is further evaluated, since it is the computationally efficient method when dealing with datasets that are much larger in spacial dimension than in temporal, meaning the amount of data points per snapshots significantly exceeds the number of snapshots. Based on [37], the POD eigenvalues and eigenvectors are then given by solving the eigenvalue problem reading

$$\frac{1}{N-1} \mathbf{Q}^H \mathbf{W} \mathbf{Q} \Psi = \Psi \Lambda, \quad (2.48)$$

where the eigenvalues are contained in  $\Lambda$  and the temporal modes can be extracted from  $\Psi$ . The spacial mode shapes can be recombined from the snapshot matrix and temporal modes as  $\Phi = \mathbf{Q} \Psi$ . Here,  $\mathbf{W}$  denotes a diagonal weighting matrix, chosen to incorporate the turbulent kinetic energy and the volume associated to each point. By arranging the eigenvalues and the accompanying eigenvectors such that  $\lambda_1 > \lambda_2 > \dots > \lambda_N$ , the dominant features of the flow can be extracted. Since in turbulent flows the large-scale

structures usually contain a major portion of the turbulent kinetic energy, the eigenvalues and eigenvectors with the highest energy content can hence be expected to span the basis for the dominant coherent structures.

The POD's advantage compared to the FFT is its spacial orthogonality which results in a better identification of structures that are of similar behaviour without a strict separation by frequency. The optimality in terms of energy contained in the leading modes makes it easier to classify the extracted structures. However, with the lack of temporal correlation, the physical interpretation of a particular mode can be difficult, as the mode might be associated to a broad range of frequencies.

### 2.3.3 Spectral proper orthogonal decomposition

The SPOD combines the advantages of FFT and POD, expressing the flow dynamics as a set of modes that are orthogonal in space **and** time. Practically speaking, the SPOD can be described as several POD conducted on a snapshot matrix that was segmented, Fourier transformed and rearranged so that the eigenvalue problem is solved frequency wise. That way, the eigenvalues and eigenvectors are associated to a particular frequency and are optimal in terms of spacial coherence of the resulting structures. The following description of the method is based on the work of Schmidt and Colonius whose condensed summary of the theoretical background and the application of SPOD can be found in [37]. The practical difference to the preceding methods is an initial row-wise segmentation of the snapshot matrix  $\mathbf{Q}$  in  $N_b$  blocks of the same row number  $N_{\text{seg}}$  with an overlap of  $N_{\text{overlap}}$  yielding a three dimensional snapshot matrix  $\mathbf{Q}_{\text{SPOD}}$  where the individual blocks are stacked in the third dimension. Each block is subsequently windowed in time, with an appropriate window function. This windowing of a signal is commonly used when the PSD of a signal is computed via Welch's method and suppresses spectral leakage due to the finite length of the individual signals. Conducting a FFT on each of the  $N_b$  blocks results in the three dimensional fourier transformed snapshot matrix  $\widehat{\mathbf{Q}}$ :

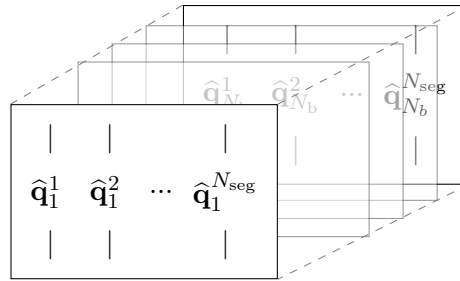


**Figure 2.1:** Three dimensional array with  $N_b$  snapshot matrices stacked in the third dimension.

Each row stacked in the third dimension now resembles one particular frequency. The remaining analysis is now performed frequency wise on each stacked row by constructing the data-matrix, which for a given frequency  $k$  is given as

$$\hat{\mathbf{Q}}^k = \begin{bmatrix} | & | & & | \\ \hat{\mathbf{q}}_1^k & \hat{\mathbf{q}}_2^k & \dots & \hat{\mathbf{q}}_{N_b}^k \\ | & | & & | \end{bmatrix} \quad (2.49)$$

Similar to POD, the next step is the construction of an eigenvalue problem for each frequency reading

$$\hat{\mathbf{Q}}^H \mathbf{W} \hat{\mathbf{Q}} \hat{\boldsymbol{\Psi}} = \hat{\boldsymbol{\Psi}} \hat{\boldsymbol{\Lambda}} \quad (2.50)$$

where again the eigenvalues are contained in  $\hat{\boldsymbol{\Lambda}}$  and the spacial mode shapes are recovered as  $\hat{\boldsymbol{\Phi}} = \hat{\mathbf{Q}} \hat{\boldsymbol{\Psi}}$ . Obtained with this algorithm is an optimal approximation of the flow dynamic at each particular frequency  $f_k = \frac{k}{N_b} F_s$ . By plotting the first few eigenvalues over the whole frequency range, one can identify regions with strong internal mechanisms when the eigenvalues have a local or global peak and show strong separation between the first and following eigenvalues [37]. In that case, the leading SPOD mode is an accurate approximation of the flow dynamics at that frequency. Furthermore, the SPOD modes and eigenvalue spectra can be connected to forced linear systems which are analyzed within the framework of the resolvent analysis. This connection, which is derived and explained thoroughly in [38], is used within the framework of this thesis to validate the RA results from Chapter 5 on empirical SPOD results.

A major disadvantage in applying the SPOD is the required amount of snapshots. Since the total sampling period is subdivided into blocks to estimate the CSD tensor, the signal needs to be much longer to obtain an appropriate frequency step in the FFT. However, when enough snapshots are present, this method combines the advantages of FFT and POD.

# CHAPTER 3

---

## Flow configuration and data-based analysis

---

In this chapter, the unsteady dynamic of the given cold and reacting flow fields is investigated by means of data-based modal decomposition. First, the LES fields are introduced and briefly described. Their RANS counterpart is shown to assess differences between the two simulation approaches. Following that, the results obtained by means of proper orthogonal decomposition (POD) and discrete Fourier transform (DFT) for both the cold and the reacting LES are presented and explained in terms of the underlying physical mechanism and with respect to the differences between the two cases. A three dimensional visualization is presented to further enhance the understanding of the structures extracted with POD and DFT. In the context of this thesis, this chapter serves as a validation for the LSA conducted in Chapter 4.

### 3.1 The flow fields

Figure 3.1 shows planes through the four flow fields that are investigated in Chapter 3 and 4 of this thesis. Pictures **a** and **b** show a cold and a reacting LES flow field, whereas **c** and **d** depict the respective RANS simulation. The RANS calculations have the same inlet conditions as their LES counterpart and are conducted to approximate the mean field of the unsteady flow. All flow fields were obtained with an incompressible finite-volume scheme on an unstructured grid with 17 million cells. The three staged injector has the same geometry in all simulations. The innermost passage emits a pilot jet on the symmetry axis, clearly visible in Figure 3.1 as the region with highest velocity. The middle and outer passages emit jets with less velocity and a radial velocity component. Together, they are referenced as the outer inlet passages. All stages have a strong azimuthal velocity component which is induced by swirl vanes. The two outer inlet passages are counter-rotating relative to the pilot axis jet, further enhancing turbulence production. The induced swirl forces the outer inlet flow away from the rotational axis, which results in an inner recirculation zone emerging between the axis jet and the outer passages and an outer recirculation zone emerging between the outer passages and the combustor wall. These recirculation zones are visible as the dark blue zones with a negative axial velocity.

The black lines in the reacting fields **b** and **d** are isocontours of the temporal mean heat release rate and indicate the flame position. The flame is stabilized in a central position downstream of the pilot axis jet, enclosed by the inner recirculation zone. In the LES, another region of high heat release in the proximity of the outer recirculation zone appears. In the reactive simulation, the fluid gets accelerated strongly in the downstream region. This is caused by the narrowing geometry and by the fluids strong expansion when a flame is present.

It is seen that neither cold nor reacting RANS accurately depict the mean field of their LES counterpart. The penetration depth of all inlet passages is much larger in RANS, whereas especially in the cold flow LES the penetration depth is short and the cone angle of the outer passages is smaller. This is attributable to the inherent inaccuracy that comes with a RANS simulation. Fluctuating motions are completely modeled in the RANS calculation, which here leads to a longer sustainment of a distinct inlet stream and larger recirculation zones. The reactive RANS seems to be more accurate with respect to its LES equivalent and the differences between those two are smaller than in the cold configuration.

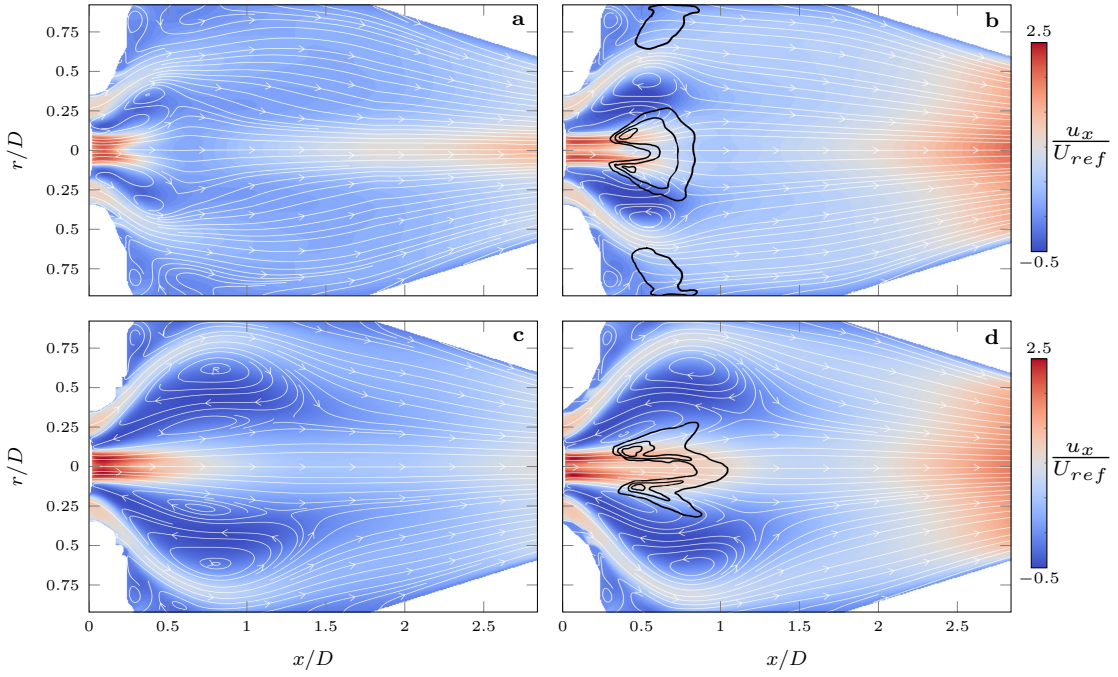


**Figure 3.1:** x-r-slices through cylindrical flow domain for cold LES (a), reacting LES (b), cold RANS (c) and reacting RANS (d). Flow direction is left to right, with the pilot jet and the outer inlet passages on the leftmost side of each figure. Streamlines represent velocity in x-r-plane. In the reacting simulation, the black lines represent isocontour of the region of highest mean heat release corresponding to the flame position.

### 3.2 POD and DFT results

To empirically analyze the underlying dynamics of the two LES flow fields, time-series of instantanious snapshots are investigated by means of proper orthogonal decomposition and discrete Fourier transform. The POD is used to find the dominant large-scale coherent structures while the latter serves as a validation to provide the POD modes with a definite physical background and oscillation frequency. To get a reliable approximation of the modal decomposition, in both cold and reacting case 800 instantanious snapshots of the x-r-plane were extracted every 50 timesteps, resulting in a temporal resolution of  $\Delta t_{\text{snap}} = 5 \cdot 10^{-5}$  s and a time period of 0.04 s leading to a fundamental frequency of  $f_{\min} = 25$  Hz and a Nyquist frequency of  $f_{\text{nyq}} = 10000$  Hz.

The resulting eigenvalues of both cold and reacting POD are depicted in Figure 3.2. In both cases, eigenvalue one and two are one order of magnitude higher than the third, fourth and following. This shows that a major fraction of the flow fields fluctuating energy is contained in the first two eigenvalues.

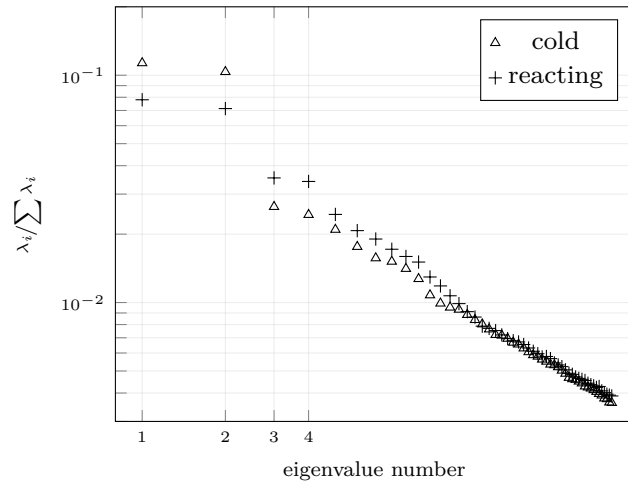


**Figure 3.2:** First 50 eigenvalues as obtained in the POD for the cold and reacting LES. The eigenvalues are sorted by relative energy in descending order. Relative energy is expressed as a fraction of cumulated energy of all eigenvalues.

Since in turbulent flows the majority of turbulent energy is usually contained in the large scale coherent structures, those high energy eigenvalues and their corresponding eigenvectors are expected to resemble the main unsteady dynamic of the underlying flow. Given the fact that eigenvalues one and two are of nearly the same energy in cold and reacting flow respectively, they can be associated to an oscillatory behaviour [10] and hence resemble the same mechanism. The third and fourth eigenvalue appear to have a similar relation to each other, however with a much lower energy. While the distribution of energy in the leading eigenvalues is qualitatively similar in cold and reacting flow, they show differences when directly compared. In the reacting simulation, the two leading

eigenvalues incorporate less relative energy than their cold counterparts, narrowing the gap between the leading two and the remaining eigenvalues. The presence of a flame apparently causes the energy of the dominant mechanism to be redistributed.

To interpret the POD eigenvalues, the spacial mode shapes corresponding to the first four eigenvalues are shown in Figure 3.3. The contour colours are normalized by the maximal value of the respective mode. Depicted is the axial velocity of the first four modes for both the cold and reacting flow.

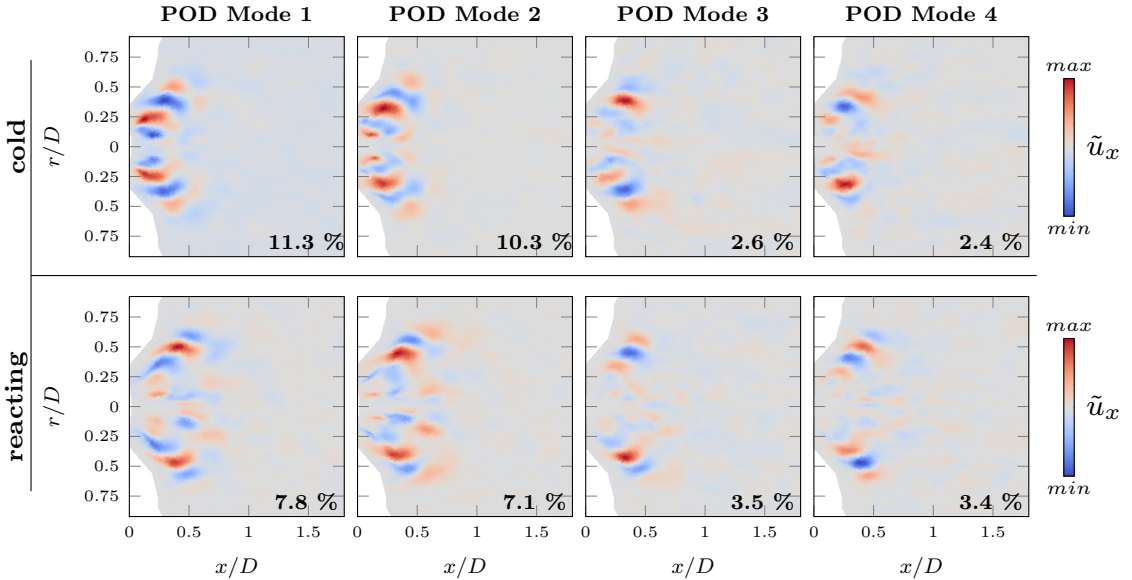


**Figure 3.3:** First four POD modes of the x-r-plane for cold and reacting simulation (upper and lower half plane respectively). Depicted is the axial velocity component. The contour colours are normalized by the maximal value of axial velocity of the respective mode. The percentage of fluctuating energy contained in each mode is written in the bottom right corner.

All modes are similar in the sense that they are located in the region of high shear between the outer inlet jet and the inner recirculation zone. They originate directly at the inlet and vanish at an axial position of  $x \approx 0.5D - 0.7D$ . Looking back to the mean field in Figure 3.1, it appears that the unsteadiness vanishes at the same axial position where the recirculation zone ends. This indicates a similar mechanism being active, no matter if a flame is present or not. The modes corresponding to the reacting flow are stretched, reaching further downstream and in radial direction. This is consistent with the larger penetration depth of the outer passages in the reacting simulation as can be seen in Figure 3.1. As already mentioned, the relative energy contained in the POD modes is different for cold and reacting flow. In the bottom right of each plot, the respective percentage of fluctuating energy is shown. For the cold flow, the energy contained in the two leading modes

is 21.7% of the cumulated fluctuating energy, whereas the energy of the third and fourth mode makes up 5% of the cumulated energy. For the reacting simulation, the two leading modes make up for 14.9% while the third and fourth mode contain 6.9% of the fluctuating energy. This indicates that with a flame present, the dominant structure gets weakened.

Mode one and two in both cold and reacting simulation are symmetric to the axis and phase shifted to each other, indicating their dependency and the fact that they represent the same mechanism. Mode three and four resemble each other in the same way but with an anti-symmetric structure. These mode structures are oftentimes found in swirled flows and are associated to Kelvin-Helmholtz instabilities, which originate in regions of high shear close to the inlet. These modes are observed as torus-like vortices in non-swirling jets and as helical vortices in strongly swirling jets [8]. 2D-Slices of helical structures with an even number of arms (2,4,...) then yields mode shapes similar to the symmetric modes 1 and 2 in Figure 3.3 whereas helical structures with an odd number of arms (1,3,...) yield mode shapes like the anti-symmetric modes 3 and 4.

To identify the number of arms or more formally the azimuthal wave number of the modes, a snapshot of the full instantaneous flow field has been examined for vortex-like structures via the Q-criterion. Deploying the Q-criterion on the flow field, the largest consecutive structure with a high vorticity can be associated to the dominant POD mode. In fact, for the cold flow this structure is found as shown in Figure 3.4 where the isocontour of the highest 5% of vorticity values shows a distinct double helix (red) winding around the axis, spatially fitting to the first POD mode.

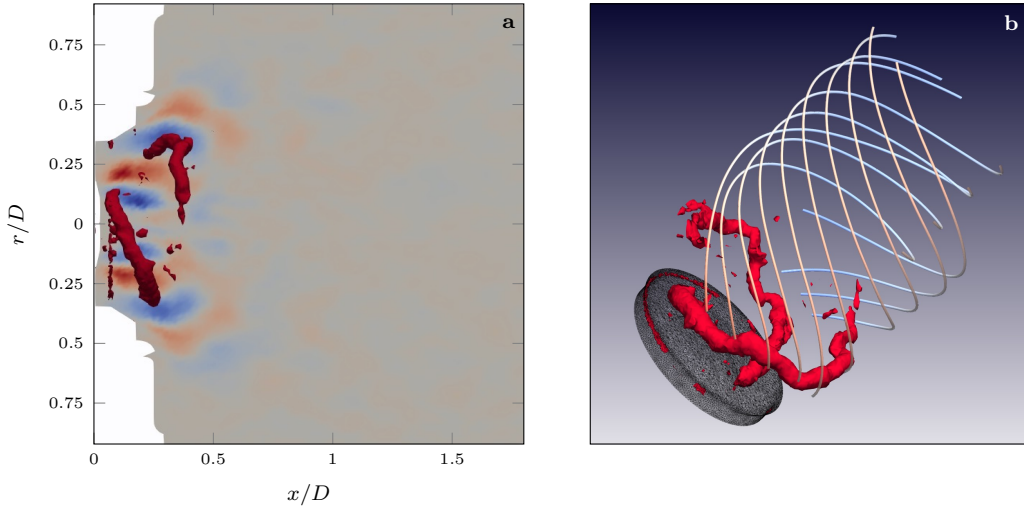


**Figure 3.4:** Isocontour of instantaneous vorticity (red) calculated by means of the Q-criterion on the cold 3D-field, overlaid with the POD planar axial velocity field (a) and streamlines of the mean velocity field (b).

Figure 3.4 (b) shows, that this helical instability is counter-winding relative to the mean flow. Concludingly, the dominant mechanism inherent to the flow field is identified as an  $m = -2$  helical instability. This is in agreement with investigations on a similar flow configuration where an  $m = -2$  instability was found to be the dominant coherent structure [14]. The reacting flow not depicted here shows a similar structure.

With the dominant coherent structure identified as an  $m = -2$  helical structure, the secondary dominant structure associated to the eigenvalues 3 and 4 remains to be classified. Furthermore, no investigation into the temporal behaviour of the flow has been made so far. This is because POD modes are optimal in an energetic sense but they lack temporal correlation. This can lead to the situation where mechanisms with a similar mode shape are resembled by the same POD mode, despite the fact that they are oscillating at different frequencies.

To clearly express spatiotemporal behaviour of the data, a DFT is conducted in addition to the POD. Each DFT mode is associated to a defined frequency bin, which supports a physical interpretation. Figure 3.5 shows the normalized PSD of the axial velocity of cold and reacting simulation integrated over all spatial points. In both cold and reacting flow fields there are the same four distinct peaks in an even pattern of  $\Delta St = 0.5$ . The energy of the mode associated to the peak at  $St = 1$  is the largest, accompanied by weaker dynamics at  $St = \{0.5, 1.5, 2, 2.5\}$ . All modes have narrow spectral bands, only the mode at  $St = 2.5$  is not identified as clearly, especially in the cold flow. The similarity of the PSD for cold and reacting flow indicates that the main flow dynamic is not strongly affected by the presence of the flame.

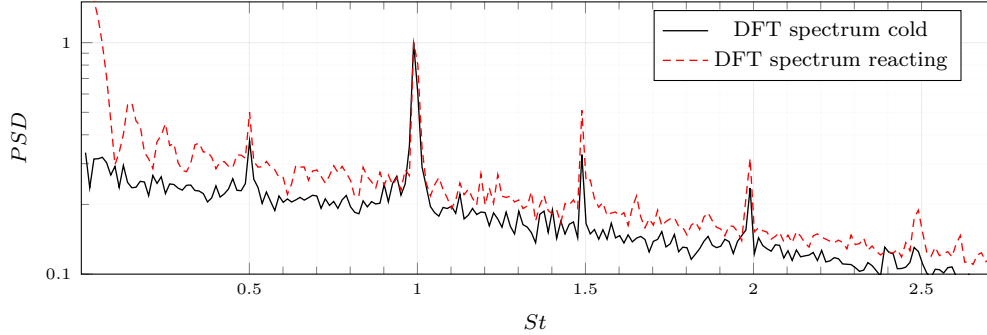


**Figure 3.5:** PSD of axial velocity of instantanious x-r-plane snapshots. The velocity of all spacial points is taken into account. The PSD is plotted over the non-dimensional Strouhal number. This dimensionless Number is defined as  $St = \frac{f \cdot D}{U_{ref}}$ , relating the oscillation frequency to a reference length and velocity. The reference values are chosen as the outermost inlet diameter and an arbitrary velocity in the range of the inlet stream velocities.

The DFT mode shapes corresponding to each of the five peaks are shown in Figure 3.5. Since the frequency bands are narrow, the DFT is able to extract the spacial shape of each mode very well. Even the less distinct mode at  $St = 2.5$  is not distorted and shows a

clear structure. The DFT mode at  $St = 1$  has the same shape as the leading POD mode in Figure 3.3. The corresponding peak in Figure 3.5 is the largest, which is in agreement with the first and second POD eigenvalue having the largest fraction of fluctuating energy. Hence, the dominant  $m = -2$  instability is oscillating at  $St = 1$ .

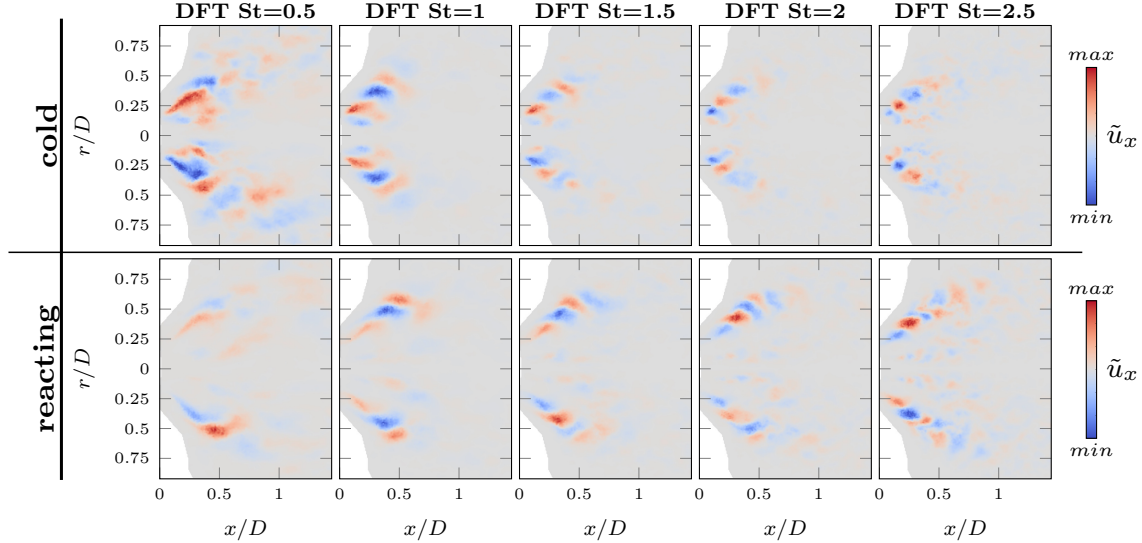


**Figure 3.6:** Axial velocity of DFT modes associated to the four main peaks in the PSD depicted in Figure 3.5. Only the real part is shown and the colours are normalized with the maximum value of the respective mode.

As mentioned earlier, certain POD modes can include mechanisms of similar shape that oscillate at various frequencies. Following that, the DFT modes at  $St = 0.5, 1.5, 2.5$  can be connected to POD modes three and four since they have a similar anti-symmetric shape. Where the POD fails to distinguish between the three mechanisms, the DFT is able to do so. In the same way, the DFT mode at  $St = 2$  appears to be included in the dominant  $m = -2$  mode, since it has a similar symmetric shape.

The appearance of numerous modes in an orderly pattern as observed here is often an indicator for one dominant mechanism at a fundamental frequency  $f$  and several higher harmonic modes at multiples  $n \cdot f$  of this fundamental frequency. This is for example the case in the sweeping jet of a fluidic oscillator as shown in [39]. For that particular case, the DFT spectrum yields one large peak at  $f$  and six smaller peaks at higher harmonic frequencies  $n \cdot f$ . These higher harmonics arise due to non-linear interaction with the fundamental mode.

In the configuration investigated within this thesis, there is one dominant structure at  $St = 1$ . Hence, higher harmonic modes would be expected at frequencies of  $St = 2, 3, 4, \dots$ . With the appearance of modes at  $St = 0.5$ ,  $St = 1.5$  and  $St = 2.5$ , a clear interpretation is difficult at this point. A possible explanation is that the dominant mode at  $St = 1$  excites

its first higher harmonic at  $St = 2$  and a subharmonic at  $St = 0.5$ . This subharmonic then excites higher harmonics at  $St = 1.5$  and  $St = 2.5$ . It is also possible that the modes are not higher harmonics but each arises linearly from the mean field. Since all modes are rotating with the mean field, this could explain their frequency correlation: The helical  $m = -2$  mode, which was identified in the flow (see Figure 3.4), would then oscillate at twice the frequency of an  $m = -1$  mode and at half the frequency of an  $m = -4$  mode. If this logic is applied on all five DFT modes, each can be associated to an azimuthal wave number from  $m = -1$  for the mode at  $St = 0.5$  to  $m = -5$  for the mode at  $St = 2.5$ .

### Conclusion

A POD and DFT is performed for snapshots of the x-r-plane of a cold and a reacting LES. Both methods are able to extract the main dynamic features of the flow which are found to be instabilities of the Kelvin-Helmholtz type, originating in the shear layer close to the inlet and travelling downstream until  $x = 0.5 - 0.7D$ . The DFT is able to distinguish between five separated modes. The most dominant structure is identified as a two-armed helix ( $m = -2$ ) oscillating at  $St = 1$ . Less dominant structures are found to be instabilities of the same type but with frequencies of  $St = \{0.5, 1.5, 2, 2.5\}$ . These modes can be associated to structures with an azimuthal wavenumbers of  $m = \{-1, -3, -4, -5\}$  respectively. A remarkable finding is the similarity of cold and reacting flow in this configuration. While the presence of a flame influences the POD and DFT mode shapes shown in Figures 3.3 and 3.6, it has no influence on the associated frequencies shown in Figure 3.5. This suggests that the instability originates in a region not influenced by the flame, most likely at an upstream position in relative large distance to the flame.

The empirical analysis carried out in this chapter serves as a validation for the Linear Stability Analysis performed in the following chapter. With the DFT showing a clear spatiotemporal behaviour of the flow, with modes at defined frequencies, the success of LSA can be measured on its capability to reproduce those modes.

# CHAPTER 4

---

## Application of Linear Stability Analysis

---

In this chapter, the LSA is applied to the LES and RANS flow fields shown in Figure 3.1. First, the technical aspects of the LSA, involving mesh generation and boundary conditions (BC), are discussed in Chapter 4.1. The principles of the underlying FEM method is described briefly. Subsequently, the need for a turbulence model is addressed by showing the LSA results for different viscosity magnitudes in Chapter 4.2.1. The following Chapter 4.2.2 deals with the calculation of the eddy viscosity based on the turbulent kinetic energy. The results of the linear stability analysis for each of the four flow fields are presented in Chapter 4.3.1 - 4.3.4. In addition to the direct modes, the adjoint modes are investigated to get information about the structural sensitivity. For the cold LES analyzed in Chapter 4.3.1 a three dimensional visualization of the dominant mode is generated. Three main questions should be answered by this chapter:

1. Is the LSA able to predict the DFT modes when conducted on the LES mean fields?
2. Does the LSA performed on a RANS simulation yield results consistent with their LES counterpart?
3. What main features cause the flow instabilities?

### 4.1 FELiCS tool

All LSA results in this thesis are obtained with the **F**inite **E**lement **L**inear **C**ombustion **S**olver, FELiCS, which is under development at the Laboratory for Flow Instabilities and Dynamics at TU Berlin. FELiCS has been initially developed to take a first step towards an application of LSA on industrial geometries and is therefore based on an unstructured grid which can easily be generated for complex geometries. The construction of the linear operators **A** and **B** (Equations (2.38) and (2.37)) and the solution of the eigenvalue problem from Equation (2.41) is performed using the Finite Element Method (FEM).

Within the FEM approach, the two-dimensional numerical domain is subdivided into  $N$  triangular elements. Following the general assembly process valid for all FEM calculations [40], within each element the solution is sought in the approximate form reading

$$\mathbf{q} = \sum_{i=1}^n \Psi_i \mathbf{a}_i, \quad (4.1)$$

where  $\Psi_i$  are shape functions in the form of polynomials of order  $n$  and  $\mathbf{a}_i$  are unknown coefficients to be solved for. For each element, the linear operators for the unknown coefficients are obtained in an integration step and the global operators  $\mathbf{A}$  and  $\mathbf{B}$  are constructed as a combination of the local operators.

Before a linear stability analysis can be conducted, a mesh has to be generated to define a space where the LSA solver FELiCS operates on. Since the LSA is performed on a contracted 2D-Domain based on the assumption of a homogenous azimuthal direction, the mesh is two dimensional. The LSA solver requires a triangular mesh, which in the framework of this thesis is generated using the open-source software GMSH. To construct this mesh, the interface developed within this thesis takes the PRECISE simulation output and extracts a two-dimensional outline of a streamwise slice of the flow domain. This outline is manually connected by the user, who subsequently defines the inlet and outlet planes as shown in Figure 4.1.

The domain is framed by the wall of the combustion chamber, the inlet, the symmetry axis and the outlet. The outlet is set to the x-coordinate where the combustion chamber transitions to a duct. This duct exists primarily for acoustic measurements and has no influence on the hydrodynamic mechanisms dominant in the inlet area as it has been evaluated within the mesh generation and assessment.

As shown in the lower part of Figure 4.1, the triangular element size is refined in the inlet region where the steepest gradients are located and the majority of dynamics is expected to be. Downstream it is coarsened to reduce computational effort. A mesh study showed no major change in results when the LSA is performed on a mesh exceeding a certain amount of elements and so the analysis within this thesis is performed on a mesh consisting of 20000 elements. The time for a BiGlobal LSA on this mesh performed with a standard workstation is under 20 minutes, illustrating the remarkably low computational cost.

Furthermore, the boundary conditions of the discret domain have to be defined. The numerical strategy within FELiCS assumes the wall to be sufficiently far away from any instability. In the framework of this thesis, the boundary conditions are therefore chosen to be either homogenous Dirichlet ( $q = 0 \forall q \in \Gamma_i$ ) or Neumann ( $\frac{\partial q}{\partial n} = 0 \forall q \in \Gamma_i$ ), where  $\Gamma_i$  denotes the respective boundary. The inlet and outlet BC's are set to Dirichlet for all components whereas the wall BC's are set to Dirichlet for the velocity and to Neumann for the pressure and the density. The boundary conditions for the symmetry axis has to be handled differently for different azimuthal wave numbers. All boundary conditions are shown in Figure 4.1.

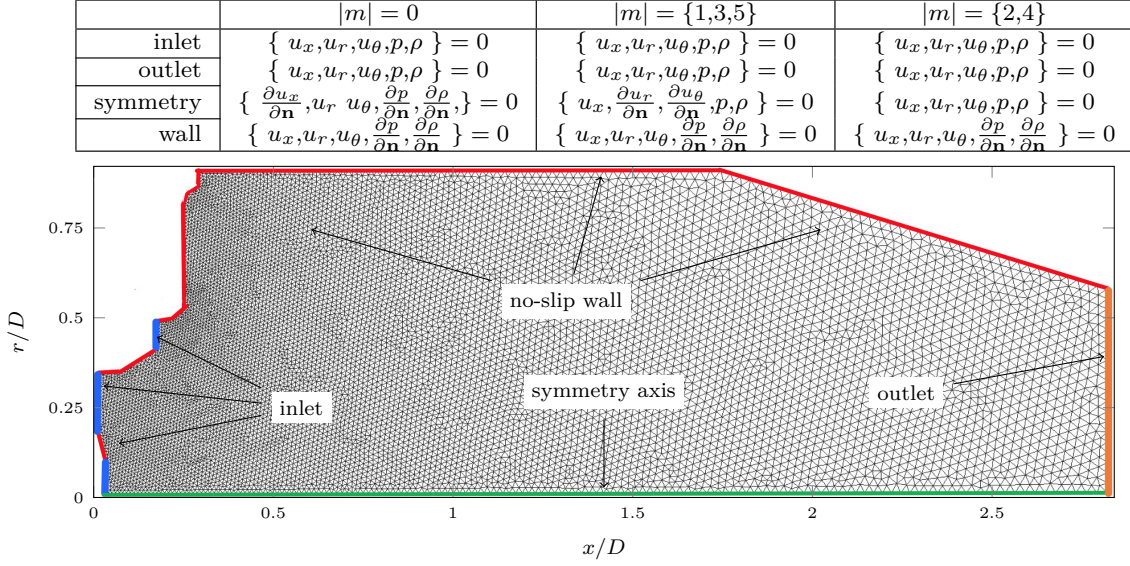


**Figure 4.1:** Numerical domain and boundary conditions for the BiGlobal LSA.

The mesh and the mean field is the only data input FELiCS requires. To conduct an LSA, the user manually defines the boundary conditions based on Figure 4.1 and has to insert a frequency as an initial guess to start the solving of the eigenvalue problem posed within the LSA calculation. The solver then iteratively calculates a user-defined number of eigenvalues. The default number is 100. When finished, the eigenvalue spectrum can be analyzed and the modes corresponding to each eigenvalue can be extracted.

## 4.2 Turbulent viscosity evaluation

In this section the handling of turbulent viscosity is evaluated. Two different approaches are presented: The first is an arbitrary, constant value for the eddy viscosity. This approach is shown to emphasize the need of a turbulent viscosity. The second approach is a turbulent viscosity based on the turbulent kinetic energy and a reference length. The practical implementation of this so called TKE-model is presented. Subsequently, both methods are applied within an LSA of the cold LES for an azimuthal wavenumber  $m = -2$ , to find out if the dominant structure is found. Lastly, the results of the two models are directly compared to each other and to the empirical modes obtained in Chapter 3 to conclude which model is to be used henceforth.

### 4.2.1 $\nu_t$ - constant

First, the LSA is performed by setting the viscosity to the constant kinematic viscosity of the fluid and to that value multiplied by a factor of  $10^2$  and  $10^3$  respectively. This is for one thing done to show the general effect of  $\nu_t$  on the resulting eigenvalue spectrum and primarily to illustrate that in case of a highly turbulent flow, it is invalid to neglect the turbulent viscosity. Figure 4.2a shows the eigenvalue spectrum for an LSA conducted by only taking into account the kinematic viscosity of the fluid. The resulting eigenvalues are randomly scattered around the initially guessed frequency which in this case was  $St = 1.034$ . The close scattering around the initial frequency guess and the lack of any standing out eigenvalues indicates that the eigenvalue problem did not yield any modes corresponding to a physical mechanism. Furthermore, the appearance of numerous eigenvalues with a positive growth rate  $\omega_i^* > 0$  is an indicator for modes that are numerical artifacts. Changing the initially guessed frequency will then result in a spectrum of same appearance but with an eigenvalue distribution closely around the new frequency and without any reappearing eigenvalues.

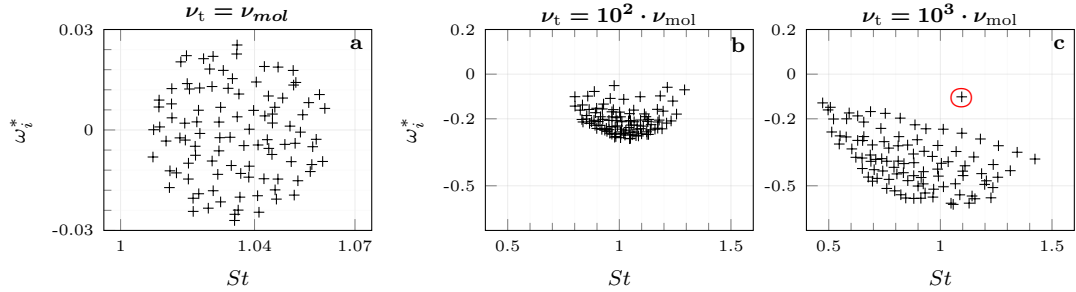


**Figure 4.2:** LSA eigenvalue spectra of the LES cold mean field for different values of  $\nu_t$ . The only physical eigenmode is found for  $\nu_t = 10^3 \cdot \nu_{\text{mol}}$  and is encircled in red.

Increasing the value of  $\nu_t$  by a factor of  $10^2$  results in the spectrum displayed in Figure 4.2b. This spectrum is shifted to negative values of  $\omega_i^*$  and is distributed over a broader frequency range. This indicates that the resulting eigenvalues are not entirely spurious as in 4.2a. However again there are no standing out eigenvalues and the resulting spectrum is strongly depending on the initial frequency guess, making a physical meaning of any of the eigenvalues unlikely. It is with an even larger turbulent viscosity of  $\nu_t = 10^3 \cdot \nu_{\text{mol}}$  that the spectrum shows a distinct eigenvalue which is separated from the remaining bulk of spurious modes. This one particular eigenvalue, circled in red in Figure 4.2c, is not dependent on the initial frequency guess, suggesting a linear modal mechanism inherent to the flow. Its growth rate  $\omega_i^*$  is negative with relative close proximity to zero, which can be expected by an eigenvalue resembling a large scale coherent structure. This structure - in this case the  $m = -2$  helical instability - is not growing or decaying in time, yielding an eigenvalue of almost zero growth rate. The remaining eigenvalues are accumulated in a cloud and can be related to boundary reflections or other spurious solutions to the

eigenvalue problem solved in FELiCS. The associated frequency is  $St = 1.1$  and therefore just 9 % off the frequency of the dominant DFT mode in Chapter 3. An important note here is that the oscillation frequency of the eigenvalue is dependent on the viscosity, even when only changed slightly. Consequently, the constant viscosity model remains ambiguous, since the viscosity value requires guesswork and lack any physical background. Due to its simplicity, the model has its greatest value when first investigating a new flow configuration.

#### 4.2.2 $\nu_t$ - TKE based

A physically backed approach for the turbulent viscosity is the TKE-model, which bases the viscosity calculation on the turbulent kinetic energy and a characteristic length scale (see derivation in Chapter 2.2). To calculate the length scale, the TKE-model requires an *a priori* knowledge of the type and scale of coherent structures. With the information obtained by means of POD and DFT in Chapter 3, the approximate extent of the largest structures is calculated as the distance between the local extrema of axial velocity enclosing the shear layer of interest. This distance is visualized as red lines in Figure 4.3a.

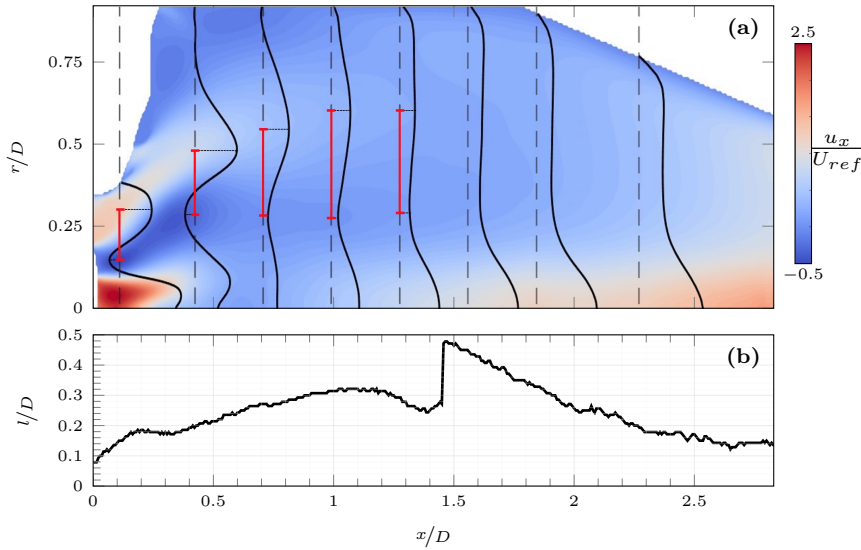


**Figure 4.3:** (a): Mean field with black lines indicating the x-velocity at the respective axial position marked by the vertical dashed black lines. Red lines mark the distance between the local x-velocity extrema at the particular axial position. (b): Radial distance  $l$  between local extrema as a measure for the turbulent length scale.

Calculating the length scale with this method results in an increasing value until  $x = 1.2D$  as pictured in Figure 4.3b. This is a reasonable development for a widening vortex originating at the inlet. However, at about  $x = 1.5D$  the calculation runs into an error

because the two extrema vanish, imposing a discontinuity on the length scale. This discontinuity does not make physical sense, leaving the second half ( $x > 1.5D$ ) of the domain up for discussion. However, the inlet area shows a reasonable evolution of turbulent length scale and since the majority of coherent dynamic is happening in the first half of the domain, the calculation is applicable. The separate treatment of the second half is necessary due to the error in length scale. To compensate for the incontinuous viscosity at  $x = 1.5D$ , a so called sponge layer is added to the second half of the domain. This layer adds a gradually increasing viscosity  $\nu_{sp}$  to the calculated viscosity. An additional benefit of this layer is its dampening function for perturbations emanating from the truncated outlet. As shown by Lesshaft [41], a truncated domain can lead to unwanted perturbation feedback which leads to unphysical modes.

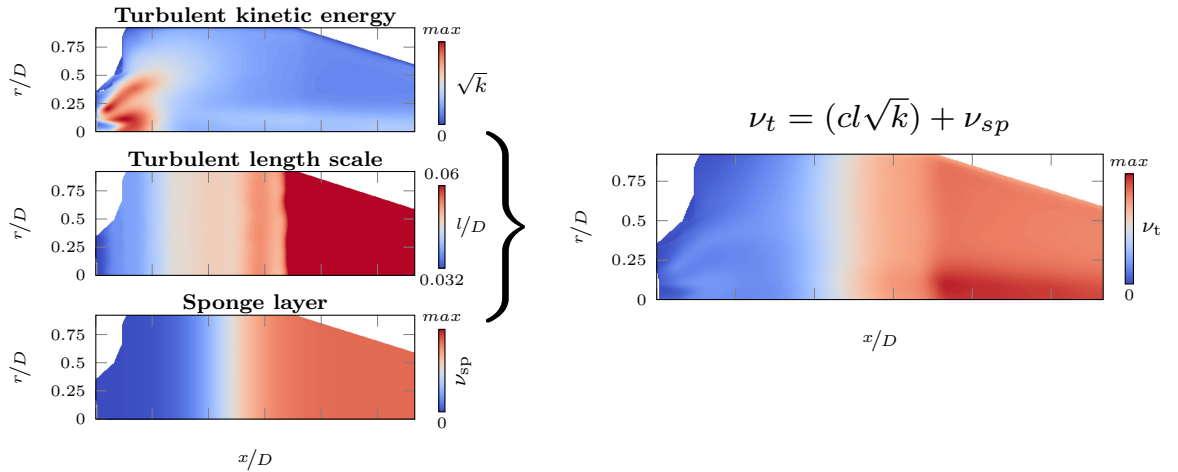


**Figure 4.4:** Left side: Spacial distribution of turbulent kinetic energy  $k$ , turbulent length scale  $l_m$  and sponge viscosity  $\nu_{sp}$ . Right Side: The complete viscosity field as an addition of  $\nu_{sp}$  and the turbulent viscosity calculated by  $\nu_t = cl_m\sqrt{k}$

Figure 4.4 shows the resulting turbulent viscosity field. It can be visualized as an addition of the turbulent viscosity obtained by  $\nu_t = cl_m\sqrt{k}$  and the sponge layer. To evaluate the influence of the sponge viscosity, an LSA was conducted with and without the sponge layer. The results showed that the separated eigenvalue was not affected by the sponge layer, while the spurious modes got damped strongly (see Appendix Figure 5.6). This shows that the sponge layer has no influence on the physical modes. Following the derivation in Chapter 2.2, the turbulent viscosity is finally calculated by  $\nu_t = 0.55 \cdot \sqrt{k} \cdot l_m$  and the effective viscosity is defined as  $\nu_{eff} = \nu_{mol} + \nu_{SGS} + \nu_t + \nu_{sp}$  where, as a reminder,  $\nu_{SGS}$  is the sub-grid-scale viscosity extracted from the LES simulation.

### Comparison of the two models

Shown in the left half of Figure 4.5 are the eigenvalue spectra of the LSA as obtained with the TKE-model and the constant viscosity model respectively. Both models yield a spectrum with one weakly damped separated eigenvalue associated to a global mode. The separated eigenvalue obtained with the TKE model is located at  $\omega_i^* = -0.22$  and the separated eigenvalue obtained with a constant viscosity is located at  $\omega_i^* = -0.1$ . Both eigenvalues are in relative proximity to a zero growth rate, which supports their physical background as a global mode oscillating at its limit cycle. The eigenvalue separation is more significant in the TKE spectrum, with the remaining eigenvalues strongly shifted to lower frequencies. Under the assumption that the remaining eigenvalues are of unphysical nature with boundary reflections as their origin, this can be explained with the TKE-viscosity gradually increasing in the downstream half of the domain and therefore damping the eigenvalues that arise due to outlet reflections. The TKE-model exactly matches the oscillation frequency of  $St = 1$  which has also been identified for the dominant mode by means of DFT (see Figure 3.5). Certainly, this comes with two proportionality constants  $C_\mu$  and  $c_{\text{prop}}$  involved in the TKE viscosity calculation (see Chapter 2.2). However, this is an accurate result and underlines the applicability of the TKE-model.

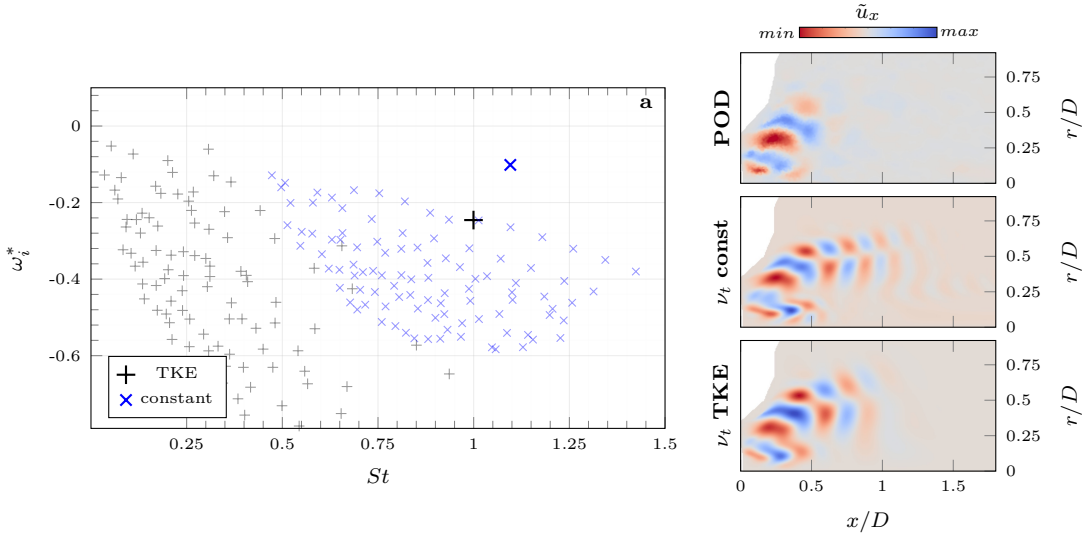


**Figure 4.5:** Left side: LSA eigenvalue spectra for an azimuthal wavenumber of  $m = -2$  obtained with a constant viscosity and with a viscosity calculated with the TKE-model. Right Side: Coherent velocity field corresponding to the respective separated eigenvalues in comparison with the spacial shape of the dominant POD mode. Contour colours are normalized with the maximal value of each field.

Depicted in the right half of Figure 4.5 are the axial velocity fields of the leading mode obtained by means of POD and the axial velocity fields corresponding to the separated eigenvalue of both models. Both models predict the spacial shape of the unsteady

mechanism with good accuracy. However, when compared in detail, the TKE-model seem to match the POD mode shape with better precision. Especially the region of the inlet axis jet is better matched in the TKE model. Conclusively, the TKE-model is chosen for all following LSA investigations.

### 4.3 Results

In the following, the results of the LSA conducted on all four flow fields - cold flow LES, cold flow RANS, reacting LES and reacting RANS are presented. For every configuration the LSA is conducted for azimuthal wave numbers of  $m = \{-1, -2, -3, -4, -5\}$  in order to evaluate the LSA's ability to find all instabilities found by means of POD and DFT in Chapter 3. Within their respective section, the LSA results are directly compared to the discrete Fourier modes from Figure 3.6.

#### 4.3.1 LES cold flow

Figure 4.6 shows the LSA eigenvalue spectra for the cold flow LES for azimuthal wavenumbers  $m = \{-1, -2, -3, -4, -5\}$ . The red lines feature the oscillation frequency of DFT modes for the respective wave number. For each wave number, there is one single separated eigenvalue that stands out from the remaining randomly scattered eigenvalues. All of these separated eigenvalues have a negative growth rate in relative close vicinity to  $\omega_i^* = 0$  which again suggest a mode oscillating without a temporal change in amplitude as expected for a mode at its limit cycle. Closest to a zero growth rate is the  $m = -2$  eigenvalue and from there on to higher and lower azimuthal wave numbers, the growth rate of the leading eigenvalues decreases. The decrease in growth rate from the  $m = -2$  to the  $m = -5$  eigenvalue follows a linear trajectory. This is in good agreement with the DFT spectrum in Figure 3.5, which identified the most dominant mechanism at  $St = 1$  and additional weaker dynamics at  $St = \{0.5, 1.5, 2, 2.5\}$ . For azimuthal wavenumbers  $m = \{-2, -3, -4, -5\}$ , the frequencies associated to the eigenvalues are very close to the DFT frequencies, with a maximal deviation of 2.5%. The frequency of the  $m = -1$  eigenvalue is not matched and is 45% larger than the frequency of the corresponding DFT peak.

The lower half of Figure 4.6 shows the spacial mode shapes corresponding to each separated eigenvalue in direct comparison with the associated Fourier mode shape. The inlet region until about  $x = 0.5D$  is matched accurately for all azimuthal wave numbers besides  $m = -1$ . In contrast to the modes of higher azimuthal wave number, the  $m = -1$  mode is sensitive to viscosity changes in the downstream domain. One reason for this is its lower frequency resulting in a larger wavelength reaching further downstream. The  $m = -1$  LSA mode has a significant amplitude close to the axis, which is not seen in the other modes. In the downstream field for  $x > 0.5D$ , the LSA predicts an oscillating pattern where the Fourier mode amplitude already vanishes. For a deactivated sponge layer, this oscillation pattern reaches to the outlet, which suggests a reflection mechanism. Since

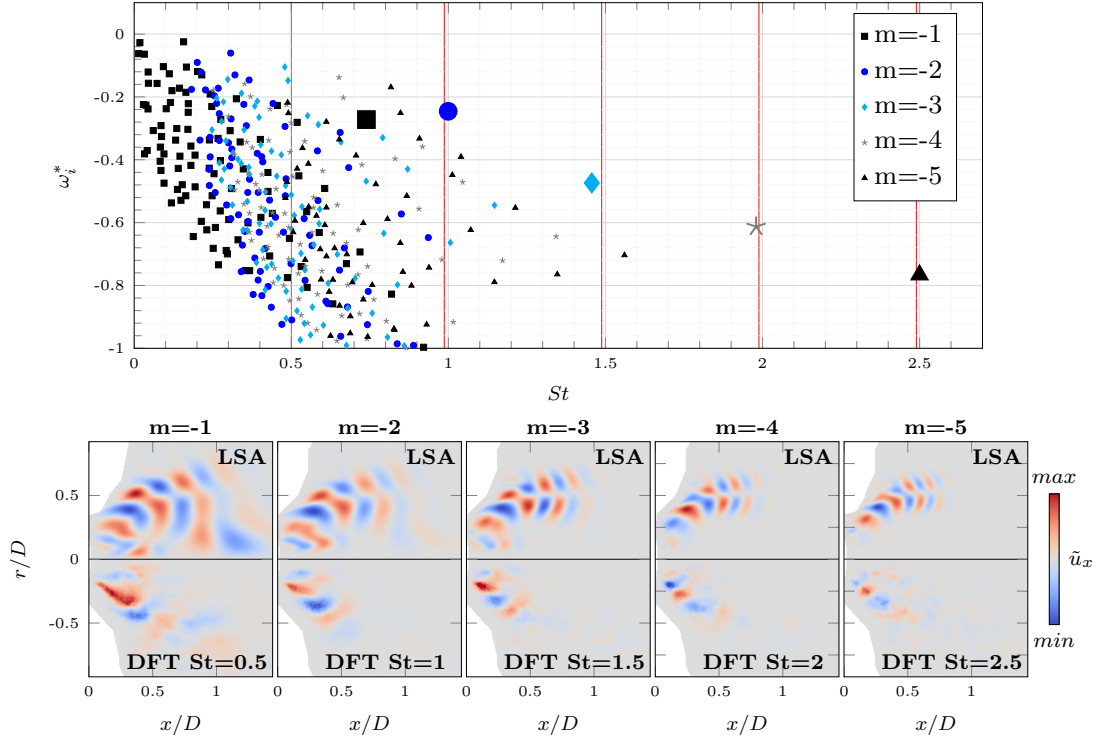


**Figure 4.6:** Cold flow LSA Eigenvalue spectra of different azimuthal wavenumbers  $m = \{-1, -2, -3, -4, -5\}$  plotted together. The red lines mark the oscillation frequency of the five modes identified by means of DFT. The separated eigenvalue corresponding to the global mode of each wave number is enlarged and depicted in the legend. The lower half shows the mode shape corresponding to each separated eigenvalue at the respective azimuthal wave number in comparison with the DFT modes at the frequencies marked by the red line.

its presence has no influence on the frequency and growth rate, it is not associated to a physical mechanism. A possible reason for its appearance is the turbulent viscosity calculated in Chapter 4.2.2, which does not include the Reynolds shear stresses, leading to an underestimation of the turbulent viscosity.

Nevertheless, the LSA finds the main features of the flow with good accuracy. One helical global mode with an azimuthal wave number of  $m = -2$  and a frequency of  $St = 1$  is identified as the dominant mechanism. Weaker global modes at azimuthal wave numbers of  $m = \{-3, -4, -5\}$  with respective frequencies of  $St = \{1.5, 2, 2.5\}$  are found. Those three modes are in agreement with the empirical modes obtained in Chapter 3. The instability mechanism at  $St = 0.5$  that was identified by means of DFT (Figure 3.5) could not be recovered with the same accuracy but also appears in the eigenvalue spectrum. The fact that the LSA finds each DFT mode suggest an individual linear mechanism for all modes.

### Adjoint modes

The next step is to take a look at the adjoint modes obtained within the LSA. Each direct global mode in Figure 4.6 has a corresponding adjoint mode. These adjoint modes can be described as a measurement of receptibility of a global mode to flow control and therefore are of great interest in the context of an LSA application in design processes.

Figure 4.7 shows the adjoint mode corresponding to the global  $m = -2$  mode from Figure 4.6. It shows a high receptibility in a region downstream of the splitter plate between the pilot jet and the middle inlet passage. The axial and radial components have their highest amplitude in the shear layer between the middle passage and the recirculation zone, whereas the azimuthal component has its highest amplitude in the inner region between pilot jet and recirculation zone.

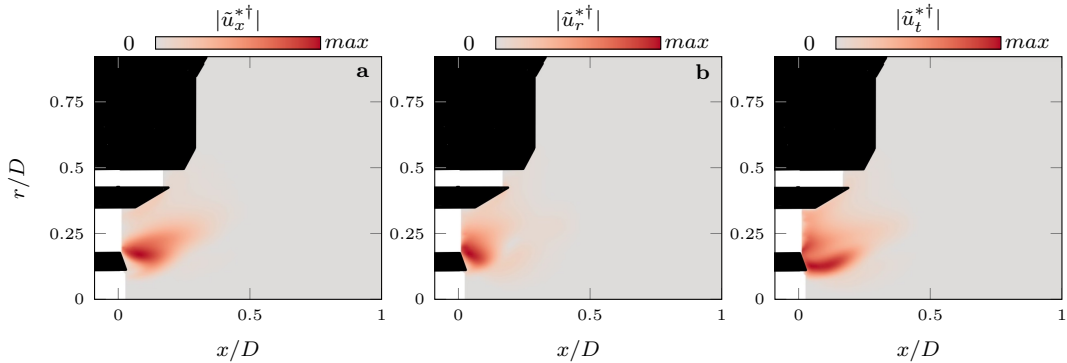


**Figure 4.7:** Axial, radial and azimuthal velocity component of the adjoint mode corresponding to the direct mode for  $m = -2$ .

A comparison between direct modes in Figure 4.6 and adjoint modes in Figure 4.7 shows a spatial separation between the regions of highest amplitude. This spatial separation of direct and adjoint mode was also observed for a cylinder wake flow by Giannetti et al. [34] who concluded that, in order to identify the origin of a global mode, it is not sufficient to focus solely on either the direct or adjoint modes. They proposed a structural sensitivity analysis, in which the direct and adjoint modes are coupled to yield information about where the strongest feedback region is located.

The upper part of Figure 4.8 shows this structural sensitivity for each of the identified global modes from Figure 4.6. The lower part shows the mean field with the regions of highest structural sensitivity highlighted in dark red. The highest magnitude of structural sensitivity is located upstream of the recirculation zone, close to the splitter plate between innermost and middle passage. Similar to the adjoint modes in Figure 4.7, there are two regions which now can be identified as the origin of the global modes. One region is

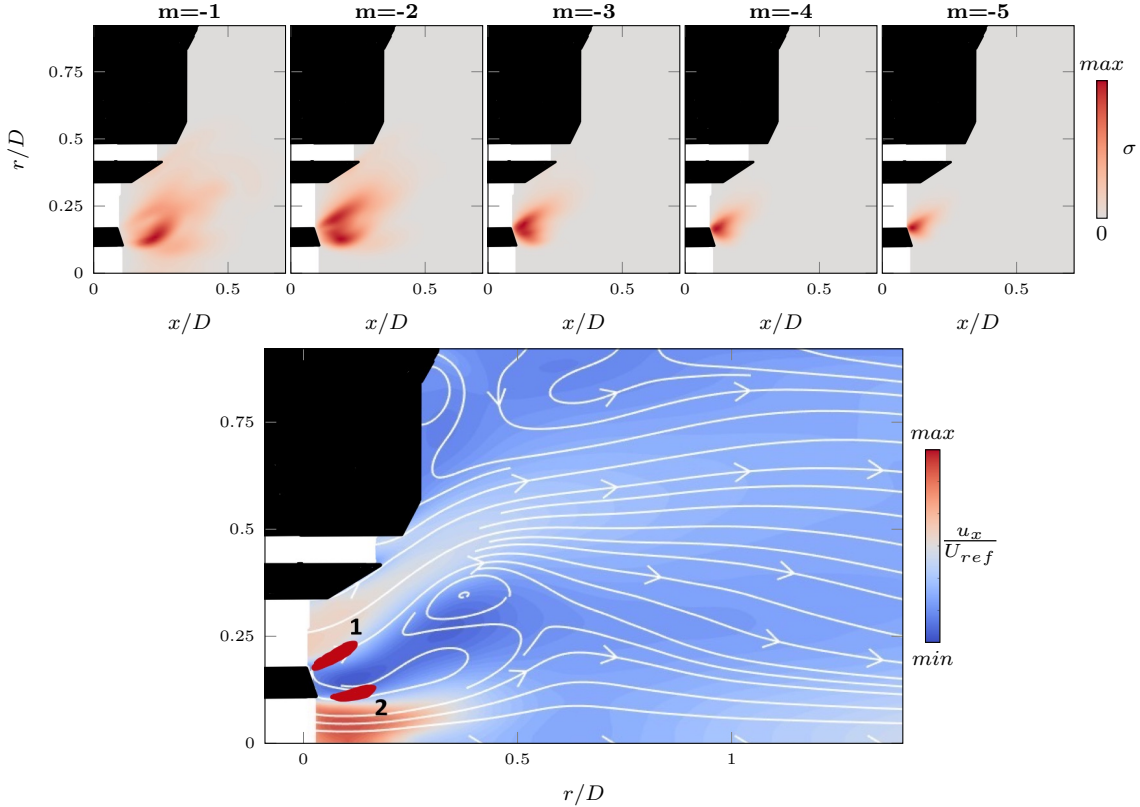


**Figure 4.8:** **a:** Structural sensitivity of each global modes from Figure 4.6. **b:** Mean velocity field with streamlines in x-r-plane and a clearly shaped recirculation bubble. The dark red mark indicates the location of highest structural sensitivity and therefore the wavemaker of the global modes.

located in the shear layer between the pilot jet and the recirculation zone (numbered as 2) and the other region is located in the shear layer between the middle passage and the recirculation zone (numbered as 1). Mode  $m = -1$  has its highest sensitivity in region 2 whereas the dominant mode  $m = -2$  has high sensitivity in both regions. The modes with higher azimuthal wave number mainly originate in region 1. The assumption that mode  $m = -1$  has a different region of origin was assumed earlier on in this chapter and is now supported by the adjoint analysis. In fact, in all subsequently presented LSA, mode  $m = -1$  is either not found (reactive LES in Figure 4.10) or appears to have a different origin.

Conclusively, the highest structural sensitivity for all modes is located in the shear layers adjacent to the upstream section of the recirculation zone. These are regions of absolute instability, so called wavemakers, which induce the global instabilities to the whole flow

domain. If a suppression or control is required by design or active forcing, it is most efficient in those regions. The identified location in an upstream section of the recirculation zone is in accordance with preceding investigations of swirled flows [27] [9] and, as Kaiser [27] stated, appears to be generally valid in swirled combustor flows.

### Three dimensional mode shape

As stated in Chapter 3.2 and now reinforced by the LSA results in the preceding section, the dominant instability mechanism takes shape as an  $m = -2$  helical structure, which emanates at the inlet and travels downstream counter-winding relative to the mean field. In Figure 3.4, the three dimensional instantaneous data was investigated for such structures by means of the Q-criterion. This analysis found a two-armed helix in the inlet area, which can be associated to the dominant  $m = -2$  instability inherent to the flow. To compare the empirical analysis from Chapter 3.2 with the linear results in this chapter, the two dimensional field of the dominant  $m = -2$  mode has been processed to depict the three dimensional evolution the global mode. Figure 4.9 shows the azimuthal vorticity calculated from the direct mode in a blue isocontour.

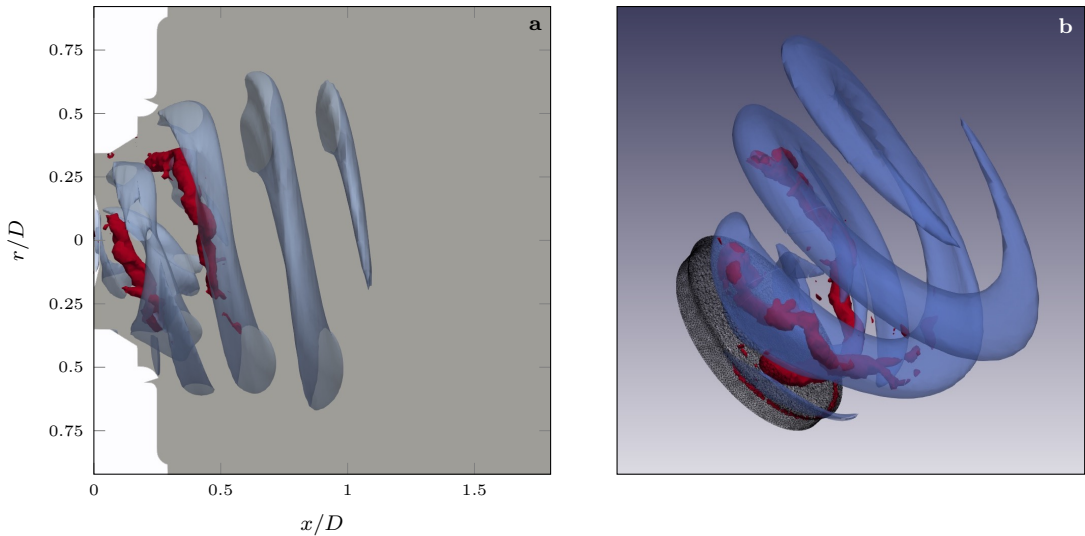


**Figure 4.9:** Azimuthal vorticity of dominant mode (blue isocontour) overlayed with the instantaneous vorticity from the 3D-field calculated with the Q-criterion.

Originating between inner and middle passage it follows the helix of high vorticity extracted from the original three dimensional snapshot (red isocontour, see Figure 3.4). In this visualization, the mean field streamlines from Figure 3.4 are omitted but the reader has to be reminded, that the mode is counter-winding relative to the mean field. The 3D field by itself gives no new information about the evolution of the instability, however it can help to understand the underlying dynamics. The 3D-analysis underlines the findings of this section and allows the conclusion that the hydrodynamic instability of the cold flow LES

has been found by the BiGlobal LSA.

### 4.3.2 LES reacting flow

Subsequent to the cold LES, a BiGlobal LSA has been conducted on a reacting LES. The reader is reminded that the reacting LSA is based on an additional governing equation which incorporates the non-homogenous density field (see Chapter 2.2). This approach includes a low mach assumption and is therefore referred to as low mach LSA. The resulting eigenvalue spectra for the reacting LES are depicted in Figure 4.10 in the same manner as it was done for the cold flow in Figure 4.6.

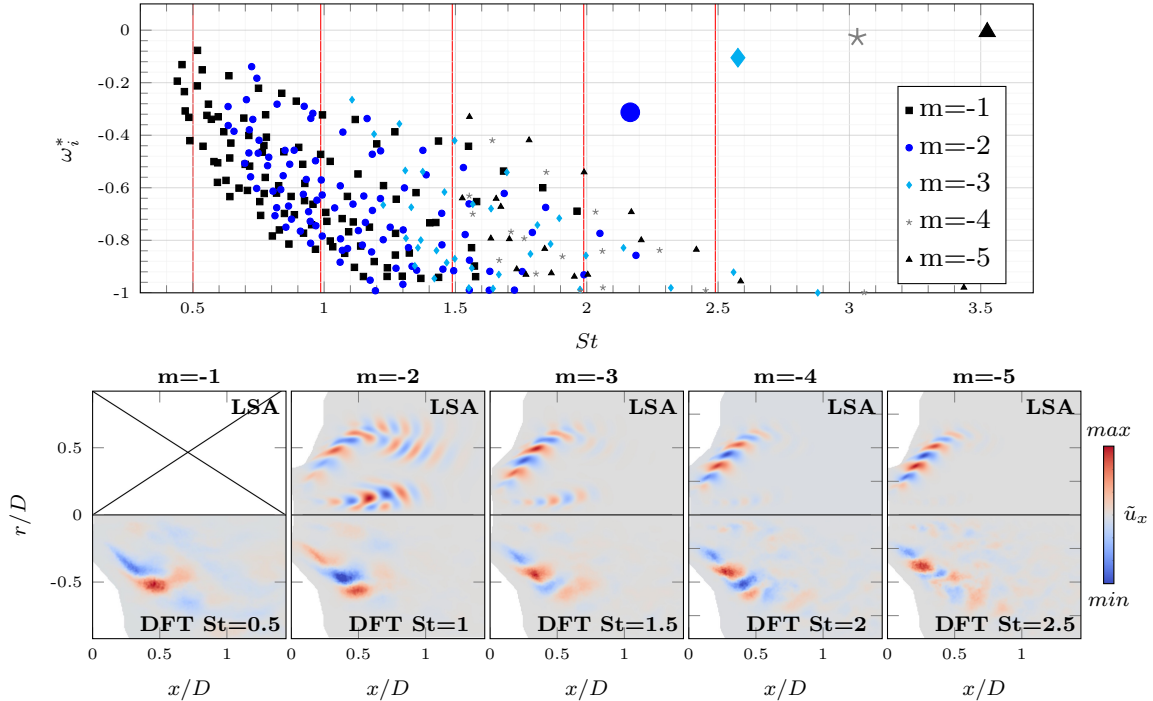


**Figure 4.10:** LSA eigenvalue spectra and spacial shapes of separated eigenvalues at different azimuthal wavenumbers  $m = \{-1, -2, -3, -4, -5\}$  as obtained for the reacting LES using the equations for a non-homogenous density. The layout is similar to Figure 4.6.

In all but the  $m = -1$  spectrum one single separated eigenvalue corresponding to a global mode is found. These separated eigenvalues are at negative growth rates and converge to  $\omega_i^* = 0$  with increasing azimuthal wave number. In contrary to the cold flow LSA, which yielded results in agreement with the DFT modes from Figure 3.5, here the DFT mode frequencies are not matched. However, consistent with the cold flow LSA from the preceding section, the eigenvalue frequency is a function of azimuthal wave number, leading to a similar arrangement relative to each other as it was seen for the cold flow in Figure 4.6. The growth rates of the eigenvalues are not in agreement with the results

from Chapter 3.2. As mentioned there, the dominant hydrodynamic instability in both cold and reacting flow manifests as a two-armed ( $m = -2$ ) helical structure which was extracted by means of Q-criterion (see Figure 3.4). The reacting LES eigenvalue spectrum however indicates the strongest global mode at an azimuthal wave number of  $m = -5$  and the weakest global mode at an azimuthal wave number of  $m = -2$ . The expected  $m = -1$  mode is not found within the reactive LSA.

Depicted in the lower part of Figure 4.10 are the spacial modes corresponding to the separated eigenvalues at the respective azimuthal wave number in comparison with the associated DFT mode. Consequently, no velocity field is shown for  $m = 1$ . Due to the large differences in frequency, the DFT and LSA mode shapes differ significantly. Nevertheless, the general regions of high amplitude are similar, with a main branch being located adjacent to the inner shear layer between the middle passage and the recirculation zone and the secondary branch emanating in the shear layer between axis jet and recirculation zone. Apparently, the low mach LSA is capable of finding the instability mechanisms inherent to the flow, however with a significant frequency deviation.

A possible reason for this strong deviation might be the viscosity modeling, which, as shown in its derivation in Chapter 2.2, does not include the Reynolds shear stresses. Furthermore, it has to be noted, that the governing equations do not include the reaction chemistry of the liquid fuelled combustion. Therefore, only the mean flames influence on the density field is considered, neglecting any coupling mechanisms between hydrodynamic instabilities and combustion process. In addition to that, the influence of the liquid spray on the density field is not taken into account. An extension to the governing equations that takes into account those effects is not implemented yet and requires further research.

Although the low mach LSA results presented in Figure 4.10 lack accuracy in predicting the frequencies and relative growth rates of the empirical modes, they can still be considered correct in the sense that the global modes for  $m = \{-2, -3, -4, -5\}$  are identified. Therefore, in order to get information on the mechanism responsible for the large scale oscillation, an investigation of the structural sensitivity is conducted and the results are shown in Figure 4.11.

Depicted in the upper half is the magnitude of structural sensitivity for each global mode from Figure 4.10. The region of highest internal feedback is located between the innermost and the middle inlet passage in the upstream region of the recirculation zone. In contrast to the cold flow LSA, the inner shear layer between pilot jet and recirculation zone appears to be not involved in the emergence of global modes. The lower half of Figure 4.11 shows the mean flow and isocontour lines of the highest mean heat release which correspond to the location of the flame. The red mark indicates the wavemaker position identified within the structural sensitivity analysis. As mentioned in the cold flow investigation (see Chapter 4.3.1), the wavemaker location in the upstream section of the recirculation zone is in agreement with preceding studies on combustor flows. Furthermore, the spacial separation of wavemaker and flame is a possible reason for the similarities of the DFT modes of cold and reacting flow (see Figure 3.5 and 3.6). The large scale coherent structure originates in a region upstream of the flame, which prevents the flame to have a major

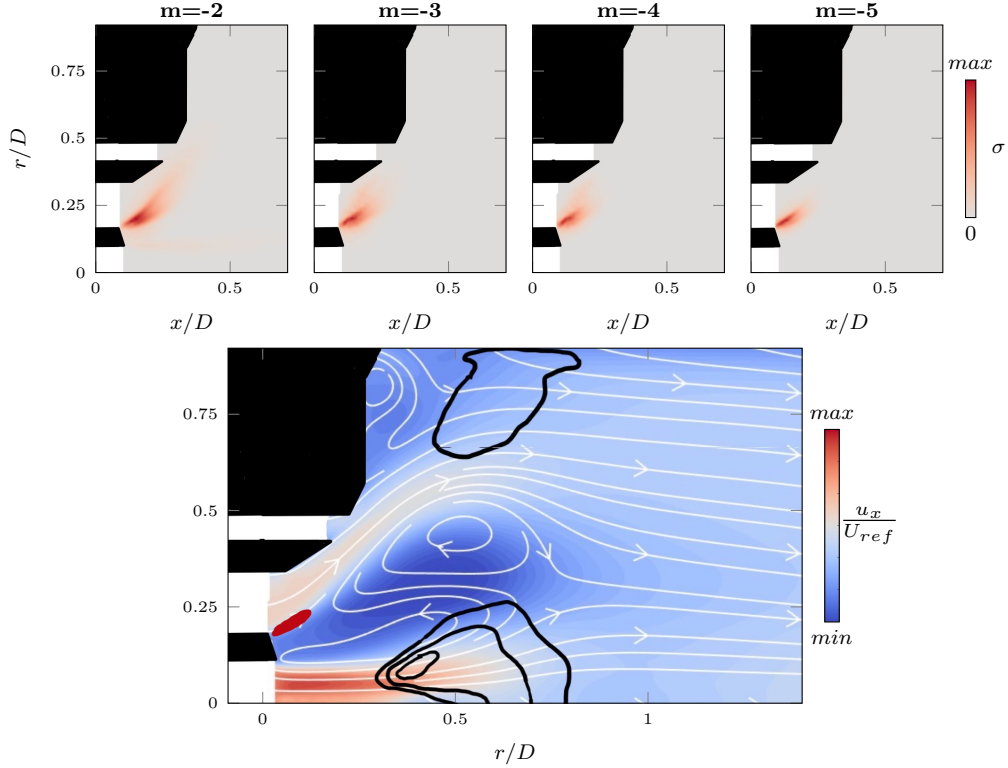


**Figure 4.11:** **a:** Structural sensitivity of the five global modes of the reacting LES as obtained with low mach LSA. **b:** Axial component of the mean velocity field with streamlines in x-r-plane and a clearly visible recirculation bubble. The red mark indicates the wave-maker position and the black lines are isocontours of the mean heat release indicating the flame position.

influence on the hydrodynamic instability.

#### LSA on reacting flow with homogenous density assumption

Another possibility to investigate the reacting flow configuration is to neglect the non-uniform density field and conduct an LSA with only the continuity and momentum equation as it is done for the cold flow configuration. The results of this 'cold hot' analysis are shown in Figure 4.12.

Here, a single separated eigenvalue is found for all investigated azimuthal wave numbers. The eigenvalue corresponding to an azimuthal wave number of  $m = -3$  has the largest growth rate with  $\omega_i^* = -0.2$ . Similar to the low mach LSA depicted in Figure 4.10, the eigenvalues are shifted to higher frequencies compared to the DFT modes marked by the red lines. However, the frequency again is a function of azimuthal wave number similar to

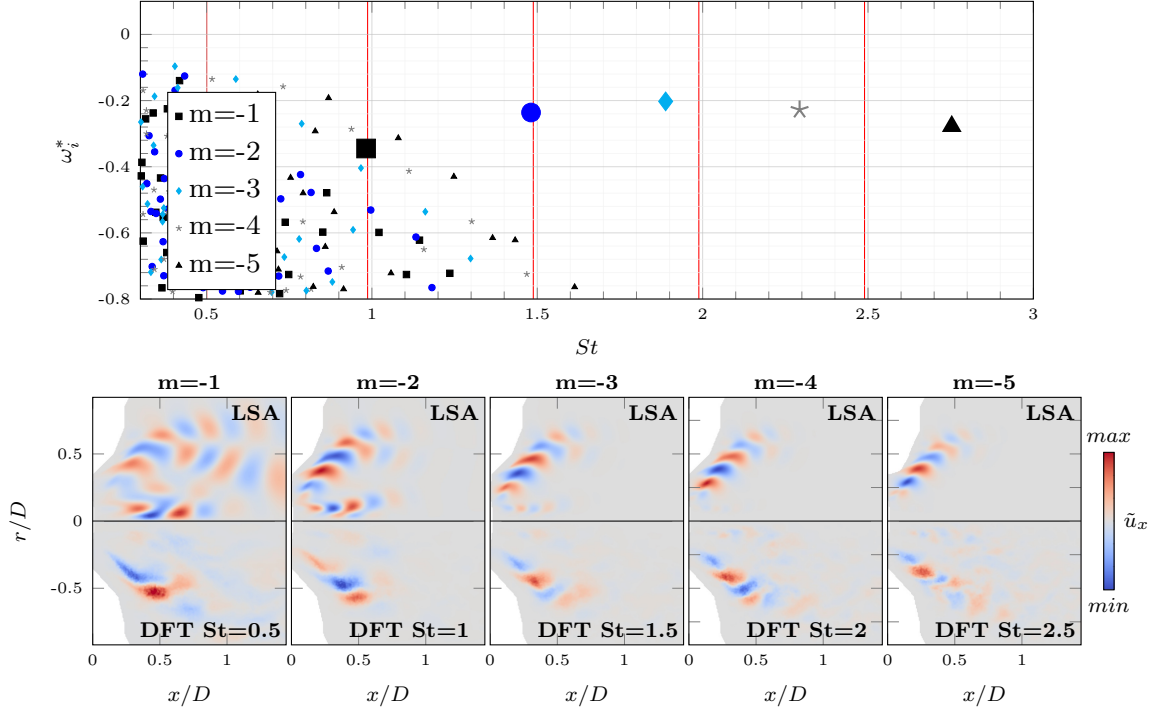


**Figure 4.12:** LSA eigenvalue spectra and spacial shapes of separated eigenvalues at different azimuthal wavenumbers  $m = \{-1, -2, -3, -4, -5\}$  as obtained for the reacting LES calculated with the equations for a uniform density. The layout is similar to Figure 4.6.

the low mach LSA and the cold flow LSA in Figure 4.6.

The spacial mode shapes in Figure 4.12 are consistent with the DFT modes and the low mach LSA modes and show the global modes highest amplitudes in the shear layers of pilot jet and middle passage. Mode  $m = -1$  has its highest amplitude close to the symmetry axis, indicating a different mechanism active, similar to the cold flow in Figure 4.6. Since the LSA mode frequencies are shifted to higher values, also the wavepackets are denser compared to the DFT modes. Generally, the 'cold hot' LSA generates a more accurate depiction of the Fourier modes than seen in the low mach LSA in Figure 4.10. Nevertheless, while these results appear closer to the empirical modes, they have to be treated with caution, since they are based on the assumption of a homogenous density field when in fact a significant density drop is present due to the flame.

The structural sensitivity of each global mode is shown in Figure 4.13. The locations of highest structural sensitivity as identified by the 'cold hot' LSA are in agreement with the locations identified for the low mach approach in Figure 4.11. For the global modes with azimuthal wave numbers  $m = \{-2, -3, -4, -5\}$ , the highest sensitivity is located in a narrow region in the shear layer between the middle inlet passage and the recirculation

zone. The inner shear layer appears to have no influence in the origin of those modes. The sensitivity of mode  $m = -1$  reveals a more distributed field without a narrow local maximum. The highest sensitivity is located in the outer shear layer in relative large distance to the splitter plate. The inner shear layer also appears to be included in the mode dynamics. This supports the assumption of a different mechanism being active for the  $m = -1$  mode.

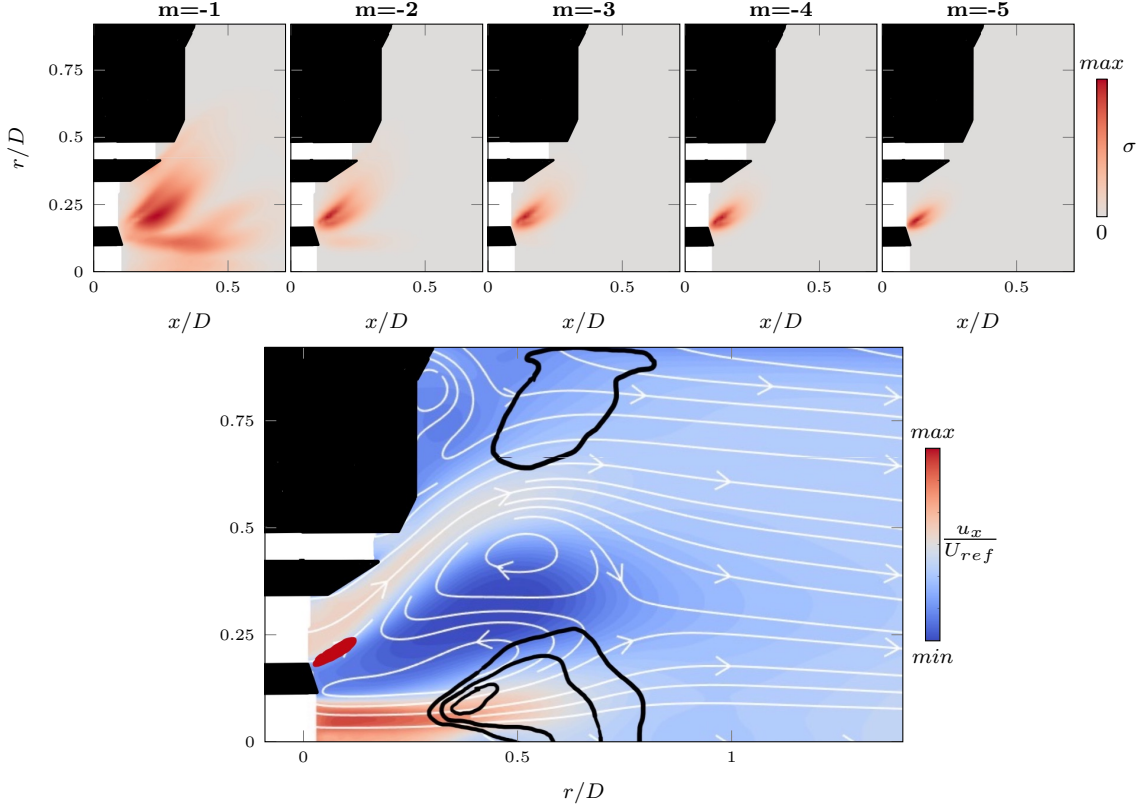


**Figure 4.13:** **a:** Structural sensitivity of the five global modes of the reacting LES as obtained with cold flow LSA. **b:** Axial component of the mean velocity field with streamlines in x-r-plane and a clearly visible recirculation bubble. The red mark indicates the wave-maker position and the black lines are isocontours of the mean heat release indicating the flame position.

The results show that for the reactive configuration, the LSA based on a homogenous density field performs better than the LSA which takes into account the non-homogenous density field with a third equation. This is in contrast to preceding investigations on a reactive swirled combustor flow [27] and on a reactive turbulent jet [33]. In both cases, the low mach LSA yielded more accurate results. However, neither low mach nor 'cold hot' LSA predicts the dynamics of the reactive flow as accurate as the LSA for the cold LES was able to do in Chapter 4.3.1.

### 4.3.3 RANS cold flow

Subsequent to the LES mean field, the LSA was conducted on a cold flow RANS simulation. As depicted in Figure 3.1, the RANS flow field differs from the cold flow LES mean field. Most importantly, due to the larger penetration depth of the inlet passages, the shear layers enclosing the recirculation zone are larger in the RANS simulation. This is expected to influence the LSA. The LSA results for the azimuthal wave numbers  $m = \{-1, -2, -3, -4, -5\}$  are shown in Figure 4.14.

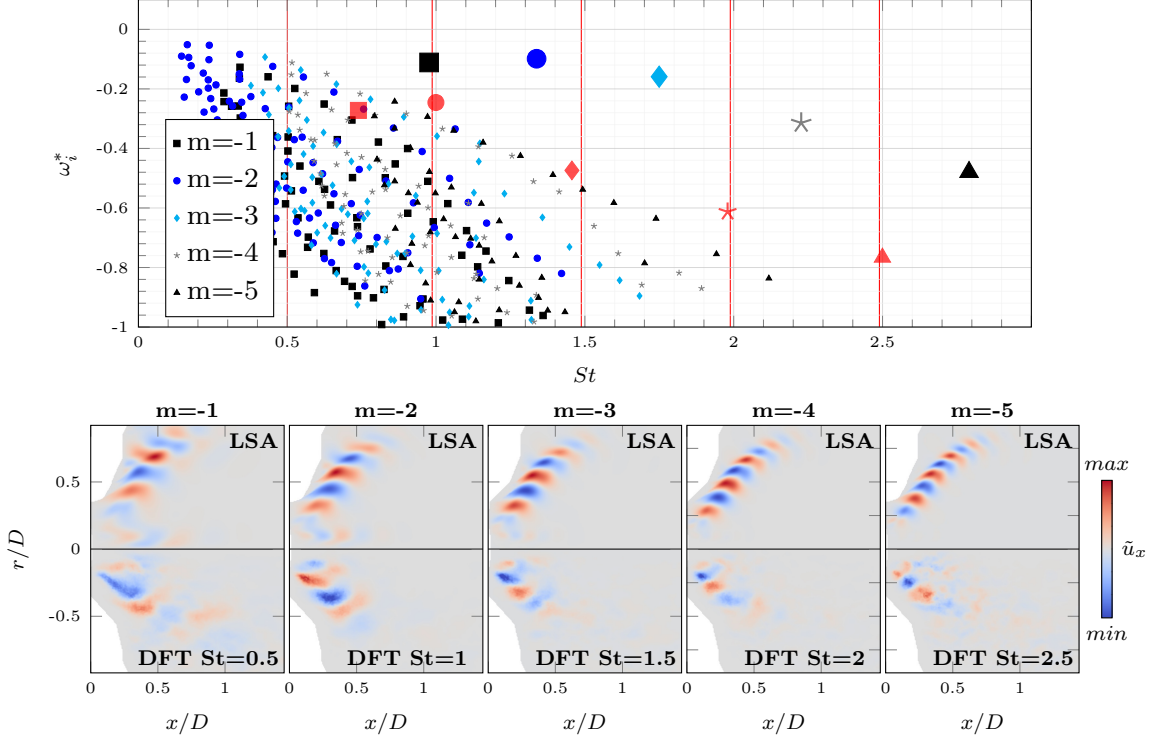


**Figure 4.14:** Eigenvalue spectra and spacial shapes of separated eigenvalue at different azimuthal wavenumbers  $m = \{-1, -2, -3, -4, -5\}$  as obtained for the cold flow RANS. The layout is similar to Figure 4.6. The five separated eigenvalues from the cold flow LES are depicted in red.

The eigenvalue spectra for each azimuthal wave number all yield one single separated eigenvalue that can be related to a global mode. All of those eigenvalues are negative and have a similar arrangement to each other as the eigenvalues extracted from the cold flow LES, which are depicted in red. However, while the eigenvalue frequency is a function of wave number similar to the cold flow LES results, all frequencies are shifted to larger values. The relative frequency difference between the eigenvalues is comparable to the cold flow LES results. The  $m = -2$  eigenvalue is closest to a zero growth rate and the growth rate of the other eigenvalues follows a gradually decreasing trajectory. This indicates a

dominant hydrodynamic instability at an azimuthal wave number of  $m = -2$  which is in agreement to the empirical and linear analysis of the cold flow LES conducted in Chapter 3.2 and 4.3.1 respectively.

A quantitative comparison of the cold LES and cold RANS eigenvalues shows that the RANS eigenvalues are located closer to a zero growth rate. An explanation for this is the fact that the LES mean field is already modulated by the large-scale coherent structure. The RANS field however does not include any unsteady motion. While the RANS viscosity model is generally able to account for fine scale turbulent motion, it fails to describe the large-scale turbulent motion. Therefore, the RANS flow field is closer to a base flow than a mean flow and the identified global modes are more unstable than their mean flow equivalent [4].

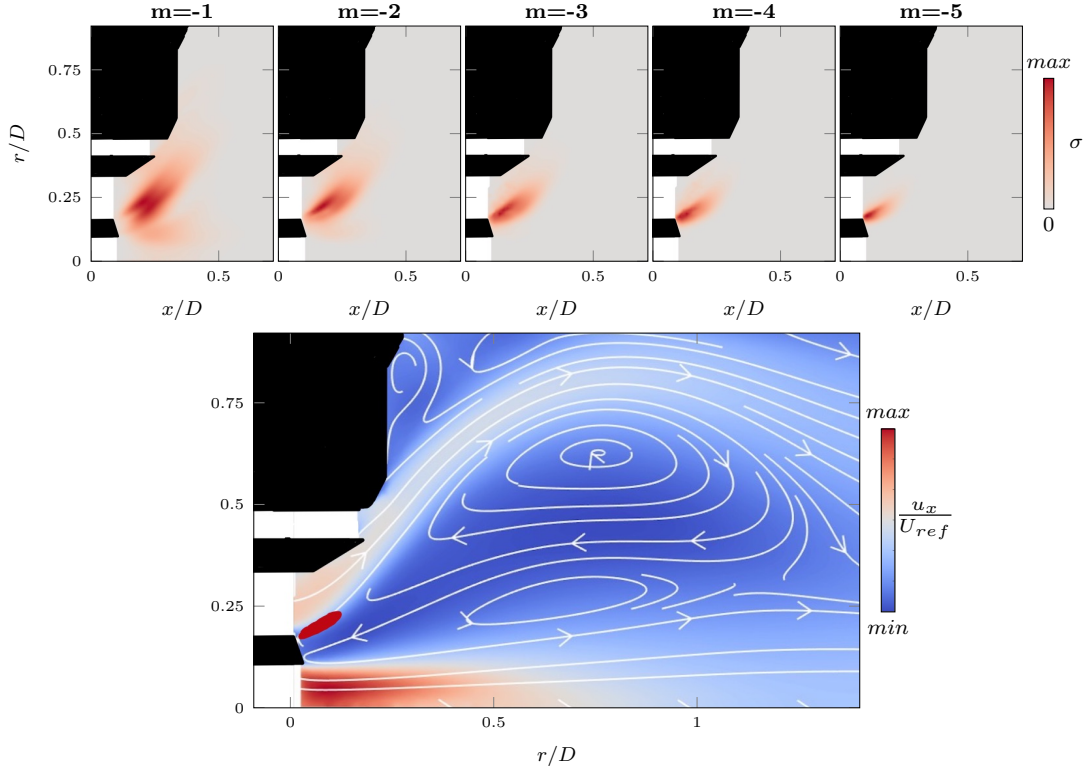


**Figure 4.15:** a: Structural sensitivity of the five global modes of the cold flow RANS. b: Axial component of mean velocity field with streamlines in x-r-plane and a clearly shaped recirculation bubble. The red mark indicates the wavemaker position.

The spatial mode shapes corresponding to the five LSA eigenvalues are shown in the lower half of Figure 4.14. The region of highest amplitudes for the direct modes is identified in the two shear layers enclosing the recirculation zone, with the outer shear layer containing the majority of coherent fluctuations. Especially the region directly after the inlet passages is in good agreement with the Fourier modes. However, the LSA modes are elongated and

in all cases reach the cylindrical combustor wall at  $r = 0.9D$  whereas the Fourier modes decay around  $r = 0.5D$ . This deviation is not attributable to the LSA calculation itself but to the RANS calculation, which predicts the penetration length of the inlet passages inaccurately.

The structural sensitivity of each mode is shown in Figure 4.15. It becomes evident that the strongest feedback of the global RANS modes is located in the outer shear layer between the recirculation zone and middle inlet passage. This is different to the cold flow LES in Figure 4.8, where mode  $m = -1$  had its highest sensitivity in the inner shear layer and the  $m = -2$  mode had a high sensitivity in both inner and outer shear layer.

#### 4.3.4 RANS reacting flow

Lastly, the LSA results for the reacting RANS simulation are presented. Similar to the reacting LES in Chapter 4.3.2, the LSA is performed two times. Once with the full set of equations for a non-homogenous density and once with the continuity and momentum equation, assuming a homogenous density field (Figures 4.16 and 4.17 respectively). Both approaches yield one separated eigenvalue for each azimuthal wave number. The general arrangement of the five eigenvalues for both methods is in agreement with the empirical mode decomposition from Chapter 3.2, yielding a dominant eigenvalue at  $m = -2$  and a gradually decreasing growth rate for the eigenvalues of higher and lower wave number. While the cold flow RANS eigenvalues in Figure 4.14 had a similar arrangement to their LES counterparts in terms of growth rate and relative position to each other, the reactive RANS eigenvalues are distributed different to their LES counterparts (red markers in each spectrum).

The  $m = \{-2, -3, -4, -5\}$  eigenvalues in the 'cold hot' spectrum in Figure 4.17 are located at frequencies close to the respective DFT mode frequency marked by the red lines. The  $m = -1$  eigenvalue frequency is overpredicted significantly. The eigenvalues of the low mach approach in Figure 4.16 are shifted to larger frequencies and do not agree with the DFT mode frequencies. In the low mach calculation, the eigenvalues for  $m = -2$  and  $m = -3$  have a positive growth rate while the remaining three eigenvalues are negative, in close proximity to  $\omega_i^* = 0$ . In the 'cold hot' calculation, all eigenvalues are located at a negative growth rate. Both eigenvalue spectra show a dominant eigenvalue for  $m = -2$  and a gradually decreasing growth rate for higher and lower azimuthal wave numbers. Hence, the arrangement of eigenvalues relative to each other is in fact closer to the empirical mode distribution from Figure 3.5 than the eigenvalues obtained for the LES mean field. The LSA performed on the RANS fields therefore yields results in better agreement with the DFT modes. Since the DFT modes were obtained for the LES mean field this is a questionable result.

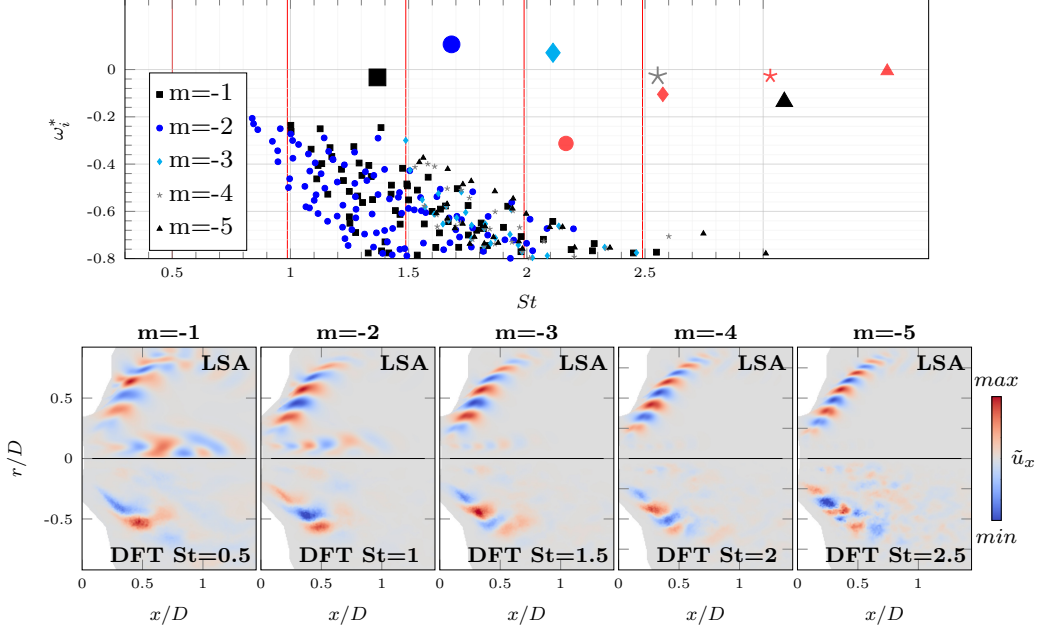


**Figure 4.16:** Low mach eigenvalue spectra and spacial shapes of separated eigenvalue at different azimuthal wavenumbers  $m = \{-1, -2, -3, -4\}$  as obtained for the reacting RANS calculated with the equations for non-uniform density. The layout is similar to Figure 4.6. The four separated eigenvalues from the low mach LSA on the reacting LES are depicted in red.

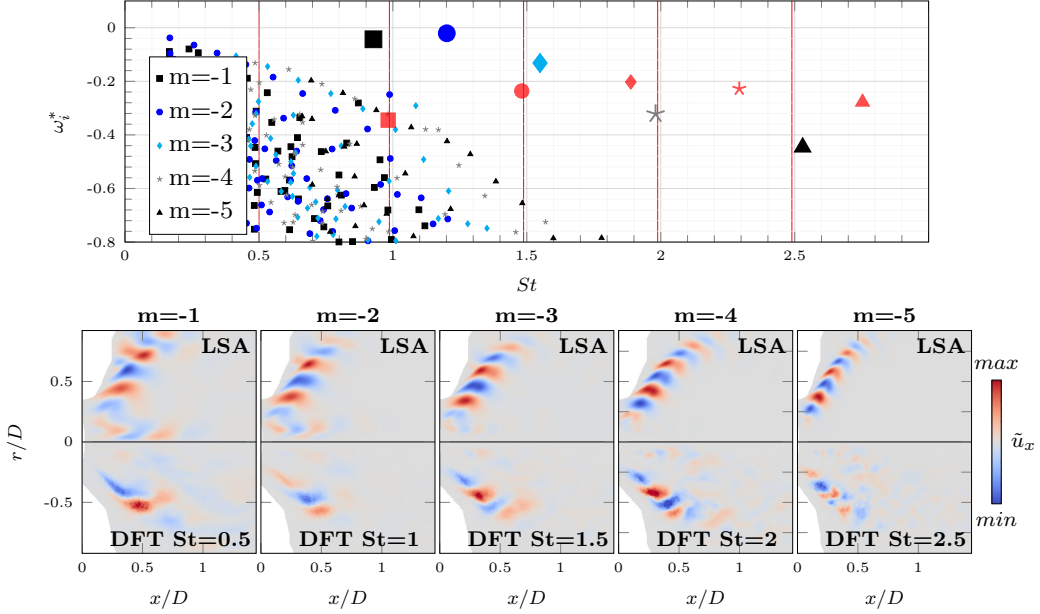


**Figure 4.17:** 'Cold hot' eigenvalue spectra and spacial shapes of separated eigenvalue at different azimuthal wavenumbers  $m = \{-1, -2, -3, -4\}$  as obtained for the reacting RANS calculated with the assumption of a uniform density. The layout is similar to Figure 4.6. The five separated eigenvalues from the 'cold hot' LSA on the reacting LES are depicted in red.

The mode shapes corresponding to each separated eigenvalue are shown in the lower part of Figure 4.16 and 4.17. For azimuthal wave numbers of  $m = -2$  and higher, the modes agree with the DFT modes in the sense that the outer shear layer is the region of highest amplitude. Also the LSA modes of low mach and 'cold hot' approach are similar for each azimuthal wave number but the low mach wavepackets are denser due to their higher frequency. The  $m = -1$  LSA mode shows high amplitudes in the inner shear layer which is not seen in the DFT modes.

Figure 4.18 shows the structural sensitivity of the low mach and 'cold hot' LSA modes. For azimuthal wave numbers of  $m = \{-2, -3, -4, -5\}$  the region of highest structural sensitivity is similar in both results. It is located in the outer shear layer between the middle passage and the recirculation zone.

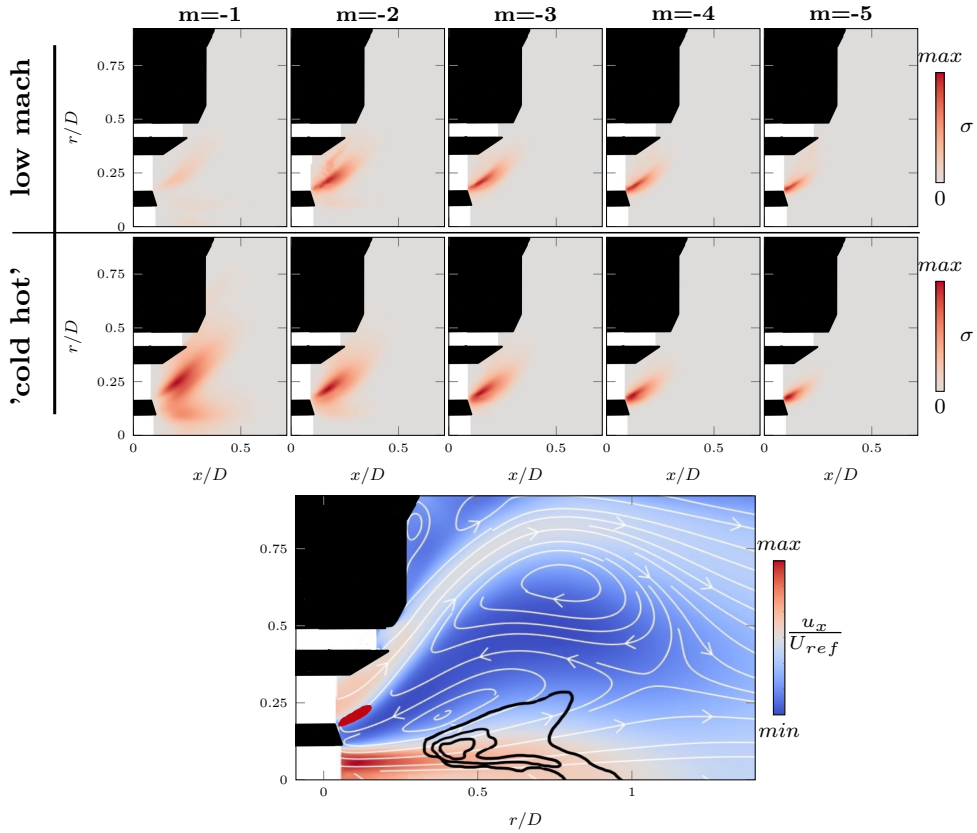


**Figure 4.18:** **a:** Structural sensitivity of the five global modes of the reacting RANS as obtained with the low mach and the 'cold hot' LSA. **b:** Axial component of mean velocity field with streamlines in x-r-plane and a clearly shaped recirculation bubble. The red mark indicates the wavemaker position.

This agrees well with the reacting LES results in Figures 4.11 and 4.13. In the low mach

calculation, the structural sensitivity of the  $m = -1$  mode appears faint. A closer look at its adjoint modes not shown here reveals a noisy and undefined field with high amplitudes at the boundary. This again leads to the assumption that the  $m = -1$  low mach mode does not stem from the same shear layer mechanism like the other modes. The 'cold hot'  $m = -1$  mode shows a defined region of high sensitivity in the outer shear layer. Also the inner shear layer appears to be included in the mode dynamics, indicating a different mechanism being active. Similar results were obtained for the 'cold hot' LSA on the reacting LES in Figure 4.13

### Conclusion

A BiGlobal LSA is performed on a cold flow LES, a cold flow RANS, a reacting LES and a reacting RANS flow field. For every configuration the LSA is conducted for azimuthal wave numbers of  $m = \{-1, -2, -3, -4, -5\}$ .

The investigation performed in this Chapter shows a good applicability of the LSA when performed on a cold LES mean field. Here, the LSA yields accurate results that are in agreement with the DFT modes extracted in Chapter 3.2. Not just the frequencies of global modes inherent to the flow are matched closely, also the growth rates are consistent with the energy fraction contained in each DFT mode. This result indicates that each mode found within the DFT is a separate mechanism with a certain azimuthal wave number, rotating on the mean field. The frequency is then dependent on the swirl and the azimuthal wave number, resulting in the frequency pattern observed in both DFT and LSA spectrum. When conducted on a cold RANS simulation, the LSA results are qualitatively comparable to the LSA results of a LES mean field: The frequency of global modes is a function of azimuthal wave number and the global mode closest to a zero growth rate is an  $m = -2$  helical instability. However, the predicted frequency and growth rate both increases for the RANS flow field as shown in Figure 4.14. This is mainly due to the differences of RANS and LES flow fields. Nonetheless, this finding underlines the applicability of linear stability analysis on a RANS flow field to extract the unsteady features of the flow.

In the reacting framework, the LSA is not able to yield accurate results. Especially when the non-uniform density is accounted for with an additional equation, the eigenvalue frequencies and growth rates are mispredicted significantly. Especially in the LES analysis, the relative arrangement of the eigenvalues is not consistent with the DFT modes. When conducted on a RANS field, the relative arrangement is closer to the DFT modes and the  $m = -2$  eigenvalue appears as the dominant mechanism. Since the DFT modes are based on the LES mean field, this result should be treated with caution and can not lead to the assumption that a RANS simulation is sufficient to extract the flow dynamics by means of LSA.

The main instability mechanism is identified in the shear layers in the upstream section of the recirculation zone. This shear layer induces helical instabilities that counter-wind relative to the mean field but rotate with the same direction. The modes of azimuthal

wave number  $m = \{-2, -3, -4, -5\}$  originate in the same shear layer between the middle inlet passage and the recirculation zone. The origin of the  $m = -1$  eigenvalue which is associated to the DFT mode at  $St = 0.5$  can not be identified with the same accuracy. The structural sensitivity analysis located its origin in the inner shear layer (cold flow LES) or in both shear layers without a defined location ('cold hot' LES, cold RANS, 'cold hot' RANS). For the low mach LSA, the eigenvalue was either not found (reactive LES) or appeared with high sensitivity on the boundaries suggesting a spurious nature (reactive RANS).

# CHAPTER 5

---

## SPOD and Resolvent Analysis

---

In the following, an investigation of a similar flow field is conducted to further evaluate the applicability of the linearized methods implemented in FELiCS. In addition to a LSA, this chapter deals with the application of resolvent analysis (RA). As a reminder, resolvent analysis is a method to investigate the hydrodynamic response of a flow field when it is acoustically forced (see Chapter 2.2.2). In contrast to LSA, RA seeks to determine feedback mechanism that are not related to intrinsic instabilities but rather to external harmonic forcing. Following [38], the RA gain spectrum can be validated on the SPOD gain spectrum.

For the SPOD, 3825 instantanious streamwise planes were extracted from the LES every 50 timesteps, resulting in a sampling timestep of  $\Delta t = 0.05$  ms and a time period of  $T = 0.19125$  s. The snapshots are segmented into blocks of 300 snapshots with an overlap of 0.8, resulting in a resolved SPOD frequency step of 66,67 Hz and a Nyquist frequency of  $f_{\text{Nyq}} = 10000$  Hz.

For every timestep, streamwise half-planes at  $N_p = 8$  different equidistant azimuthal angles  $\Theta$  were obtained. Applying an azimuthal Fourier decomposition for each timestep reading

$$\mathbf{q}^m = \frac{1}{8} \sum_{k=1}^8 \mathbf{q} e^{imk\frac{\pi}{4}\Theta}, \quad (5.1)$$

allows for a separate analysis for a certain azimuthal wave number  $m$  if  $|m| < \frac{1}{2}N_p = 4$ . Hence, instabilities of azimuthal wave numbers up to  $|m| = 3$  can be distinguished from each other. For an azimuthal wave number of  $|m| = 4$  it is not possible to distinguish the sign of the instability but nonetheless an investigation is done.

This chapter is structured as follows: First, the flow field is presented and investigated for vortex structures by means of the q-criterion. Secondly, the SPOD results for each azimuthal wave number  $-3 \geq m \leq 3$  and  $|m| = 4$  are presented and compared to LSA results conducted for the same azimuthal wave numbers. For each azimuthal wave number, the SPOD mode associated to the dominant peak is compared to the corresponding LSA mode. If no corresponding LSA mode is found, the SPOD mode is shown without a

comparison. Subsequently, the SPOD results are compared to the RA results. Each SPOD gain spectrum is overlayed with the corresponding RA gain spectrum. The general envelopes of SPOD and RA gains are compared to each other. The SPOD modes at distinct SPOD peaks are compared to the RA responses at the same frequency.

## 5.1 Flow field

A slice through the flow field under investigation is depicted in Figure 5.1. The data was obtained by means of an incompressible LES on an unstructured grid with a finite-volume scheme. The inlet geometry is identical to the flow fields investigated in Chapter 3 and 4 (see Figure 3.1). However, while those simulation where conducted on a mesh consisting of 17 million cells, the new data was calculated on a coarser mesh of 4 million cells. Since this mesh is coarser in all regions, it is not able to resolve the turbulent fluctuations down to the same scale as the high resolution LES is able to. Therefore, a larger amount of turbulent motion requires modelling, which can result in inaccuracies.

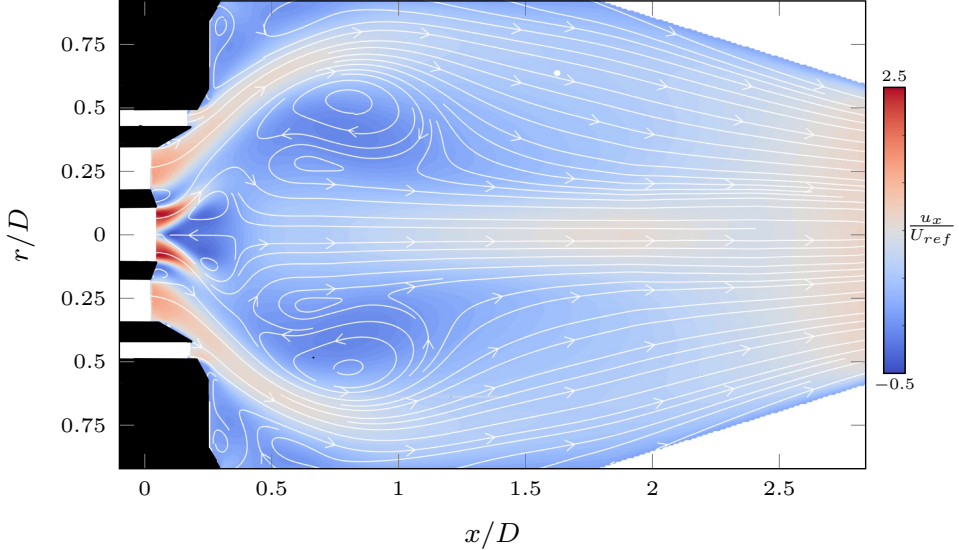


**Figure 5.1:** x-r-slice through cylindrical flow domain for cold LES. Flow direction is left to right, with the pilot jet and the outer inlet passages on the leftmost side of the figure.

In fact, the coarser grid leads to a new flow configuration, where the penetration of the pilot jet is significantly reduced. This jet splits up on the symmetry axis as visible in Figure 5.1. This flow configuration has been observed within preceding investigations [14] and is due to insufficient grid resolution downstream of the axis jet. The split up jet results in a small recirculation zone located at a central position downstream of the axis jet. Furthermore, while the precedingly investigated flow fields had two relevant shear layers, one on each side of the large recirculation zone (See Figure 3.1), now a third shear

layer between the pilot jet and the new central recirculation zone emerges. The resulting complexity of the flow field underlines the need for an azimuthal Fourier decomposition to distinguish between instabilities of different azimuthal wave number.

### Q-criterion

Before the flow field is thoroughly analyzed by means of SPOD, LSA and RA, an instantaneous three dimensional snapshot is investigated for vortex structures. As shown in Chapter 3.2, a dominant large-scale coherent structure can manifest as a helical vortex which can be extracted by means of the q-criterion. Figure 5.2 shows the isocontour of highest vorticity colored by wall distance. The view is in axial direction from a downstream position.

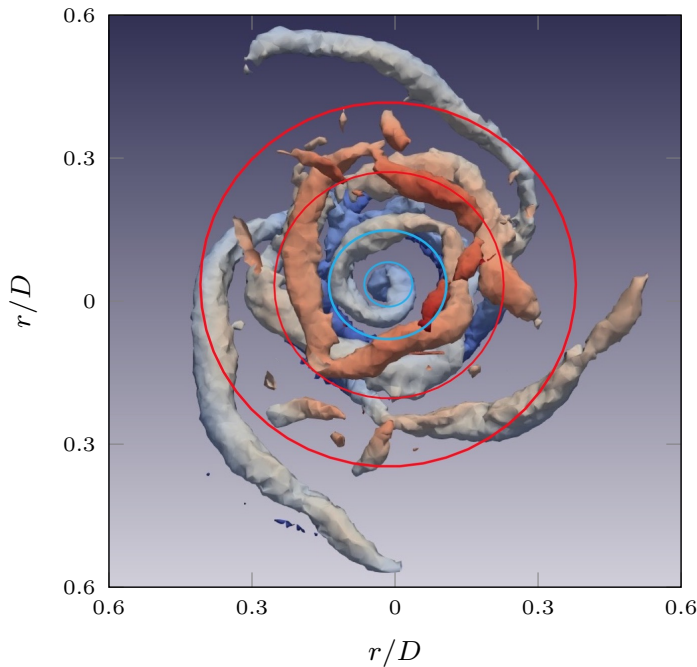


**Figure 5.2:** Isocontour of instantaneous vorticity calculated by means of the Q-criterion on the cold 3D-field. The view is in axial direction from a downstream position. The isocontour is colored by wall distance to distinguish between the inner  $|m| = 1$  and the outer  $|m| = 3$  vortex. The cyan and red circles indicate the position of the inner and middle passage respectively.

Two structures become evident in the three dimensional field: A distinct three-armed helical structure ( $|m| = 3$ ) in the region of the middle inlet passage (red circles) and a less obvious one-armed ( $m = 1$ ) helical structure in the region of the innermost passage (cyan circles). The  $|m| = 3$  vortex is counter winding relative to the  $|m| = 1$  vortex.

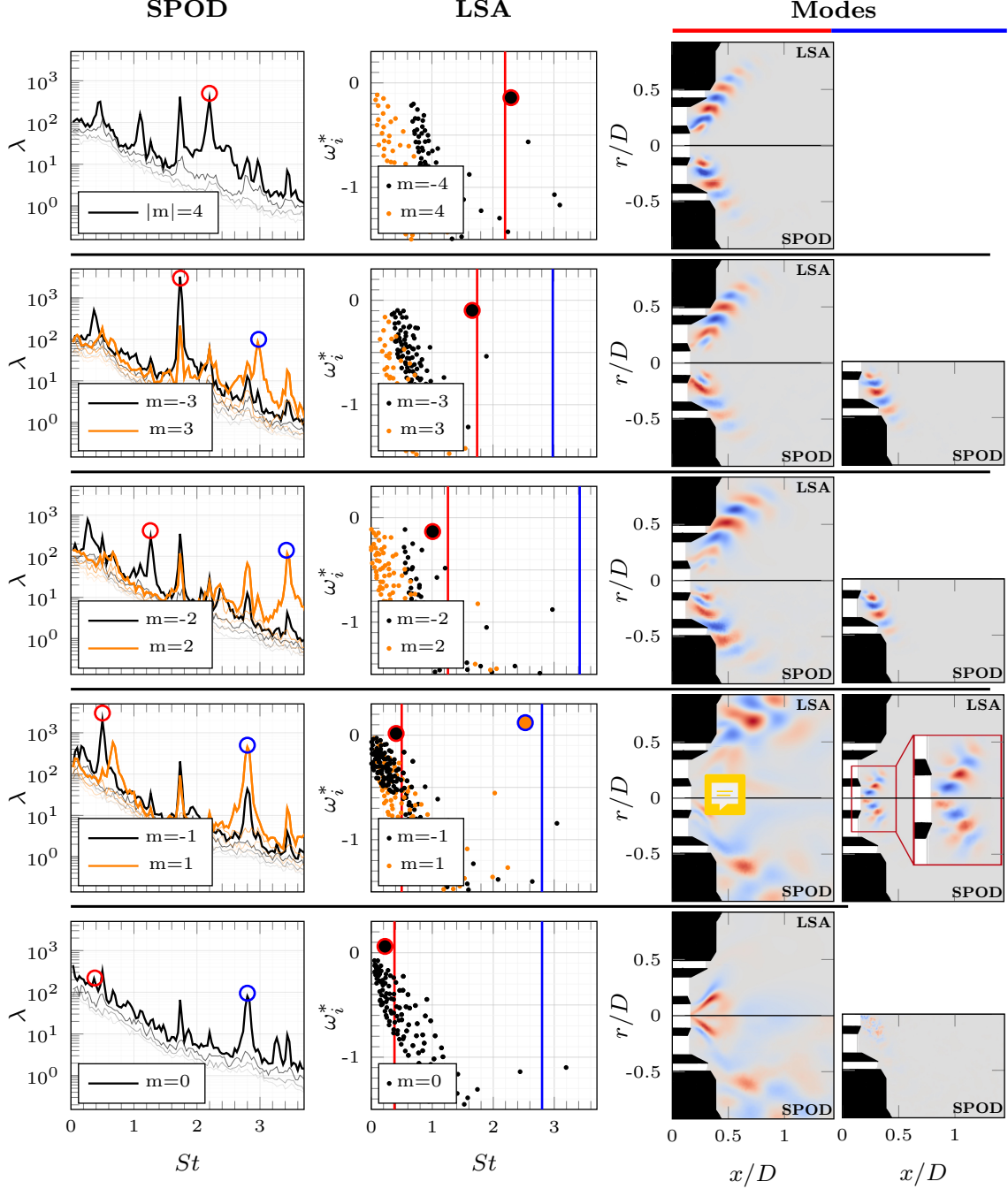
### 5.1.1 Results: SPOD and LSA

Figure 5.3 shows the combined results for SPOD and LSA. Each of the five rows presents the results for one of the five azimuthal wave numbers  $|m| = \{4,3,2,1,0\}$  in that order. In the three middle rows, the results for  $|m| = \{3,2,1\}$  for both positive and negative wave number are depicted in the same figure to make a condensed overview possible. The visualization as a whole is important because the azimuthal Fourier decomposition on only 8 different angles can not entirely filter the instabilities, which results in a complex spectrum with some peaks present in all spectra. As an example, residual spectral energy of the  $m = -3$  peak appears in all other spectra. With all results depicted together, it is easier to classify the most dominant mode for each wave number.

With this in mind, for each azimuthal wave number  $|m| > 0$  one dominant peak can be identified. These peaks are encircled in red and blue in the respective SPOD figure in the first column. For the  $|m| = 4$  peak encircled in red, a corresponding LSA eigenvalue for  $m = -4$  is found with a growth rate close to zero. The frequency is matched accurately and the SPOD and LSA mode shapes depicted in the third column are similar. A look at the second row reveals that the SPOD peak for  $m = -3$  also has a corresponding LSA eigenvalue with a close frequency match. The  $m = -3$  SPOD peak is the largest, relating this mode to the three-armed helical structure which was found in the preceding section. The SPOD and LSA mode shapes are similar as well. For the  $m = 3$  SPOD peak, no corresponding LSA eigenvalue is found. The SPOD mode has a similar structure as the  $m = -3$  but with a denser wavepacket.

For  $m = -2$ , the SPOD peak at  $St = 1.23$  is not as dominant and the  $m = -3$  peak at  $St = 1.72$  also appears in the spectrum. However, as mentioned earlier, this is due to the azimuthal Fourier decomposition. A corresponding  $m = -2$  LSA mode is found at  $St = 1$ . The SPOD and LSA mode shapes are in agreement as shown in the third column. The  $m = 2$  SPOD mode has no corresponding LSA peak however its mode shape is similar to the  $m = -3$  and  $m = -4$  modes. The fact that its frequency is twice the  $m = -3$  frequency indicates a non-linear relation between those two modes with the  $m = 2$  as a possible higher harmonic.

The  $m = -1$  SPOD shows a dominant peak at  $St = 0.5$  which has a corresponding LSA eigenvalue close to that frequency. The mode shape is not matched with the same accuracy as the preceding modes but it still resembles the instability well. For  $m = 1$ , the SPOD shows a peak at  $St = 2.72$ , which has a corresponding LSA eigenvalue at a positive growth rate in proximity to zero. The mode shape is matched accurate. This  $m = 1$  mode has been identified by means of the q-criterion in the preceding section. It is located closer to the symmetry axis than the preceding modes, indicating a location in the innermost shear layer which arises in this configuraton due to the split up inlet jet. While the modes at  $m = \{-2, -3, -4\}$  are located in the shear layer between the middle passage and the recirculation zone and hence can be related to the dominant modes found



**Figure 5.3:** SPOD and LSA spectra (first and second column) for the cold flow LES for azimuthal wave numbers  $-4 \geq m \leq 4$ . For  $|m| = \{1, 2, 3\}$ , the results for negative and positive azimuthal wave numbers are plotted in the same row. The dominant peak in every SPOD spectrum is circled either in red or blue. The frequency of those peaks is shown as equally colored lines in the LSA spectrum to allow a direct comparison. If a corresponding LSA mode is found, it is circled in the same color as the SPOD peak. Both modes are compared in the third column, red on the left and blue on the right. If no corresponding LSA mode is found, the SPOD mode is plotted alone.

in Chapter 4, the  $m = 1$  mode is located between the pilot jet and the new central recirculation zone. This explains why it is not present in the flow field of the preceding chapter, since the shear layer is not present in that case. The fact that the pilot jet has a counter rotating swirl compared to the middle inlet passage explains why this mode has a positive sign. While the SPOD identifies instabilities with a positive  $m$  for  $m = \{1,2,3\}$ , this  $m = 1$  mode is the only positive rotating mode found in the linear framework. This indicates a non-linear mechanism being active for the  $m = 2$  and the  $m = 3$  mode. The  $m = 0$  SPOD spectrum shows one large peak at  $St = 2.72$ . This peak can however be related to the  $m = 1$  peak since it has the same frequency and the mode shape shows a noisy, indistinct structure at the same region the  $m = 1$  mode is located. The peak at  $St = 1.72$  can be related to the  $m = -3$  peak. Hence, the  $m = 0$  spectrum has no dominant peak, which is a reasonable finding for a strongly swirling jet, where the most energetic coherent structures are usually of helical structure. The LSA spectrum shows one eigenvalue with a positive growth rate at  $St = 0.21$ . The  $m = 0$  SPOD spectrum shows a region of relatively large gain separation at a similar frequency and the corresponding mode shape is also similar, suggesting a weak intrinsic mechanism at that frequency. The mode shape is similar to the  $m = -1$  mode, which indicates an interaction between the two modes. It is possible, that the  $m = -1$  mode amplifies the  $m = 0$  mode.

### Structural sensitivity

To investigate the feedback mechanisms inherent to the modes, the structural sensitivity for the most distinct modes ( $m = \{-1, -2, -3, -4, 1\}$ ) is shown in Figure 5.4. It becomes evident, that the modes for  $m = \{-2, -3, -4\}$  all arise in the shear layer between pilot jet and middle passage, which is comparable to the dominant modes of the cold LES from Chapter 4 (see Figure 4.8). The wavemaker for these modes is marked as a red dot in the mean field in figure 5.4. It is located close to the splitter plate which separates the pilot and the middle passage. A flow control would be most effective at this location.

The  $m = 1$  mode shows a small region of high structural sensitivity on the symmetry axis, in the upstream section of the central recirculation zone (black dot in Figure 5.4). This underlines the fact that this mode is not found in the preceding investigation and only emerges with a split up inlet jet. A flow control by design is difficult to implement, since the wavemaker is in no close wall proximity. As shown by Kaiser [27], a dampening of such an  $|m| = 1$  mode, which emerges in a central recirculation zone, can be achieved by mounting a cylinder on the jet axis in the interior of the pilot injector. This cylinder was found to have a stabilizing effect on the coherent structure.

The  $m = -1$  mode has its highest structural sensitivity on the symmetry axis, but farther downstream when compared to the  $m = 1$  mode. This could be an indicator for a precessing vortex core (PVC) which emerges in this configuration due to the opening of a central recirculation zone. Similar to the  $m = 1$  mode, this mode could possibly be damped with a central cylinder on the jet axis.

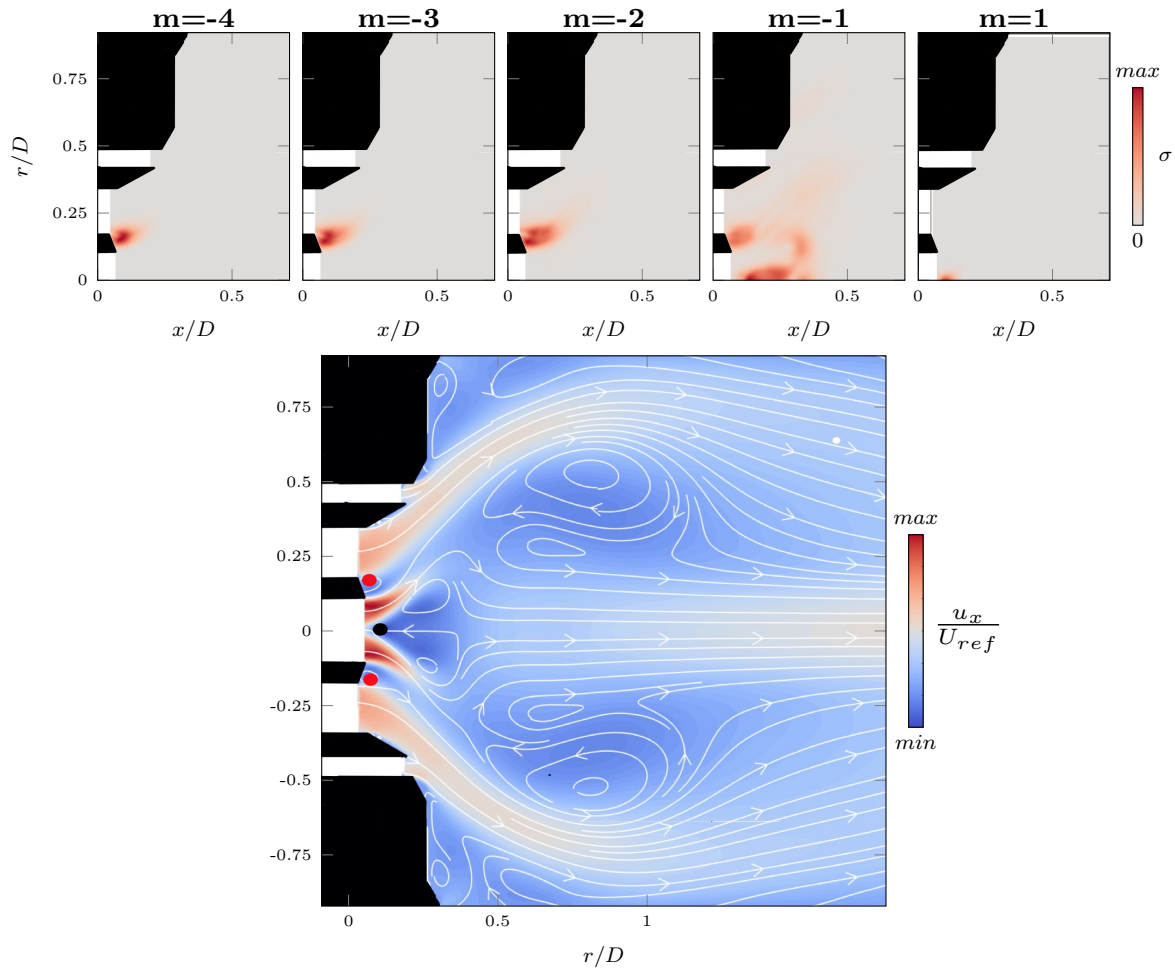


**Figure 5.4:** Structural sensitivity of the dominant LSA modes. The region of highest sensitivity is marked in the mean field in the lower half. The region of highest sensitivity are marked as a red marker for  $m = \{-2, -3, -4\}$  and as a black marker for  $m = 1$ .

### 5.1.2 Results: SPOD and RA

Figure 5.5 shows the same SPOD spectra from Figure 5.3 in comparison with the gain envelope which was obtained by means of a resolvent analysis on the mean field from Figure 5.1. The RA was performed with the boundary conditions pictured in Figure 4.1. The dominant SPOD peaks are circled for each wave number and the RA gain at that frequency is marked. The corresponding mode/response shapes are shown in the third column. The spectra are compared with respect to peaks and to the low-rank condition. As a reminder, this condition states that if there is a large separation between the first and the following eigenvalues, the spacial structure associated to the leading eigenvalue at this frequency is assumed to be representative of the instability at that frequency. Hence, when validating the RA gains with the SPOD spectra, a large gain separation at the same frequency indicates an accurate RA result.

The RA gains all decrease in energy for higher frequencies, which is in general agreement with the SPOD spectra. While the SPOD shows distinct peaks for each azimuthal wave number, the gain spectra do not reproduce those peaks in all cases. For the positive azimuthal wave numbers of  $m = \{4, 3, 2\}$ , the RA gain shows no peak at any positions. These three wave numbers had no global mode in the LSA analysis. Since both LSA and RA do not predict the SPOD modes for these azimuthal wave numbers, the underlying mechanisms are likely to be of non-linear nature and arise due to amplification from other, linear modes. A look at the  $m = 1$  spectrum reveals a RA gain envelope in agreement with the SPOD spectrum. The SPOD peak at  $St = 2.72$  is predicted and shows a large gain separation. The corresponding RA response shows an exact agreement with the SPOD mode. The large gain therefore can be explained with the presence of a globally unstable mode which was found in the preceding section (see Figure 5.3). For  $m = -1$  and  $m = 0$ , the gain envelope has no distinct peak. In both cases the RA response matches the SPOD mode at the marked positions which is chosen based on the global LSA modes from Figure 5.3.

An accurate prediction of the SPOD spectrum is obtained for the azimuthal wave numbers of  $m = \{-4, -3, -2\}$ . The RA gain envelopes match the respective SPOD spectrum in the sense that both low frequency and high frequency SPOD peaks are identified and show low-rank behaviour. The high-frequency peaks all agree with the frequency of the global mode found within the LSA, which is marked with a vertical line. The high frequency response shapes are in close agreement to the SPOD mode shapes as depicted in the rightmost figures. These RA gains therefore arise due to the presence of a global mode, which is also observed for the  $m = 1$  mode. The low frequency SPOD peaks are matched precisely by the RA gains in all three cases and the corresponding mode shapes also agree with the SPOD modes. The shapes are different than the high frequency modes, with a high amplification further downstream and a larger wavelength due to the lower frequency. These RA responses have no LSA equivalent, which suggests a non-modal growth in the shear layer between the middle inlet jet and the downstream section of the large recirculation zones.

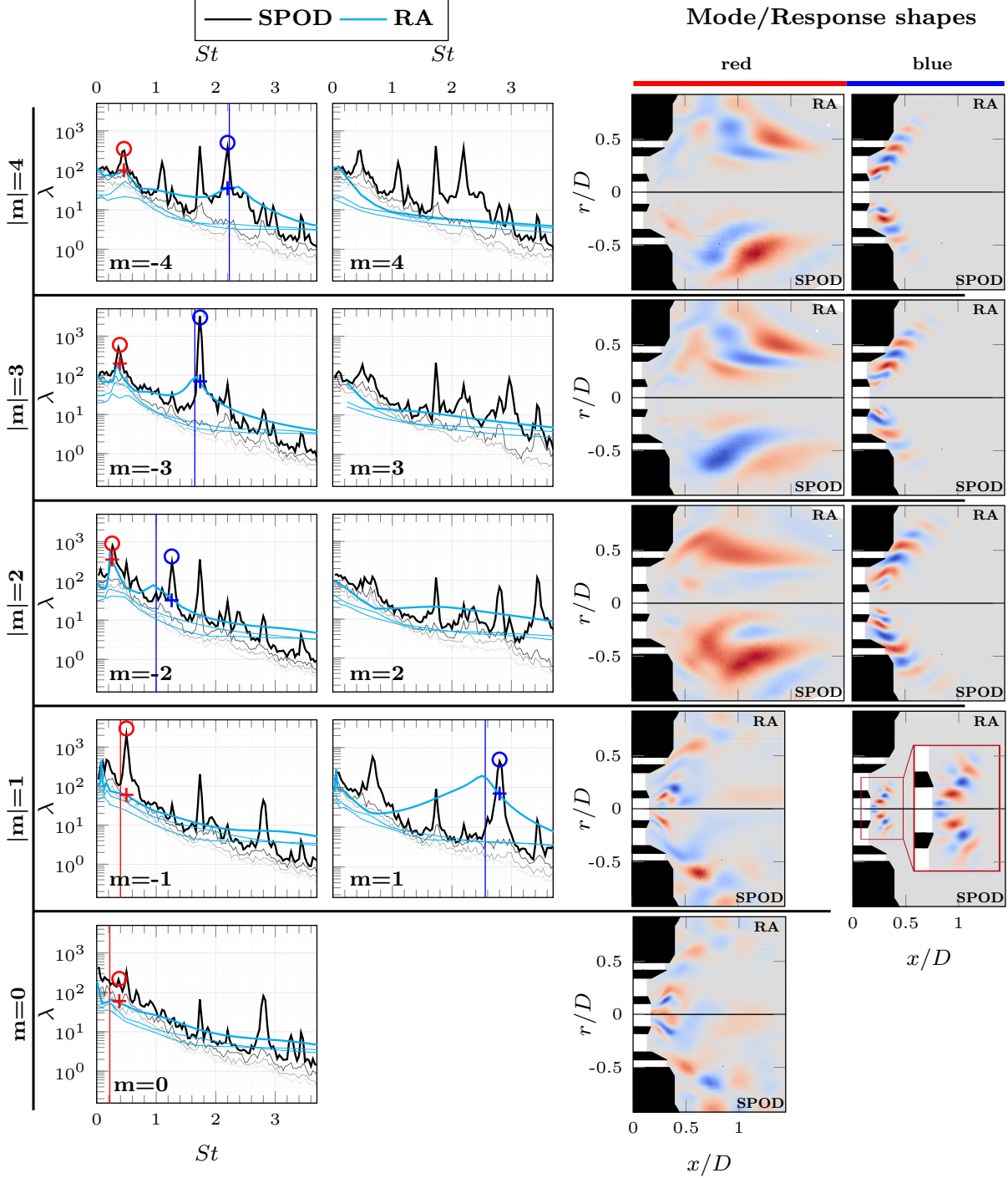


**Figure 5.5:** SPOD spectra and RA gains for the cold flow LES for azimuthal wave numbers of  $-4 \geq m \leq 4$ . The SPOD and RA spectra for each azimuthal wave number are plotted in the same figure to directly compare the envelopes. The dominant SPOD peak is circled in either red or blue and the corresponding RA gain at that frequency is marked with a cross in the same color. If a global mode was found within the LSA, a vertical line indicates the frequency of that mode in the same color as the corresponding SPOD peak. The associated SPOD and RA modes are pictured in direct comparison in the third column of the figure, with red marked modes/responses on the left and blue marked modes/responses on the right.



---

## Appendix

---

### LSA spectrum with and without sponge viscosity

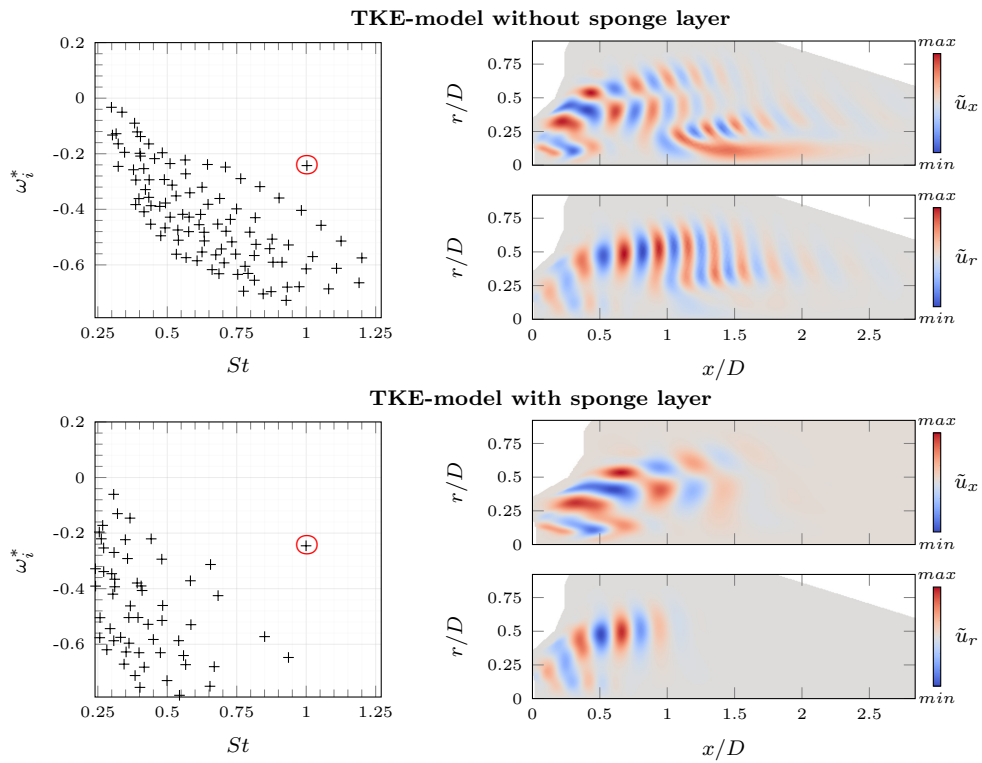


**Figure 5.6:** Eigenvalue spectrum of LSA conducted with the TKE-viscosity model. The upper half shows the results for a deactivated sponge layer, the lower half for an activated sponge layer. The separated eigenvalue is not affected by the sponge viscosity.



---

## Bibliography

---

- [1] John William Strutt Baron Rayleigh. *The theory of sound*, volume 2. Macmillan, 1896.
- [2] Thierry Poinsot. Prediction and control of combustion instabilities in real engines. *Proceedings of the Combustion Institute*, 36(1):1–28, 2017.
- [3] Roger E Bilstein. *Stages to Saturn: A technological history of the Apollo/Saturn launch vehicles*, volume 4206. US Government Printing Office, 1996.
- [4] Dwight Barkley. Linear analysis of the cylinder wake mean flow. *EPL (Europhysics Letters)*, 75(5):750, 2006.
- [5] Abul Khair Muhammad Fazle Hussain and William C Reynolds. The mechanics of an organized wave in turbulent shear flow. *Journal of Fluid Mechanics*, 41(2):241–258, 1970.
- [6] Garry L Brown and Anatol Roshko. On density effects and large structure in turbulent mixing layers. *Journal of Fluid Mechanics*, 64(4):775–816, 1974.
- [7] S Cj Crow and FH Champagne. Orderly structure in jet turbulence. *Journal of fluid mechanics*, 48(3):547–591, 1971.
- [8] Kilian Oberleithner. *On turbulent swirling jets: Vortex breakdown, coherent structures, and their control*. PhD thesis, Universitaetsbibliothek der Technischen Universität Berlin, 2012.
- [9] Outi Tammisola and Matthew Juniper. Coherent structures in a swirl injector at  $re=4800$  by nonlinear simulations and linear global modes. 2016.
- [10] Kilian Oberleithner, Moritz Sieber, CN Nayeri, Christian Oliver Paschereit, Christoph Petz, Hans-Christian Hege, Bernd R Noack, and I Wygnanski. Three-dimensional coherent structures in a swirling jet undergoing vortex breakdown: stability analysis and empirical mode construction. *Journal of fluid mechanics*, 679:383, 2011.
- [11] S Terhaar, B Ćosić, CO Paschereit, and K Oberleithner. Suppression and excitation of the precessing vortex core by acoustic velocity fluctuations: An experimental and analytical study. *Combustion and Flame*, 172:234–251, 2016.

- [12] Finn Lückoff, Thomas Ludwig Kaiser, Christian Oliver Paschereit, and Kilian Oberleithner. Mean field coupling mechanisms explaining the impact of the precessing vortex core on the flame transfer function. *Combustion and Flame*, 223:254–266, 2021.
- [13] Jonas P Moeck, Jean-François Bourgouin, Daniel Durox, Thierry Schuller, and Sébastien Candel. Nonlinear interaction between a precessing vortex core and acoustic oscillations in a turbulent swirling flame. *Combustion and Flame*, 159(8):2650–2668, 2012.
- [14] Nick Treleaven. *The numerical prediction of the acoustic response of liquid-fuelled, swirl-stabilised flames*. PhD thesis, Loughborough University, 2019.
- [15] Thomas Ludwig Kaiser, Lutz Lesshafft, and Kilian Oberleithner. Prediction of the flow response of a turbulent flame to acoustic perturbations based on mean flow resolvent analysis. *Journal of Engineering for Gas Turbines and Power*, 141(11), 2019.
- [16] Patrick Huerre and Peter A Monkewitz. Absolute and convective instabilities in free shear layers. *Journal of Fluid Mechanics*, 159:151–168, 1985.
- [17] W Koch. Local instability characteristics and frequency determination of self-excited wake flows. *Journal of Sound and Vibration*, 99(1):53–83, 1985.
- [18] Matthew P Juniper. Absolute and convective instability in gas turbine fuel injectors. 44687:189–198, 2012.
- [19] Thierry Poinsot and Denis Veynante. *Theoretical and Numerical Combustion*, volume 3. R.T. Edwards Inc., 2001.
- [20] MS Anand, R Eggels, M Staufer, M Zedda, and J Zhu. An advanced unstructured-grid finite-volume design system for gas turbine combustion analysis. In *ASME 2013 Gas Turbine India Conference*. American Society of Mechanical Engineers Digital Collection, 2013.
- [21] Suhas Patankar. *Numerical heat transfer and fluid flow*. Taylor & Francis, 2018.
- [22] Clay Mathematics Institute. Millennium Problems. <https://www.claymath.org/sites/default/files/navierstokes.pdf>, 2000. [Online; accessed 21-March-2021].
- [23] Hermann Sohr. *The Navier-Stokes equations: An elementary functional analytic approach*. Springer Science & Business Media, 2012.
- [24] Robert R Schaller. Moore’s law: past, present and future. *IEEE spectrum*, 34(6):52–59, 1997.
- [25] Osborne Reynolds. Iv. on the dynamical theory of incompressible viscous fluids and the determination of the criterion. *Philosophical transactions of the royal society of london.(a.)*, (186):123–164, 1895.

- [26] Stephen B Pope. Turbulent flows, 2001.
- [27] Thomas L. Kaiser. *Impact of Flow Rotation on Flame Dynamics and Hydrodynamic Stability*. PhD thesis, L'UNIVERSITE DE TOULOUSE, 2019.
- [28] WC Reynolds and AKMF Hussain. The mechanics of an organized wave in turbulent shear flow. part 3. theoretical models and comparisons with experiments. *Journal of Fluid Mechanics*, 54(2):263–288, 1972.
- [29] Kilian Oberleithner, Lothar Rukes, and Julio Soria. Mean flow stability analysis of oscillating jet experiments. *Journal of fluid mechanics*, 757:1–32, 2014.
- [30] Lothar Rukes, Christian Oliver Paschereit, and Kilian Oberleithner. An assessment of turbulence models for linear hydrodynamic stability analysis of strongly swirling jets. *European Journal of Mechanics-B/Fluids*, 59:205–218, 2016.
- [31] Arnold Martin Kuethe. *Investigations of the turbulent mixing regions formed by jets*. Guggenheim Aeronautical Laboratory, 1935.
- [32] Herbert Brien Squire and J Trouncer. Round jets in a general stream. Technical report, AERONAUTICAL RESEARCH COUNCIL LONDON (UNITED KINGDOM), 1944.
- [33] Mario Casel. Identification of coherent structures in non-reacting and reacting jet flows using spectral proper orthogonal decomposition and resolvent analysis. 2020.
- [34] Flavio Giannetti and Paolo Luchini. Structural sensitivity of the first instability of the cylinder wake. *Journal of Fluid Mechanics*, 581(1):167–197, 2007.
- [35] Samir Beneddine, Denis Sipp, Anthony Arnault, Julien Dandois, and Lutz Lesshafft. Conditions for validity of mean flow stability analysis. *Journal of Fluid Mechanics*, 798:485, 2016.
- [36] John Leask Lumley. The structure of inhomogeneous turbulent flows. *Atmospheric turbulence and radio wave propagation*, 1967.
- [37] Oliver T Schmidt and Tim Colonius. Guide to spectral proper orthogonal decomposition. *Aiaa journal*, 58(3):1023–1033, 2020.
- [38] Aaron Towne, Oliver T Schmidt, and Tim Colonius. Spectral proper orthogonal decomposition and its relationship to dynamic mode decomposition and resolvent analysis. *Journal of Fluid Mechanics*, 847:821–867, 2018.
- [39] Moritz Sieber, C Oliver Paschereit, and Kilian Oberleithner. Spectral proper orthogonal decomposition. *Journal of Fluid Mechanics*, 792:798–828, 2016.
- [40] Olgierd Cecil Zienkiewicz and Robert Leroy Taylor. *The finite element method, ; volume 1: basic formulation and linear problems*. 1994.
- [41] Lutz Lesshafft. Artificial eigenmodes in truncated flow domains. *Theoretical and Computational Fluid Dynamics*, 32(3):245–262, 2018.